2017-06-01

Development of a Performance-Based Procedure to Predict Liquefaction-Induced Free-Field Settlements for the Cone Penetration Test

Mikayla Son Hatch
Brigham Young University

Development of a Performance-Based Procedure to Predict Liquefaction-Induced Free-Field Settlements for the Cone Penetration Test

Mikayla Son Hatch

A thesis submitted to the faculty of
Brigham Young University
in partial fulfillment of the requirements for the degree of

Master of Science

Kevin W. Franke, Chair
Kyle M. Rollins
Paul W. Richards

Department of Civil and Environmental Engineering

Brigham Young University

ABSTRACT

Development of a Performance-Based Procedure to Predict
Liquefaction-Induced Settlements for the
Cone Penetration Test

Mikayla Son Hatch
Department of Civil Engineering, BYU
Master of Science

Liquefaction-induced settlements can cause a large economic toll on a region, from severe infrastructural damage, after an earthquake occurs. The ability to predict, and design for, these settlements is crucial to prevent extensive damage. However, the inherent uncertainty involved in predicting seismic events and hazards makes calculating accurate settlement estimations difficult. Currently there are several seismic hazard analysis methods, however, the performance-based earthquake engineering (PBEE) method is becoming the most promising. The PBEE framework was presented by the Pacific Earthquake Engineering Research (PEER) Center. The PEER PBEE framework is a more comprehensive seismic analysis than any past seismic hazard analysis methods because it thoroughly incorporates probability theory into all aspects of post-liquefaction settlement estimation. One settlement estimation method, used with two liquefaction triggering methods, is incorporated into the PEER framework to create a new PBEE (i.e., fully-probabilistic) post-liquefaction estimation procedure for the cone penetration test (CPT). A seismic hazard analysis tool, called *CPTLiquefY*, was created for this study to perform the probabilistic calculations mentioned above.

Liquefaction-induced settlement predictions are computed for current design methods and the created fully-probabilistic procedure for 20 CPT files at 10 cities of varying levels of seismicity. A comparison of these results indicate that conventional design methods are adequate for areas of low seismicity and low seismic events, but may significantly under-predict seismic hazard for areas and earthquake events of mid to high seismicity.

Keywords: cone penetration test (CPT), *CPTLiquefY*, liquefaction, performance-based earthquake engineering, seismic hazard, settlement

ACKNOWLEDGEMENTS

I want to thank my advisor chair, Dr. Kevin Franke, for all of his help, encouragement, and patience. He recognized potential in me that I struggled to originally see in myself. I want to thank him for the countless hours of tutoring and support he provided, without which I would not have been able to complete this intensive research. Not only did he help me find my passion for geotechnical engineering, he has inspired me to be the best person, and engineer, I can be. I would not be where, or who, I am today without his support.

I also want to thank members of my graduate committee, Dr. Kyle M. Rollins and Dr. Paul Richards. They have each had a significant influence in shaping me into the engineer I am today. I thank my fellow team members, Tyler Coutu and Alex Arndt, both of whom I would not have completed this project without. I am grateful for your support, help, and friendship.

I would like to thank my dad, Stacey Son, for not only all of the help and C++ tutoring he provided, but for years of love, support and encouragement. I don't think I would have had the confidence to try, and discover my deep passion for, engineering without your encouragement. I thank my mom, Pamela Paxman, for never letting me limit myself and teaching me how to set and achieve goals. I thank my older sister, Melyssa Fowler, for being my biggest role model, for all the phone calls of encouragement, help with C++, and for always being there for me.

Finally, and most of all, I thank my husband, Jarom Hatch. You are my biggest supporter and have never questioned my ability to fulfill my dream of becoming an engineer. I'm so grateful for all that you have done for me to help me through grad school, I love you.

TABLE OF CONTENTS

LIST OF TABLES

LIST OF FIGURES

1 INTRODUCTION

During an earthquake event, soil has the potential to liquefy and subsequently cause ground surface settlements. Liquefaction-induced settlements are not directly life-threatening, but the resulting effects can be dangerous and take a large economic toll. When settlements occur unevenly, called differential settlement, they can cause the severing of lifelines, utility lines, and severe structural and roadway damage. Structural damage caused by differential settlement can range from cracking to dangerous structural collapse. The severing of lifelines or utilities can be dangerous because it could spark a fire, spread disease when people are unable to receive clean water, and even prevent firefighters from being able to put out earthquake-caused fires by preventing access to water. In addition, the widespread damage caused by differential settlement can cause a huge economic toll on a city. Also severe damage of roadways and highways can prevent shipment of goods in or out of the city, adding to the financial distress.

To be able to prevent these scenarios, engineers need to be able to predict seismic effects, and the damage they cause, accurately. Liquefaction was not critically studied until the 1964 Niigata and Alaska earthquakes, which caused extensive liquefaction damage. Therefore liquefaction is a relatively new research area, so prediction methods are continually being improved and developed. Originally, engineers used a deterministic (or scenario-based) analysis method to predict liquefaction effects. In the past 20 years, however, engineers have relied more

on a pseudo-probabilistic approach to predict liquefaction effects. This approach uses a ground motion from a probabilistic seismic hazard analysis (PSHA) to represent the design earthquake, but computes the liquefaction and its effects using deterministic analysis procedures.

Recent research has found that a performance-based earthquake engineering (PBEE) approach produces more accurate and consistent hazard estimates than the current pseudo-probabilistic approach (Kramer & Mayfield, 2007; Franke et al. 2014). PBEE applies a fully-probabilistic analysis into the prediction of earthquake effects and presents these predictions in terms of levels of hazard. PBEE is extremely advantageous for not only predicting hazard for liquefaction triggering and its effects, but also presenting this hazard in a way for all stakeholders to make more informed decisions. Unfortunately, due to the complex nature of probability theory and the numerous calculations required, PBEE is not used widely yet in practice.

Most geotechnical PBEE analysis methods have been developed for the standard penetration test (SPT) rather than for the cone penetration test (CPT). This discrepancy is due to the relative novelty of the CPT. The CPT is a method used to determine soil properties by pushing an instrumented cone into the ground at a controlled rate. The cone reads the resistance it receives from each soil layer as it is advanced through the soil. These resistances can then be correlated to the soil's relative density or consistency, which correlates to its ability to resist liquefaction. The use of the CPT has grown rapidly due to the speed of the test and the continuous nature of its results. Deterministic and pseudo-probabilistic post-liquefaction settlement analysis methods have been developed for the CPT, but no performance-based method has been developed and tested yet. As such, there are three purposes to this study: first, to create a new performance-based procedure for the estimation of free-field post-liquefaction settlements for the CPT; second, to develop an analysis tool to perform and simplify the necessary probabilistic

calculations; and third, to assess and quantify the differences between the performance-based (i.e., fully-probabilistic) and pseudo-probabilistic post-liquefaction settlement analyses.

2 SESIMIC LOADING CHARACTERIZATION

When engineers can accurately quantify earthquake ground motion parameters, they are able to accurately design for seismic events. Earthquake engineering is still a relatively new field but is improving with improved instrumentation, an increase of instrumentation stations, and more understanding of the physics and mechanics behind earthquake ground motions.

2.1 Earthquakes

Earthquakes continue to be one of the most devastating natural disasters civilizations must face. Earthquakes and their effects can be extremely fatal and economically cripple a region. Engineers attempt to reduce the negative causes of an earthquake by preparing their designs for a certain level of earthquake. To accomplish this, it is important to have a metric to be able to quantify an earthquake.

The first step in characterizing an earthquake is to quantify the "size" on an earthquake. The size of an earthquake has historically been recorded and described in different ways. Prior to modern technology, an earthquake was quantified based on crude and qualitative descriptions (Kramer, 1996). With technological advancements, modern seismographs have been developed to record earthquake sizes in a more quantitative fashion.

Before the development of seismographs, an earthquake's size was recorded by recording the intensity. The intensity is a qualitative measure recording of observed damage and people's reactions compared to their location. After a seismic event, intensities were recorded through interviews and recorded observations. The measure of intensity is extremely subjective and consistency is questionable because two different people could perceive the intensity differently from each other.

With technological advancements and a need for a less subjective measure of earthquake size, strong motion recording instruments, such as accelerometers and seismometers, were developed and provided a quantitative measure of earthquake sizes. Instruments allow engineers to record earthquake ground motions in the form of acceleration, velocity, and displacement. These recordings became known as earthquake time histories. Time histories have led to an objective and quantitative measurement of earthquake size called earthquake magnitude.

Many magnitude scales have been developed over the years. A commonly known magnitude scale is the Richter local magnitude scale. In 1935, Charles Richter used a Wood-Anderson seismometer to define a magnitude scale for shallow, local earthquakes in southern California (Richter, 1935). The Richter scale is the most widely known magnitude scale but is only applicable to shallow and local earthquakes. For this reason, it is not usually used in design. Magnitude scales were then developed based on surface and body waves (Kanamori, 1983). Surface and body wave magnitude scales are used more widely than the Richter scale but are less reliable when distinguishing between large earthquakes. This is because large earthquakes tend to produce saturation in their recordings. Saturation occurs when ground motion recordings produce constant readings after a certain level of earthquake. As the total energy released during an earthquake increases, the ground motion parameters do not increase at the same rate, causing

saturation in the readings. The most commonly used magnitude scale is the moment magnitude scale, which is not directly measured from any ground motion and therefore is not subject to saturation (Hanks & Kanamori, 1979; Kanamori, 1977). Ground motion recordings are used to back calculate the seismic moment, which is a measure of the energy released by the earthquake. This study uses moment magnitude in all references to an earthquake's magnitude.

2.2 Ground Motion Parameters

To accurately characterize an earthquake's strong ground motions quantitatively, ground motion parameters are essential. The most commonly used ground motion parameters to characterize a seismic event are amplitude, frequency content, and duration parameters. It is impossible to accurately describe all important ground motion characteristics using a single parameter (Jennings, 1985; Joyner & Boore, 1988). Ground motion parameters are usually obtained from an acceleration, velocity, and/or displacement time histories. A typical recorded time history is shown in Figure *2-1*. Typically, an acceleration time history is recorded then used to calculate a velocity and/or displacement time history through integration and filtering.

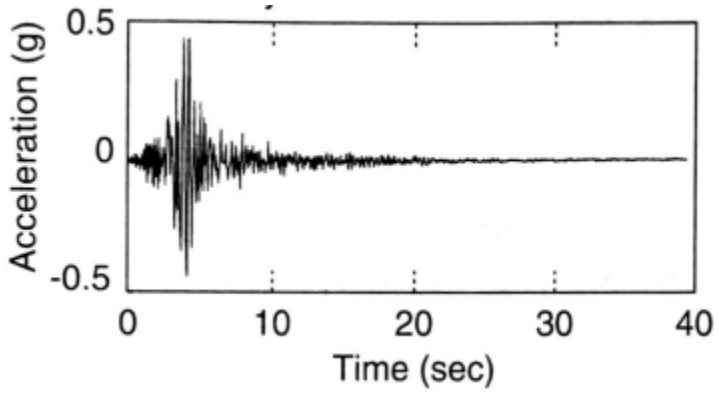

Figure 2-1: A typical recorded time history (Kramer, 1996).

2.2.1 Amplitude Parameters

Amplitude parameters are used to describe the maximum value of a specific ground motion. Amplitude can be expressed as maximum acceleration, velocity, and/or displacement. The most widely-used amplitude parameter is the peak ground acceleration (PGA) or peak ground surface acceleration (a_{max}). The PGA can be broken up into peak horizontal acceleration (PHA) and peak vertical acceleration (PVA) to distinguish between horizontal and vertical accelerations.

The PGA is a useful ground motion parameter, but it cannot be used on its own to accurately characterize a seismic event. Figure *2-2* depicts two hypothetical acceleration time histories with similar PGA values. To only characterize the earthquakes using the PGA ground motion parameter would yield inaccurate results. It is apparent time history (b) developed more energy than time history (a) because of the frequency content time history (b) developed. This example shows how important it is to not characterize an earthquake using a single ground motion parameter.

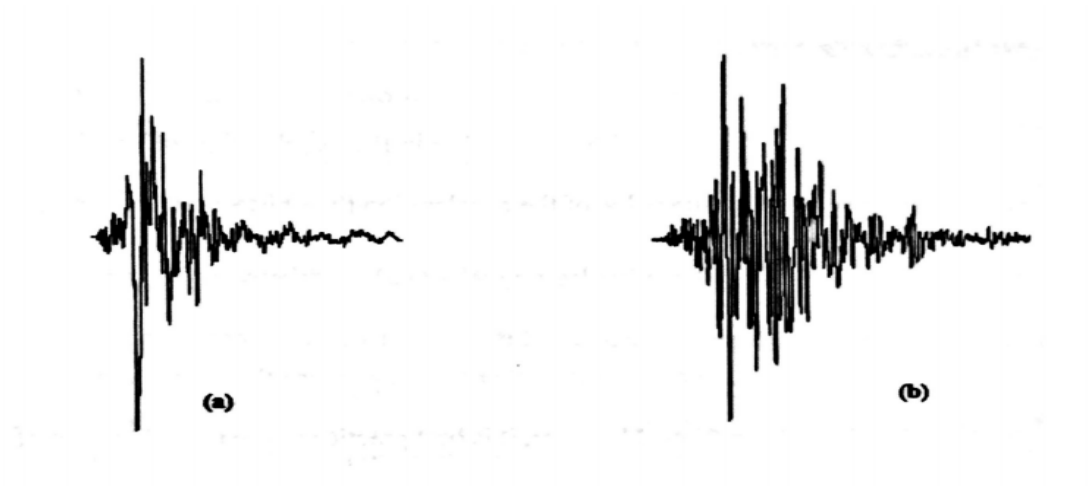

Figure 2-2: Two hypothetical time histories with similar PGA values (Kramer, 1996).

2.2.2 Frequency Content Parameters

Every structure is affected by the frequency content of an earthquake event uniquely. Frequency content describes how quickly the amplitude of a ground motion is repeated over a given duration of time. Every structure has a frequency at which it oscillates inherently, called its natural frequency. When earthquake loading corresponds to a frequency that matches a structure's natural frequency, the structure will experience resonance. Resonance causes the amplitudes of both the structure's oscillation and oscillation from the earthquake to compound. Resonance is the reason some structures hardly deform by a particular earthquake loading, but a building next door may experience a drastic increase of deformation damage because of its natural frequency.

The frequency content of a ground motion can be described as a mathematical function known as the Fourier spectrum. A Fourier spectrum is an analysis of a series of simple harmonic terms of varying frequency, amplitude and phase (Steven L Kramer, 1996). In respect to earthquake engineering, a Fourier series shows the distribution of the amplitude of a specific time history with respect to frequency.

The Fourier amplitude spectrum, a plot of Fourier amplitude versus frequency, is often used to express frequency content. When plotted for a strong ground motion, the Fourier amplitude spectrum shows how amplitude is distributed with respect to frequency. Figure *2-3* depicts two Fourier spectrums of the east-west loading from the 1989 Loma Prieta earthquake. As shown, the shapes of the Fourier spectra are quite different. The Gilroy No.1 (rock) spectrum is the strongest at low period, or high frequencies, while the Gilroy No.2 (soil) is the strongest at high periods, or low frequencies.

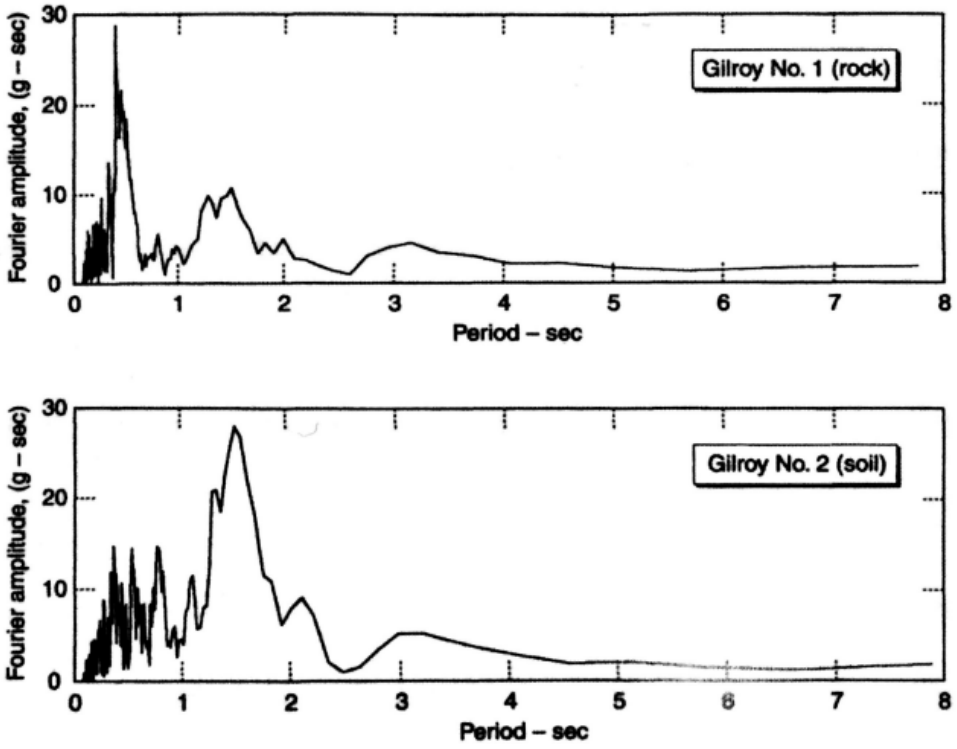

Figure 2-3: Fourier amplitude spectra for the E-W components of the Gilroy No. 1 (rock) and Gilroy No.2 (soil) strong motion records (Kramer, 1996).

Fourier spectra are very useful in predicting earthquake ground motion hazards. Engineers can use Fourier spectra to predict the hazard level of specific ground motions for a structure based on its natural frequency. If a structure has a natural frequency similar to the critical frequency described by the Fourier spectrum, it will experience resonance. An engineer could then know to design the structure to resist extreme lateral loads. Also, the engineer could design the height and mass distribution of the structure to create a natural frequency different from the critical frequency, based on the Fourier spectrum.

2.2.3 Duration Parameters

Duration of strong ground motions can also affect the amount of earthquake damage. Duration can cause degradation of stiffness and strength of structures, buildup of pore water pressures in soils, and weakening of soil layers. A short duration of a large earthquake may not occur long enough for intensive damage to occur. However, a weaker earthquake with a longer duration may occur long enough for intensive damage to occur.

Different approaches exist to quantify duration. Most commonly used is the bracketed duration (Bolt, 1969), which is the time between the first and last exceedance of a defined threshold (usually 0.05g) on an accelerogram (Figure *2-4*). An accelerogram generally records all ground motions from an initial loading till the ground motions return to a standard level.

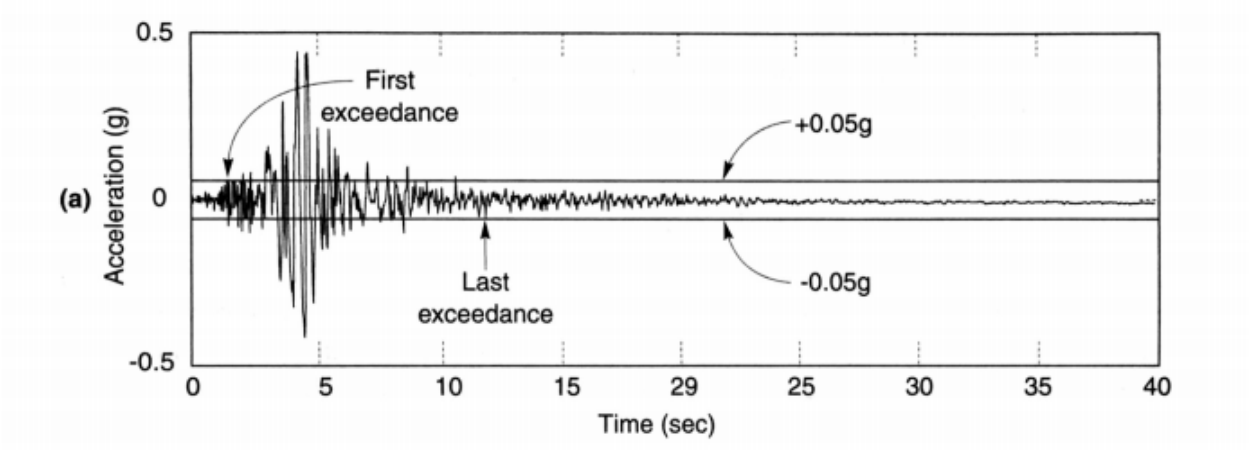

Figure 2-4: Bracketed duration measurement (Kramer, 1996).

2.2.4 Ground Motion Parameters that describe Amplitude, Frequency Content, and/or Duration

Amplitude, frequency content, and duration are all influential parameters; consequently, some parameters have been created that can describe more than one parameter at once. Each of the discussed parameters are important but are limited to describing only one aspect of an

earthquake, making these combined ground motion parameters very useful. The rms acceleration parameter was created to describe the effects of both amplitude and frequency (Kramer, 1996). Arias Intensity (I_a) also describes amplitude and frequency by integrating across the acceleration time history, resulting in the amount of energy from a strong ground motion (Arias, 1970). A few other common parameters include the cumulative absolute velocity (CAV) (Benjamin & Associates, 1988), response spectrum intensity (SI) (Housner, 1959), acceleration spectrum intensity (Von Thun, 1988), and effective peak acceleration (EPA) (Applied Technology Council, 1978).

2.3 Ground Motion Prediction Equations

Engineers are able to predict ground motions for future events by using relationships developed from previously recorded time histories, called ground motion prediction equations (GMPEs). Attenuation relationships have been developed for numerous input variables including magnitude, distance, and site specific effects that are described in detail in section 3.4.

Since peak acceleration is the most commonly used ground motion parameter, extensive effort has been exerted in the development of attenuation relationships for peak acceleration. In 1981, Cambell used previously recorded data from across the world to develop an attenuation relationship for the mean peak acceleration for sites within 50 km of the fault rupture and with earthquake magnitudes 5.0 to 7.7. Cambell and Bozorgnia (1994) used earthquake data from earthquakes of magnitudes 4.7 to 8.1 to predict peak acceleration at distances within 60 km from the fault rupture. Boore et al. (1993) expanded this relationship to predict peak accelerations within 100 km of fault rupture for earthquake magnitudes 5.0 to 7.7. Toro et al. (1995) developed

attenuation relationships for the mid-continental eastern United States. Finally, Youngs et al. (1988) developed acceleration attenuation relationships for specifically subduction zones.

With an increase in new earthquake data, a more unified and updated relationship was needed. Five research teams were given the same set of ground motion data and were asked to each develop new relationships called the Next Generation Attenuation (NGA) Relationships (Abrahamson & Silva, 2008; Boore & Atkinson, 2008; Cambell & Bozorgnia, 2008; Chiou & Youngs, 2008; Idriss, 2008). The NGA equations were updated in 2013 to the NGA West 2 relationships (Ancheta et al., 2014). These attenuation relationships were developed specifically for the western US and other areas of high seismicity. Care should be taken when using these relationships to avoid using them incorrectly or extrapolating their use to invalid seismic predictions.

2.4 Local Site Effects

Attenuation relationships depend heavily on magnitude and distance; however, local site effects can profoundly influence ground motion parameters. The extent of their effects depends on the soil properties, characteristics of earthquake loading, topography, and geometry of the site. Local site effects can be very difficult to predict, but they are very important for designing for an earthquake's effects.

Soil properties of local soil deposits can alter a ground motion's frequency and amplification. Figure *2-5* demonstrates this phenomenon. Site A and site B have identical geometries, but site B is considerably stiffer than site A. The softer site (site A) will amplify low-frequency, or high-period, ground motions more than the stiffer site (site B). The opposite amplification will occur with high-frequency, or low-period, ground motions (Steven L Kramer,

1996). The September 19, 1985 Mexico City earthquake is a good example of this soil amplification phenomenon. The earthquake (M_s = 8.1) caused only moderate damage in the area surrounding its epicenter near the Pacific coast of Mexico, but it severely damaged Mexico City located 350 km away. The soft clay lake deposits amplified the ground motions increasingly until it reached Mexico City (Dobry & Vucetic, 1987).

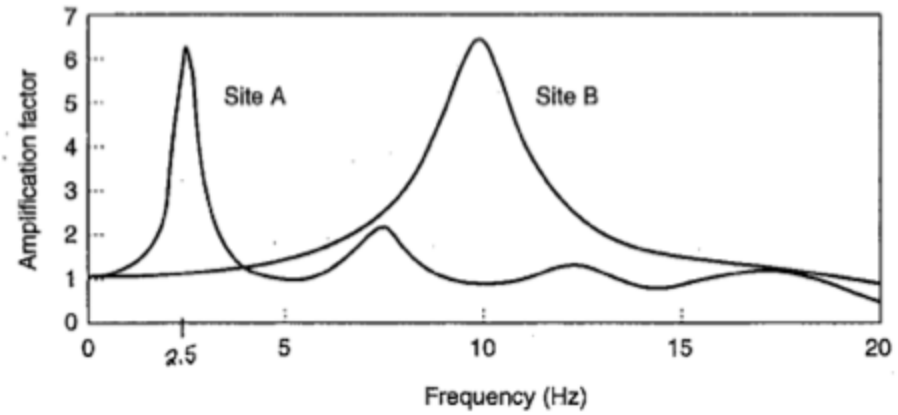

Figure 2-5: Amplification functions for two different sites (Kramer 1996).

Near-source and directivity are also very influential local site effects. They tend to be lumped together as one, although they are independent phenomena. Both phenomena have been known to significantly alter ground motions within about 10 km of a rupturing fault. Small earthquakes are usually modeled as point processes because their rupture lengths only span a few kilometers. However, large earthquakes can have rupture lengths of hundreds of kilometers. The earthquake will rupture with different strengths in different directions creating directivity effects (Ben-Menachem, 1961; Benioff, 1955). Directivity is caused by constructive interference of waves produced by successive dislocations that produce strong pulses of large displacements (Benioff, 1955; Singh, 1985) (Figure *2-6*).

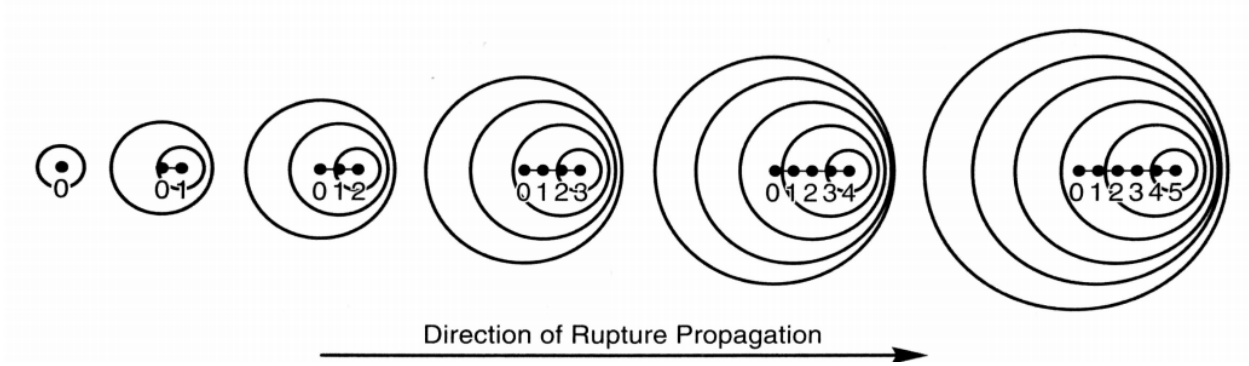

Figure 2-6: Schematic illustration of directivity effect of motions at sites toward and away from direction of fault rupture (Kramer, 1996).

Site topography can also influence the magnitude of ground motion parameters. For example, crests and ridges have been known to amplify ground motion parameters as they move up the peak. Amplification of ground motions near the crest of a ridge was measured in five different earthquakes in Matsuzaki, Japan (Jibson, 1987). Figure *2-7* depicts the normalized peak accelerations from this study. The average peak acceleration was about 2.5 times the average base acceleration. These effects are not usually accounted for due to complexity and the fact not many structures are built on the crest of mountains. However, a finite element analysis can be used for critical structures.

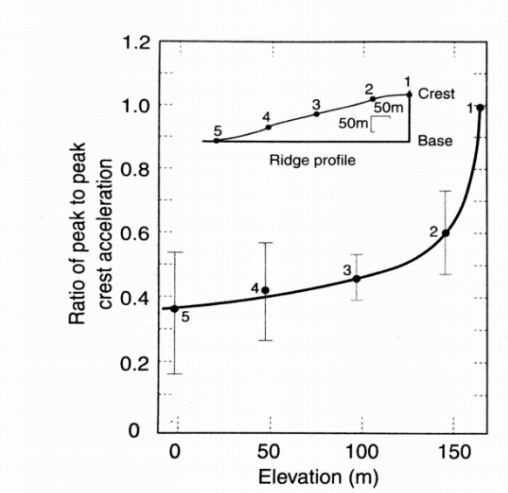

Figure 2-7: Normalized peak accelerations (means and error bars) recorded on mountain ridge at Matsuzaki, Japan (Jibson, 1987).

Basin effects are very important because many cities are built near or on alluvial valleys. The curvature of basin edges with soft alluvial soils can trap body waves causing propagation of increased surface waves and longer shaking durations (Vidale & Helmberger, 1988). Currently, shallow basin effects are relatively easy to predict, but predictions become complicated on the edges of basins and within deep basins.

2.5 Chapter Summary

Understanding seismic loading and the capability to predict it is crucial to predict earthquake hazards, including soil liquefaction. Seismic loading can be quantified into ground motion parameters. The most commonly used ground motion parameters include amplitude, frequency, and duration. Ground motion parameters can be significantly affected by local site effects.

3 REVIEW OF SOIL LIQUEFACTION

Liquefaction-induced settlements can have extreme economic effects. Liquefaction can cause differential settlement, which can be severely problematic for structures with shallow foundations, roadways, utility lines, and life lines. The resulting fire from the 1906 San Francisco earthquake showed how differential settlement can result in life-threatening tertiary hazards when life and utility lines are severed. After the earthquake, San Francisco firefighters had no access to water because the water mains had been severed in the earthquake. To provide the necessary background to understand liquefaction-induced settlements, soil liquefaction is reviewed in this chapter.

3.1 Liquefaction

Liquefaction is a complex phenomenon that has been closely studied for the past 50 years. It was not until the 1964 Alaska earthquake (M_w=9.2) and Niigata, Japan earthquake (M_s=7.5) occurred within three months of each other that liquefaction caught the attention of geotechnical engineers. Both earthquakes had intensive liquefaction-induced damage causing slope failures, bridge and building foundation failures, sinkholes, and flotation of buried structures (Steven L Kramer, 1996). In the past 30 years in particular, liquefaction has been studied intensively, resulting in many new prediction procedures, exploration technologies, and design methods.

Liquefaction, a term coined by Mogami and Kubo (1953), has been known to collectively reference soil phenomena related to deformations caused by disturbances of undrained cohesionless soils (Steven L Kramer, 1996). It is well known that dry cohesionless soils tend to densify under static or cyclic loading. If the cohesionless soil is saturated, this densification causes the pore water to be rapidly forced from the pore spaces causing a corresponding buildup of excess pore water pressure and a decrease in effective stress. The decrease in effective stress causes the soil to experience a temporary weakened state. If the effective stress reaches a null value, then liquefaction has initiated. Liquefaction will manifest itself as either flow liquefaction or cyclic mobility. Cyclic mobility is the most common and can occur a wide variety of site and soil conditions. Flow liquefaction has the most damaging effects but occurs less frequently because it requires specific site and soil characteristics. Both phenomena are discussed in more detail in sections 3.4.2 and 3.4.3.

A comprehensive liquefaction analysis should consider liquefaction susceptibility, initiation, and its corresponding effects. The remaining sections of this chapter will address each of these aspects of liquefaction individually.

3.2 Liquefaction Susceptibility

The first step in a liquefaction hazard analysis is to determine if a soil is even susceptible to liquefaction. If a soil is not susceptible to liquefaction, a hazard analysis is not needed. However, if a soil is susceptible, an initiation analysis should be performed. Susceptibility is judged by site historical information, geology, composition, and state. Each of these susceptibility criteria are addressed in detail in the following sections.

3.2.1 Historical Criteria

The liquefaction history of a particular site can predict a site's liquefaction susceptibility. When the groundwater and soil conditions remain the same, liquefaction will often occur at the same location it did in the past (T. L. Youd, 1984). Therefore, liquefaction case histories can be used to predict whether or not a site is susceptible to liquefaction. Youd (1991) describes multiple instances where this process has been used successfully.

3.2.2 Geologic Criteria

The hydrological environment, depositional environment, and age of a soil deposit all contribute to liquefaction susceptibility (T. L. Youd & Hoose, 1977). Because liquefaction occurs from pore water pressure build-up, liquefaction will only occur in saturated soils. Therefore, soils must be below the water table to be susceptible to liquefaction. Saturated uniform cohesionless soil particles placed in a loose state are most susceptible to soil liquefaction. Therefore, saturated alluvial, fluvial, colluvial, and aeolian deposits tend to be highly susceptible. Soil age also affects liquefaction susceptibility. The susceptibility of newer deposits are generally more susceptible than older deposits.

Man-made deposits can also be susceptible to liquefaction. If a fill is placed without compaction, it will be susceptible because of the loose state of the non-compacted soil particles. Well-compacted fills will present a lower seismic liquefaction hazard.

3.2.3 Compositional Criteria

Liquefaction susceptibility is affected by compositional characteristics that influence volume change behavior, including particle shape, size, and gradation (Steven L Kramer, 1996). Liquefaction is known to occur when soils begin to densify and water is essentially pushed out of

the pore spaces. If pore water cannot escape quickly enough, the pore water will begin to push back, generating excess pore water pressure.

Particle shape, size, and gradation affect a soil's densification ability and consequently its liquefaction susceptibility. Excess pore water pressures can only develop in soils that can densify easily. If a soil cannot densify easily, or has high permeability that cannot sustain pore water pressures, it is unlikely to liquefy. Smooth, rounded particles densify more easily than coarse and jagged particles, indicating a higher susceptibility to liquefaction. Coarse and jagged particles will interlock with each other resisting densification. Gradation also affects liquefaction susceptibility. Poorly graded soils are more likely to liquefy than well graded soils. The voids in well graded soils are filled with fines, resulting in less volume change under drained conditions and consequently less pore water pressure under undrained conditions.

Fine-grained soils have generally been considered not susceptible to liquefaction due to cohesion, but recent studies have found these soils could potentially still liquefy. Cohesion is a chemical and electrical attraction between fine-grained soil particles that hold the particles together. This cohesion is generally sufficient to prevent liquefaction initiation. However liquefaction has been observed to occur in coarse fines with low to no plasticity and low cohesion (K. Ishihara, 1984, 1985). Boulanger and Idriss (2005) reviewed case histories and laboratory tests of cyclically loaded fine-grained soils. Boulanger and Idriss identified two types of soil behavior of fines, "sand-like" and "clay-like", based on stress-strain behavior and stress-normalization. If a fine-grained soil exhibited "sand-like" behavior it was susceptible to liquefaction. Boulanger and Idriss found that the lower the plasticity of a soil, the more "sand-like" behavior it exhibited and is susceptible to liquefaction.

3.2.4 State Criteria

The initial state of a soil, or its stress and density characteristics, can have a significant impact on liquefaction susceptibility. Even if a soil is considered liquefiable by all of the previous criteria, its initial state could still prevent liquefaction from occuring. A soil loosely placed is more likely to be contractive and therefore liquefiable, while a soil densely compacted is more likely to be dilative and therefore not liquefiable.

Casagrande (1936) pioneered the understanding of soil behavior under various confining pressures across various densities. His research showed all specimens, under the same confining pressure, converged to the same density when sheared. Loose specimens contracted, or densified, initially, while dense specimens initially contracted. However, both specimens converge to the same void ratio (or relative density) at large strains, representing a steady or critical state. This phenomenon is illustrated in Figure *3-1*.

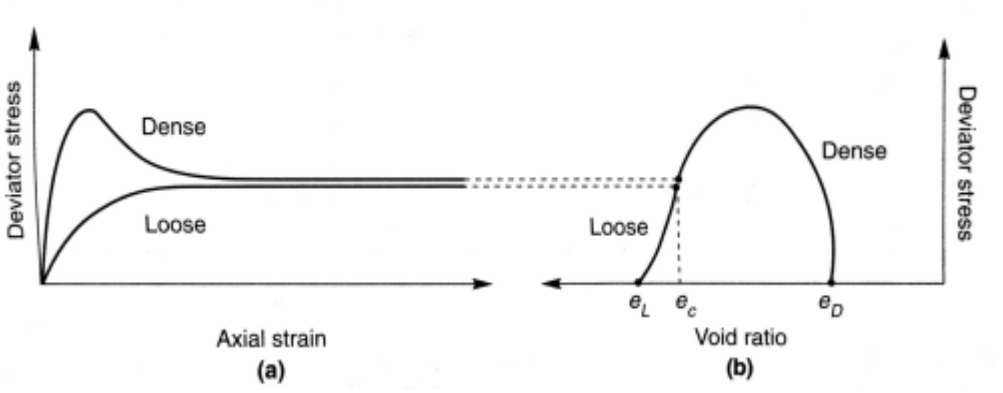

Figure 3-1:(a) Stress-strain and (b) stress-void ratio curves for loose and dense sands at the same confining pressure (Kramer, 1996).

The critical void ratio (e_c) is the void ratio corresponding to the density at the steady or critical state. This discovery led to Casagrande's idea of the critical void ratio (CVR) line, which is the critical void ratios plotted for a range of effective confining pressures. The CVR is a boundary line between loose (contractive) and dense (dilative) soils, or susceptible and nonsusceptible soils respectively, as shown in Figure *3-2*.

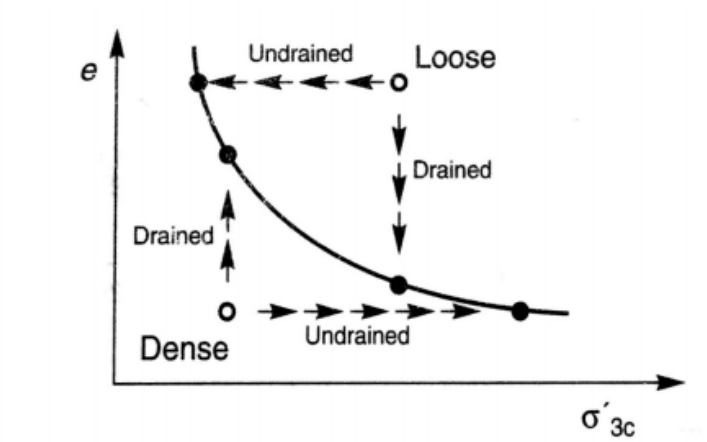

Figure 3-2: Behavior of initially loose and dense specimens under drained and undrained conditions (Kramer, 1996).

In 1938 the failure of the Fort Peck Dam in Montana proved the CVR line to be an insufficient method for predicting liquefaction susceptibility (Middlebrooks, 1942). The dam had a flow liquefaction failure even though the initial state of the soils before liquefaction plotted below the CVR line (i.e., in the nonsusceptible region). Casagrande concluded the failure was due to the inability of a strain-controlled drained test to emulate all the phenomena that influences soil behavior under the stress-controlled undrained conditions of an actual flow liquefaction failure.

It was not until 1969 that Castro, one of Casagrande's students, was able to effectively replicate soil flow liquefaction. At this time, technology gained the ability to perform stress-

controlled undrained tests. Castro performed various static and cyclic triaxial tests, which helped him discover the steady state of deformation (Castro & Poulos, 1977; Poulos, 1981). The steady state of deformation describes the soil state in which it flows continuously under constant shear stress and constant effective confining pressure at constant volume and velocity.

The steady-state line (SSL) can be plotted and viewed as a three-dimensional curve in the e- $\boldsymbol{\sigma}$'- $\boldsymbol{\tau}$ space (Figure *3-3*), to predict flow liquefaction susceptibility. The SSL can also be projected onto a plane of the steady-state strength (S_{su}) or confining pressure versus void ratio, as shown in Figure 3-3.

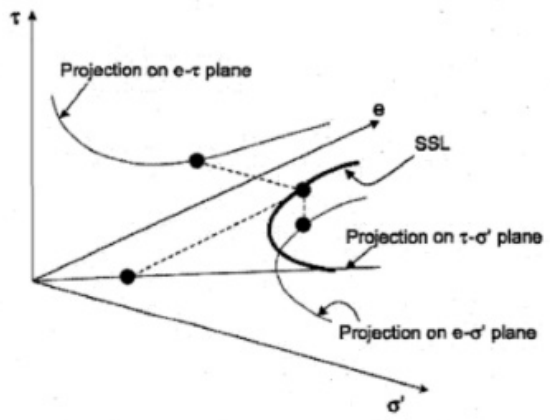

Figure 3-3: Three-dimensional steady-state line showing projections on the e-τ plane, e-σ' plane, and τ -σ' plane (Kramer, 1996).

When plotted logarithmically, the strength-based SSL is parallel to the effective confining pressure-based SSL. This relationship is because the shearing resistance of a soil is proportional to the effective confining stress. Soils that plot below the SSL are not susceptible to flow liquefaction. A soil will be susceptible to flow liquefaction if it plots above the SSL and only if the stress exceeds its steady state strength. It is important to note the SSL is only effective in predicting flow liquefaction and cannot predict cyclic mobility (Steven L Kramer, 1996).

The SSL is limited however, because it applies the absolute measure of density for characterization of flow liquefaction susceptibility. As shown in Figure *3-4*, a soil at one particular density could be considered liquefiable at a very high confining pressure but not susceptible to flow liquefaction at a low confining pressure.

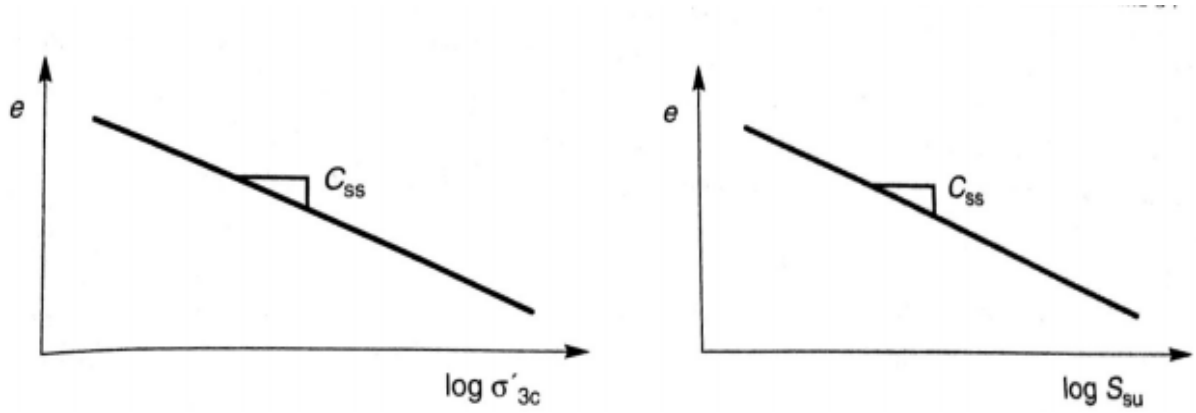

Figure 3-4: State criteria for flow liquefaction susceptibility based on the SSL for confining pressure (left) or stead-state strength (right), plotted logarithmically (Kramer, 1996).

To address this limitation of the SSL, Roscoe and Pooroshasb believed the behavior of cohesionless soils should be related to the proximity of the soil's initial state to the SSL. In other words, soils with similar proximities to the SSL should behave similarly. Using this idea, Been and Jefferies (1985) developed a state parameter (ψ). The state parameter can be defined as the initial state void ratio subtracted by the void ratio on the SSL at the confining pressure of interest (Figure *3-5*). If the state parameter is positive, the soil is contractive and therefore may be susceptible to flow liquefaction. If the state parameter is negative, the soil is dilative and not

susceptible to flow liquefaction. It is important to note, however, that the accuracy of the state parameter is dependent on the accuracy of the position of the SSL.

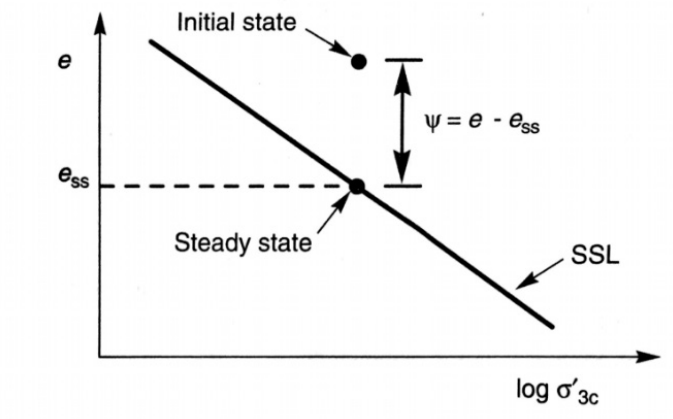

Figure 3-5: State Parameter (Kramer, 1996).

3.3 Liquefaction Initiation

Even if a soil meets all of the susceptibility criteria stated above, it is still possible for liquefaction not to occur in a specific earthquake. The earthquake must create large enough disturbances to initiate liquefaction. Both flow liquefaction and cyclic mobility are very different phenomena that, in discussing liquefaction initiation, need to be discussed separately. Both, however, can be described easily in stress path space (Hanzawa, 1979) using the three-dimensional surface called the slow liquefaction surface (FLS). Understanding of the FLS, flow liquefaction, and cyclic mobility are discussed in detail below.

3.3.1 Flow Liquefaction Surface

The conditions of flow liquefaction can be understood most easily when evaluating the response of an isotopically consolidated specimen of loose saturated sand in an undrained triaxial test under monotonic loading. Figure *3-6* demonstrates the stress path of such a specimen under monotonic loading. The initial state, prior to loading, of the specimen is plotted well above the SSL (point A). This indicates the soil will exhibit contractive behavior and is therefore susceptible to flow liquefaction. Prior to loading, the soil has no excess pore water pressure or any strain. Once loading begins, the sample will have an increase of shear strength until it reaches a maximum shear strength (point B). If loading persists past the peak strength, the sample will exhibit a drastic decrease in strength, becoming unstable and will collapse. This drastic decrease in strength will result in a rapid increase of excess pore water pressure and excess strains until the soil reaches a steady-state residual strength (point C). The soil has just experienced flow liquefaction. Flow liquefaction occurred at point B, when the soil became irreversibly unstable (Steven L Kramer, 1996).

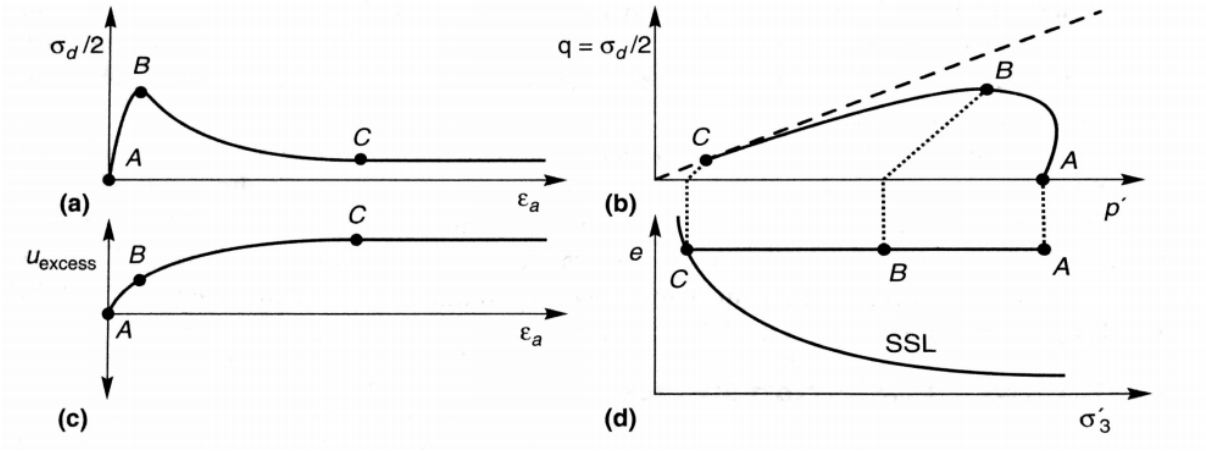

Figure 3-6: Response of isotropically consolidated specimen of loose, saturated sand: (a) stress-strain curve; (b) effective stress path; (c) excess pore pressure; (d) effective confining pressure (Kramer, 1996).

Now consider the same test applied to multiple samples at the same void ratio, but at varying effective confining pressures. Since all of the specimens have the same void ratio, they will all reach the same effective stress conditions at the steady-state, but they will all follow different paths to get there (Steven L Kramer, 1996). Figure *3-7* illustrates this response from five different specimens. Sample A and B have initial states below the SSL and therefore exhibit dilative behavior. Neither sample A or B reached flow liquefaction because of their initial effective confining pressure, but they did dilate and settle at the steady-state point. However, samples C, D, and E did achieve flow liquefaction because their initial state plotted above the SSL. Each specimen reached a peak undrained shear strength (marked with an *x*), followed by a rapid decrease in strength and settled at the steady state point.

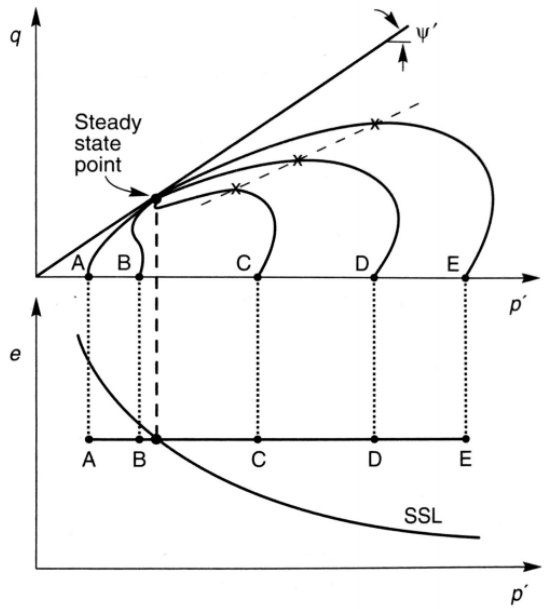

Figure 3-7: Response of five specimens isotopically consolidated to the same initial void ratio at different initial effective confining pressures (Kramer, 1996).

Hanzawa et al. (1979) and Vaid and Chern (1983) found each initiation point can be connected by a projected straight line that projects through the origin of the stress path. This projected line creates the FLS and flow liquefaction occurs below this line. Figure *3-8* shows the orientation of the flow liquefaction surface in the stress path space.

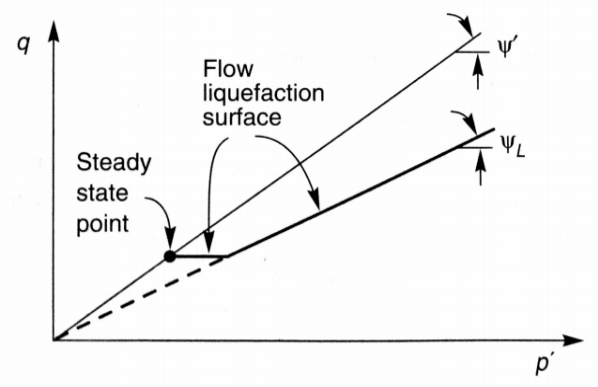

Figure 3-8: Orientation of the flow liquefaction surface in stress path space (Kramer, 1996).

The FLS applies to not only monotonic loading but also cyclic loading (Vaid & Chern, 1983). Two identical specimens will both liquefy when their stress paths reach the FLS, independent from how they are loaded. Figure *3-9* demonstrates this phenomenon. Two identical loose saturated sand specimens were tested, one under monotonic loading and one under cyclic loading. The monotonically loaded specimen is represented by path ABC and behaved according to the phenomenon discussed above. The effective stress path of the cyclically loaded specimen is represented by path ADC. As the specimen is loaded, it builds up pore water pressure with each cycle until it reaches the FLS. At that point, flow liquefaction is initiated.

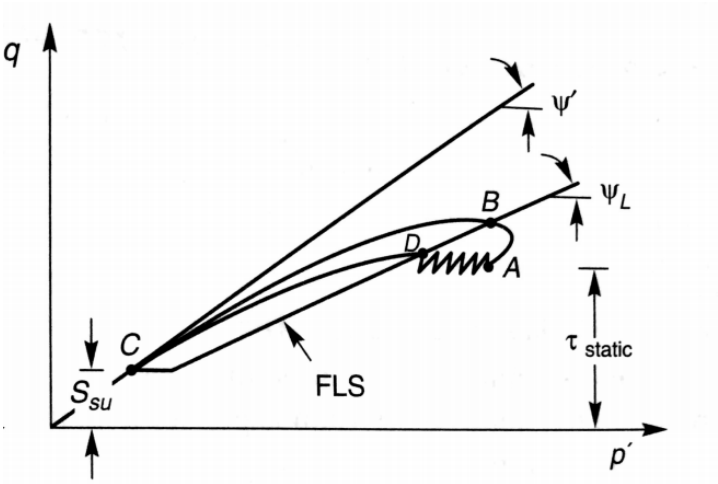

Figure 3-9: Initiation of flow liquefaction by cyclic and monotonic loading (Kramer, 1996).

Even though the effective stress conditions at the liquefaction initiation points (points B and D) were different, they both experience flow liquefaction at the FLS. This indicates the FLS marks the boundary between stable and unstable soil conditions. Lade (1992) developed a more detailed description of this instability using continuum mechanics.

3.3.2 Flow Liquefaction

Flow liquefaction will only have the potential to occur when the shear stress required for static equilibrium is greater than the steady-state strength. The shear stresses in the field are caused by gravity and will therefore remain constant until large deformations develop. If a soil's initial state plots within the shaded region in Figure *3-10*, it will be susceptible to flow liquefaction. For flow liquefaction to occur, there must be a large enough undrained disturbance to move the effective stress path to the FLS.

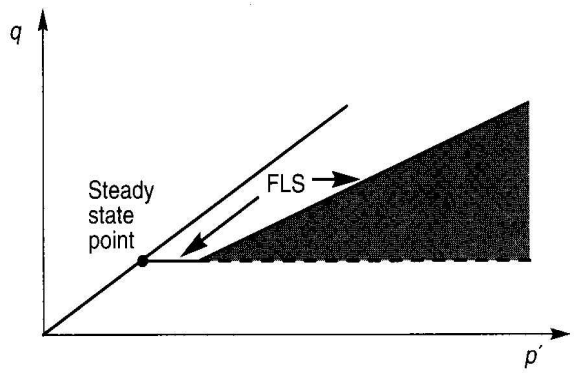

Figure 3-10: Zone of susceptibility to flow liquefaction (Kramer, 1996).

3.3.3 Cyclic Mobility

Unlike flow liquefaction, cyclic mobility can occur when the initial effective stress point is below the steady-state strength line. Therefore, initial states that plot below the steady-state point are susceptible to cyclic mobility (Figure *3-11*). The shaded region extends from very high to very low effective confining stress. This indicates both loose and dense soils are susceptible to cyclic mobility because soils across this region would plot both above and below the SSL.

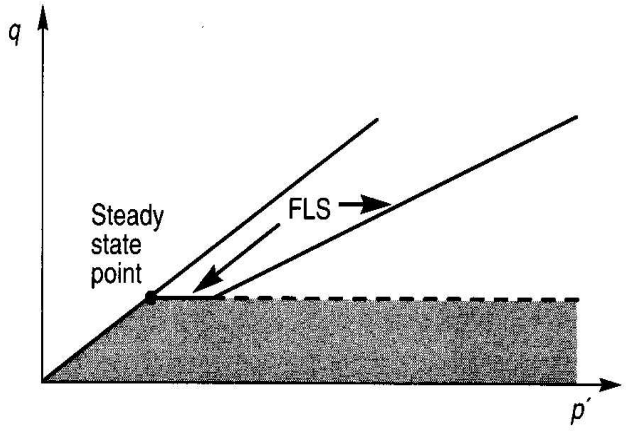

Figure 3-11: Zone of susceptibility to cyclic mobility (Kramer, 1996).

There are three combinations of initial conditions and cyclic loading conditions that lead to cyclic mobility (Figure *3-12*). The first condition (Figure *3-12*(a)) will occur when the static shear stress is greater that the cyclic shear stress; in other words, no shear stress reversal occurs. There is also no exceedance of steady-state strength as the effective stress path moves to the left until it reaches the drained failure envelope and continues to move up and down the failure envelope with additional loading cycles. This results in a stabilization of the effective stress conditions, but the effective confining pressure has decreased significantly, resulting in large permanent strains occurring within each load cycle.

The second case will occur when there is no shear stress reversal, but the steady-state strength is momentarily exceeded (Figure *3-12*(b)). With each load cycle, the effective stress path will move to the left until it reaches the FLS. Momentary periods of instability occur, resulting in significant permanent strains.

The third possible condition occurs when stress reversal occurs, but the steady-state strength is not exceeded (Figure *3-12*(c)). The shear stress changes direction in this case, causing both compressional and extensional loading. Increasing rate of pore pressure generation correlates with an increase degree of stress reversal (Mohamad & Dobry, 1986), resulting in the effective stress path moving relatively quickly to the left. Once the effective stress path reaches the FLS, it oscillates along the compressional and extensional portions of the drained failure envelope. Every time it passes through the origin, it reaches a state of zero effective stress causing large permanent strains.

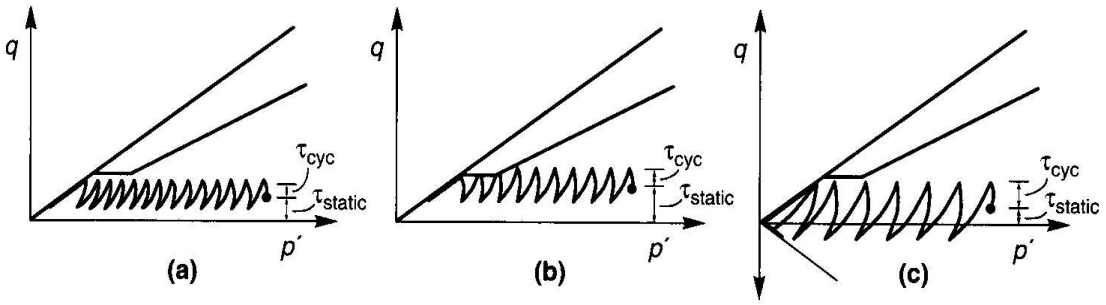

Figure 3-12: Three cases of cyclic mobility: (a) no stress reversal and no exceedance of the steady-state strength; (b) no stress reversal with momentary periods of steady-state strength exceedance; (c) stress reversal with no exceedance of steady-state strength (Kramer, 1996).

Flow liquefaction occurs at a specific point, but there is no clear point at which cyclic mobility occurs. Large deformations and strains from cyclic mobility occur incrementally. The magnitude of strain deformations depends on duration and magnitude of soil loading. Cyclic mobility will cause the most damage to sloping sites subjected to a long duration of ground motions. However, for level sites subjected to short duration ground motions, the expected resulting strains will be small.

3.4 Methods to Predict Liquefaction Triggering

Liquefaction initiation can be quantified and predicted by calculating liquefaction triggering. Liquefaction triggering can be expressed as a factor of safety against liquefaction (FS_L) or a probability of liquefaction triggering (P_L). This factor of safety represents the ratio of a soil's ability to resist liquefaction to the loading demand from an earthquake. Many liquefaction triggering models have been developed, but the most prominent models, and the models used for this study, are presented in this section.

3.4.1 Empirical Liquefaction Triggering Models

When calculating FS_L, engineers rely predominately upon a simplified empirical procedure by calculating the ratio of resistance to liquefaction to the seismic demand on the soil (Seed, 1979; Seed & Idris, 1982). According to this procedure, liquefaction triggering is evaluated by:

$$FS_L = \frac{capacity}{demand} = \frac{CRR}{CSR} \tag{3-1}$$

where *CRR* represents the cyclic resistance ratio and the *CSR* represents the cyclic stress ratio. The *CSR* represents the characterization of the earthquake loading and can be computed by:

$$CSR = 0.65\frac{a_{max}}{g}\frac{\sigma_v}{\sigma'_v}(r_d) * \frac{1}{k_\sigma} * \frac{1}{MSF} \tag{3-2}$$

where $a_{max}$is the peak ground surface acceleration as a fraction of gravity, σ_v is the total vertical stress, σ'_v is the vertical effective stress, r_d is the stress reduction factor, k_σ is the overburden correction factor, and *MSF* is the magnitude scaling factor. Various methods calculate these variables for the *CSR* differently and will be discussed in the next sections.

The *CRR* represents a soil's ability to resist liquefaction and is a function of the corrected normalized equivalent clean sand CPT penetration resistance [$(q_{c1N})_{cs}$]. Stiffer soil will result in a higher *CRR* value, which will result in a higher FS_L, meaning less of a chance to liquefy. Various correlations have been produced to calculate $(q_{c1N})_{cs}$ differently and therefore produced differing *CRR* values. Arguably, two of the most widely used CPT correlation methods are the Boulanger and Idriss (2014) and Robertson and Wride (2009) methods. Each of these procedures are explained in detail in the next sections.

3.4.2 Robertson and Wride (1998, 2009) Procedure

Until recent years, most liquefaction assessments for the CPT were calculated based on CPT to SPT correlations, but the increased usage of the CPT initiated an increase of CPT assessment methods. One of the most widely used CPT liquefaction triggering procedures is the Robertson and Wride (1998), which was updated to the Robertson and Wride (2009) procedure. This procedure uses all of the available CPT data variables [cone tip resistance (q_c), sleeve friction (f_s), pore pressure (u), and depth] to calculate a corrected normalized equivalent clean sand CPT penetration resistance, Q_{tncs} [e.g. $(q_{c1N})_{cs}$] based on correlations from case history data. Robertson and Wride used these Q_{tncs} values to develop a deterministic *CRR* curve, which represents a boundary between cases that are expected to liquefy and those which are not expected to liquefy (Figure 3-13).

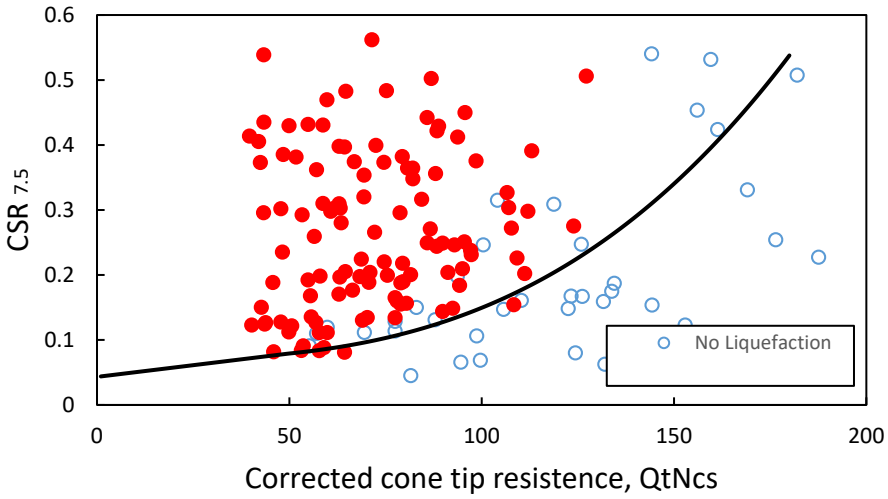

Figure 3-13: Robertson and Wride (2009) liquefaction triggering curve with case history data points.

Once the *CRR* is defined it is then possible to make a prediction of liquefaction triggering by plotting the CPT resistance and the *CSR* calculated at a depth of interest for a certain earthquake event. If the point plots above the *CRR* curve it is expected that the factor of safety

against liquefaction (FS_L) will be greater than 1 and thus not expected to liquefy. Conversely, if the point plots below the curve, FS_L will be less than 1 and liquefaction will be predicted.

To obtain a *CRR*, Q_{tncs} must be calculated. To calculate the Q_{tncs}, the Robertson and Wride method is an iterative process (Figure *3-15*). To start an initial stress exponent, *n*, is calculated using:

$$n = 0.381(I_c) + 0.05\left(\frac{\sigma'_{vo}}{P_o}\right) - 0.15 \qquad (3\text{-}3)$$

where I_c is the soil behavior index. The soil behavior index is an indicator of how much a soil will behave like a fine-grained soil compared to a coarse grained material. Robertson (1990) found a correlation for the I_c from the q_c and f_s. This relationship can be summarized with the soil behavior chart (Jefferies & Davies, 1993; Robertson, 1990) shown in Figure *3-14*.

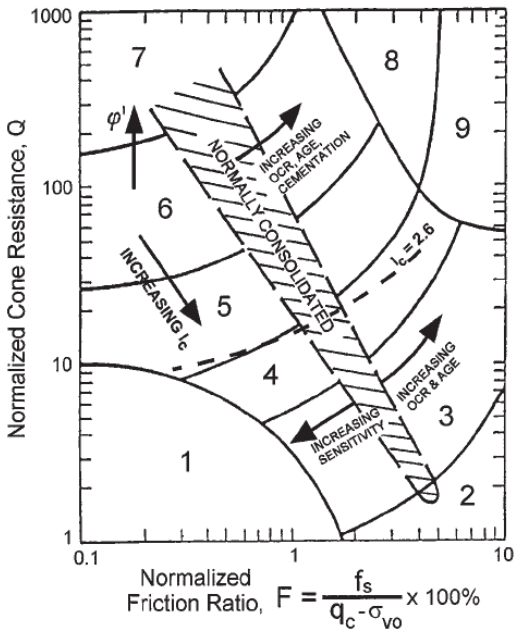

Figure 3-14: Normalized CPT soil behavior type chart (after Robertson, 1990). Soil types: 1, sensitive, fine grained; 2, peats; 3, silty clay to clay; 4, clayey silt to silty clay; 5, silty sand to sandy silt; 6, clean sand to silty sand; 7, gravelly sand to dense sand; 8, very stiff sand to clayey sand; 9, very stiff, fine grained.

I_c cannot be calculated directly, so an initial seed I_c value is used to start the iterative process. Using this seed value, n is calculated from Equation (3-3) and then used to calculate the overburden stress correction factor, C_N as:

$$C_N = \left(\frac{P_a}{\sigma_{vo}}\right)^n < 2.0 \tag{3-4}$$

The I_c value is then calculated as:

$$I_c = [(3.47 - \log(Q))^2 + (\log(F) + 1.22)^2]^{0.5} \tag{3-5}$$

where

$$Q = \left[\frac{q_t - \sigma_{vo}}{P_a}\right] * C_N \tag{3-6}$$

and

$$F_r = \frac{f_s}{(q_t - \sigma_{vo})} * 100 \tag{3-7}$$

Using the newly calculated I_c, from Equation (3-5), n is recalculated using Equation (3-3). This process is repeated until the change in n (Δn) is less than 0.01. Once $\Delta n < 0.01$, all current calculated values of Q, F_r, and I_c are used to calculate $Q_{tn,cs,}$ which is calculated using:

$$Q_{tn,cs} = K_c * Q_{tn} \tag{3-8}$$

where K_c is calculated using:

$$K_c = \begin{cases} K_c = 1.0 & if\ I_c \leq 1.64 \\ K_c = 5.58{I_c}^3 - 0.403{I_c}^4 - 21.63{I_c}^2 + 33.75I_c - 17.88 & if\ 1.64 < I_c < 2.60 \\ K_c = 6 * 10^{-7}(I_c)^{16.76} & if\ 2.50 < I_c < 2.70 \end{cases} \tag{3-9}$$

CRR is calculated using:

$$CRR_{7.5} = 93\left[\frac{Q_{tn,cs}}{1000}\right]^3 + 0.08 \tag{3-10}$$

However, Equation (3-10) is only valid if I_c <2.70, if $I_c \geq 2.70$, then K_c is not used and *CRR* is calculated as:

$$CRR_{7.5} = 0.053 * Q_{tn,cs} \tag{3-11}$$

This *CRR* value is then used to calculate the factor of safety against liquefaction. A summary flowchart of the Robertson and Wride (2009) procedure for computing *CRR* is presented in Figure 3-15.

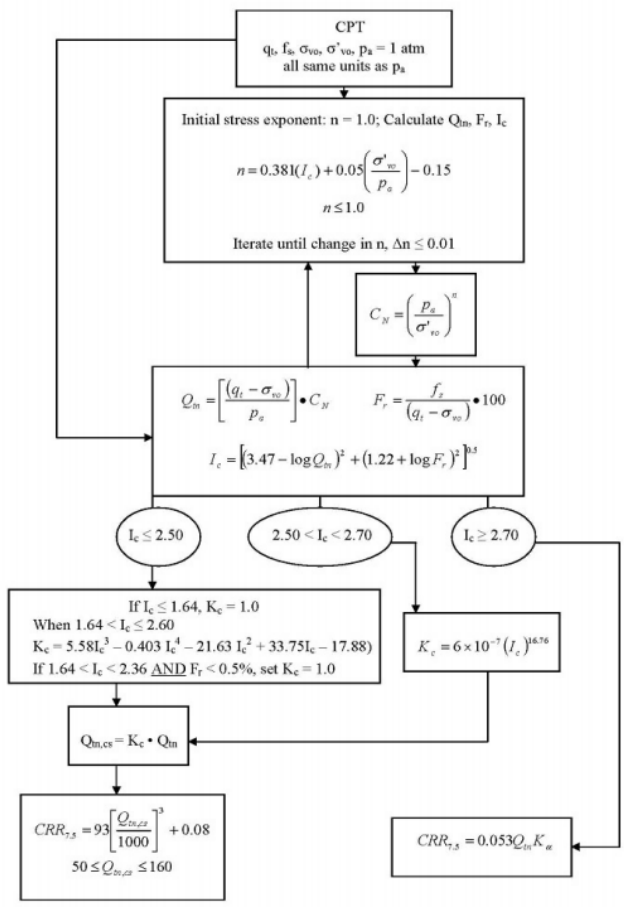

Figure 3-15: Summary of the Robertson and Wride (2009) *CRR* procedure.

Robertson and Wride (2009) presents a procedure to calculate the *CSR*. Robertson and Wride (2009) utilize Equation (3-2) to calculate the *CSR*, but calculates the *MSF*, r_d, and K_σ factors uniquely. Many values for *MSF* have been suggested by various researchers (Seed and Idriss, 1982; Ambraseys, 1988), however, the Robertson and Wride method uses the lower-bound equation values suggested by Youd et al. (2001):

$$MSF = \frac{10^{2.24}}{M_w{}^{2.56}} \tag{3-12}$$

where M_w is the moment magnitude of the earthquake loading. The value r_d is a depth dependent shear stress reduction factor. The Robertson and Wride procedure calculates the r_d, based on the work of Liao and Whitman (1986), Robertson and wride (1998), and Seed and Idriss (1971), as:

$$r_d = \begin{cases} 1.0 - 0.00765z & for\ z \leq 9.15m \\ 1.174 - 0.0267z & for\ 9.15m < z \leq 23m \\ 0.744 - 0.008z & for\ 23m < z \leq 30m \\ 0.5 & for\ z > 30m \end{cases} \tag{3-13}$$

where z is the depth of interest in meters. Finally, to calculate the K_σ, Robertson and Wride utilizes the procedure from Idriss et al. (2001):

$$K_\sigma = \left(\frac{\sigma_{vo}{}'}{P_a}\right)^{(f-1)} \tag{3-14}$$

where $\sigma_{vo}{}'$ is the effective overburden pressure, P_a is atmospheric pressure in the same units and f is an exponent that is a function of site conditions. After *CRR* and *CSR* are calculated FS_L can be computed using Equation (3-1).

3.4.3 Ku et al. (2012) Procedure [Probabilistic Version of Robertson and Wride (2009) Method]

Because of the increased usage and popularity of the Robertson and Wride (2009) liquefaction triggering procedure, the need for a probabilistic version of this method was needed. Ku et al. (2012) developed a probabilistic model of the Robertson and Wride (2009) method through statistical analysis of the Robertson and Wride (2009) liquefaction triggering case histories. The goal of this new model was to create a probabilistic method that could be easily integrated into current reliability or performance-based design practices.

Ku et al. developed a function to relate FS_L (from the Robertson and Wride method) to a probability of liquefaction P_L. This function was intended to provide a smooth transition of integrating a probabilistic method into current design methods. By using the Bayesian statistical analysis of a case history database and the principle of maximum likelihood, Ku et al. developed the following relationship:

$$P_L = 1 - \Phi\left[\frac{0.102 + \ln(FS_L)}{\sigma_m}\right] \quad (3\text{-}15)$$

where Φ is the standard normal cumulative distribution function, and σ_m is the model based uncertainty and is equal to 0.276. This relationship between FS_L and P_L can be viewed visually in Figure *3-16*. The curve indicated by the "RW" represents the Robertson and Wride (2009) deterministic triggering curve.

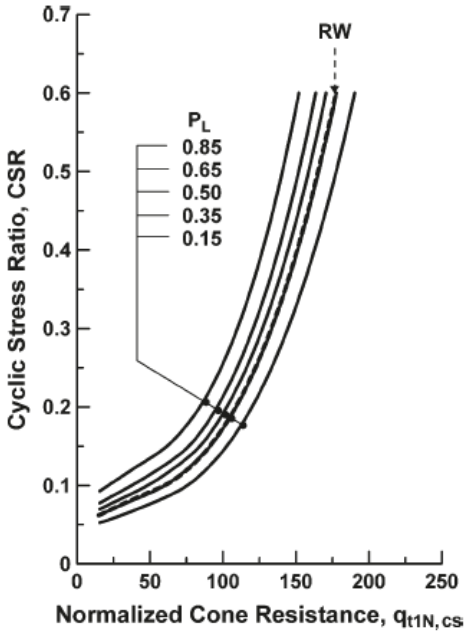

Figure 3-16: CRR liquefaction triggering curves based on P_L.

3.4.4 Boulanger and Idriss (2014) Procedure

The Boulanger and Idriss (2014) procedure calculates the q_{c1Ncs} differently than the Robertson and Wride (2009) procedure, which results in a different calculated *CRR* value. Boulanger and Idriss gathered together a database of old and recent (up through 2011) earthquake data. Using this database, Boulanger and Idriss created a new correlation between CPT data and the *CRR* for an earthquake.

Just like the Robertson and Wride method, the Boulanger and Idriss method requires an iterative calculation for q_{c1Ncs}. The method starts by correcting for overburden pressure as:

$$q_{c1N} = C_N \frac{q_c}{P_a} \tag{3-16}$$

where q_c is CPT cone tip resistance, $P_a$is atmospheric pressure, and $C_N$is the overburden correction factor calculated as:

$$C_N = \left(\frac{P_a}{\sigma'_v}\right)^m \leq 1.7 \tag{3-17}$$

where $\sigma'_v$is the vertical effective stress and m is calculated as:

$$m = 1.338 - 0.249(q_{c1Ncs})^{0.264} \tag{3-18}$$

and where q_{c1Ncs} is limited to values between 21 and 254. To start the iteration, an initial seed value of q_{c1Ncs} is specified, and Equations (3-16) through (3-18) are iteratively repeated until the change in q_{c1Ncs} is less than 0.5. Throughout the iterative process, the normalized clean-sand cone tip resistance (q_{c1Ncs}) value is calculated as:

$$q_{c1Ncs} = q_{c1N} + \Delta q_{c1N} \tag{3-19}$$

where Δq_{c1N} is the fines content adjustment factor, Δq_{c1N} is calculated as:

$$\Delta q_{c1N} = \left(11.9 + \frac{q_{c1N}}{14.6}\right) \exp\left(1.63 - \frac{9.7}{FC + 2} - \left(\frac{15.7}{FC + 0.01}\right)^2\right) \tag{3-20}$$

where *FC* is the percentage of fines within the soil. To obtain *FC* from the CPT, Idriss and Boulanger suggest using the *FC* and I_c correlation from the Robertson and Wride (1998) procedure. However, Idriss and Boulanger suggest approaching this relationship with caution due to the data scatter. Idriss and Boulanger suggest calculating *FC* as:

$$FC = 80(I_c + C_{FC}) - 137$$
$$0\% \leq FC \leq 100\% \tag{3-21}$$

where I_c is the soil behavior type index calculated from the Robertson and Wride procedure, and C_{FC} is a regression fitting parameter that can be used to minimize uncertainty when site-specific fines content data is available. Figure *3-17* is a plot of the relationship between *FC* and I_c along with the associated data scatter.

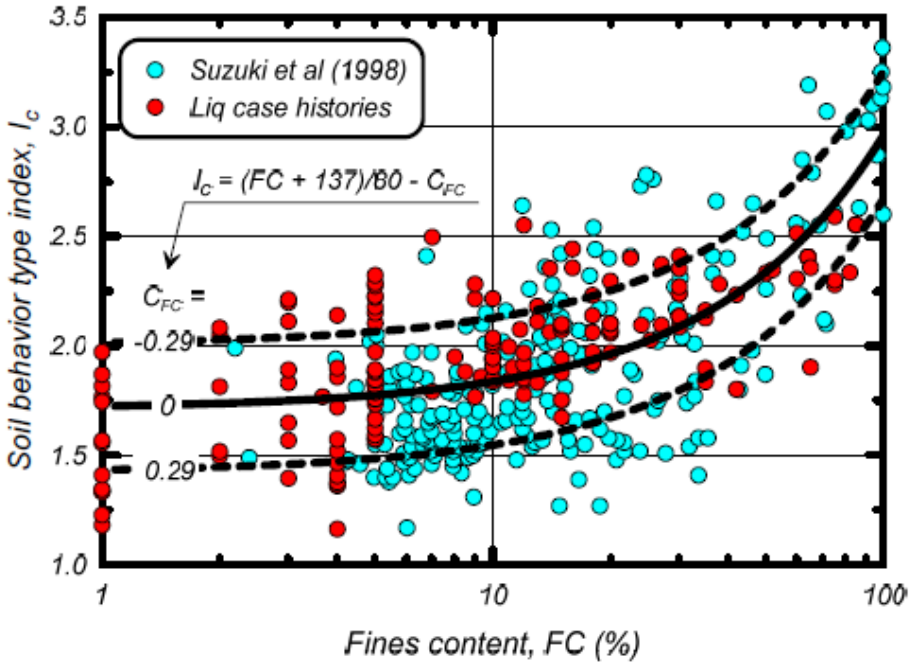

Figure 3-17: Recommended correlation between Ic and FC with plus or minus one standard deviation against the dataset by Suzuki et al. (1998) (after Idriss and Boulanger, 2014).

After the iteration has been completed to the desired level of accuracy, the *CRR* is then calculated. For the Boulanger and Idriss method, the *CRR* is calculated as:

$$CRR_{M=7.5,\sigma'_{vo}=1atm} = \exp\left(\frac{q_{c1Ncs}}{113} + \left(\frac{q_{c1Ncs}}{1000}\right)^2 - \left(\frac{q_{c1Ncs}}{140}\right)^3 + \left(\frac{q_{c1Ncs}}{137}\right)^4 - 2.8\right) \quad (3\text{-}22)$$

Idriss and Boulanger presents a procedure to calculate the *CSR*. Idriss and Boulanger utilize Equation (3-2), just as the Robertson and Wride (2009) procedure, but implements different methods to calculate the *MSF*, r_d, and K_σ. Idriss and Boulanger (2014) developed a relationship to calculate the *MSF* by combining past MSF relationships (Idriss, 1999; Boulanger and Idriss, 2008). This new *MSF* relationship is calculated as:

$$MSF = 1 + (MSF_{max} - 1)\left(8.64 \exp\left(\frac{-M}{4}\right) - 1.325\right) \tag{3-23}$$

$$MSF_{max} = 1.09 + \left(\frac{q_{c1Ncs}}{180}\right)^3 \leq 2.2 \tag{3-24}$$

where *M* is the moment magnitude of the scenario earthquake and q_{c1Ncs} is the corrected cone tip resistance for the Idriss and Boulanger (2014) method. This new relationship allows for soil characteristics to be represented by CPT cone tip resistance and was found to improve the degree of fit between CPT-based liquefaction triggering correlation and their respective history databases (Idriss and Boulanger, 2014).

The Idriss and Boulanger procedure calculates r_d by using the equations of Golesorkhi (1989):

$$r_d = \exp[\alpha(z) + \beta(z) * M] \tag{3-25}$$

$$\alpha(z) = -1.012 - 1.126 \sin\left(\frac{z}{11.73} + 5.133\right) \tag{3-26}$$

$$\beta(z) = 0.106 + 0.118 \sin\left(\frac{z}{11.28} + 5.142\right) \tag{3-27}$$

where *z* is the depth below the ground surface in meters, *M* is the moment magnitude of the scenario earthquake, and the arguments within the trigonometric functions are in radians.

The K_σ factor in the Boulanger and Idriss method is calculated using the procedure developed by Boulanger (2003):

$$k_\sigma = 1 - C_\sigma \ln\left(\frac{\sigma'_v}{P_a}\right) \leq 1.1 \tag{3-28}$$

$$C_\sigma = \frac{1}{37.3 - 8.27(q_{c1Ncs})^{0.264}} \leq 0.3 \tag{3-29}$$

Where $\sigma'_v$is the vertical overburden pressure, $P_a$is a reference pressure equal to 1 atm, and q_{c1Ncs} is the corrected cone tip resistance for the Idriss and Boulanger method.

Finally, with the calculated *CSR* and *CRR* values the liquefaction triggering model is applicable to wide ranges of CPT resistance values. The liquefaction triggering curve, for the Idriss and Boulanger deterministic model, is presented in Figure *3-18*. The *CRR* line for both Idriss and Boulanger studies (2008 and 2014) are shown.

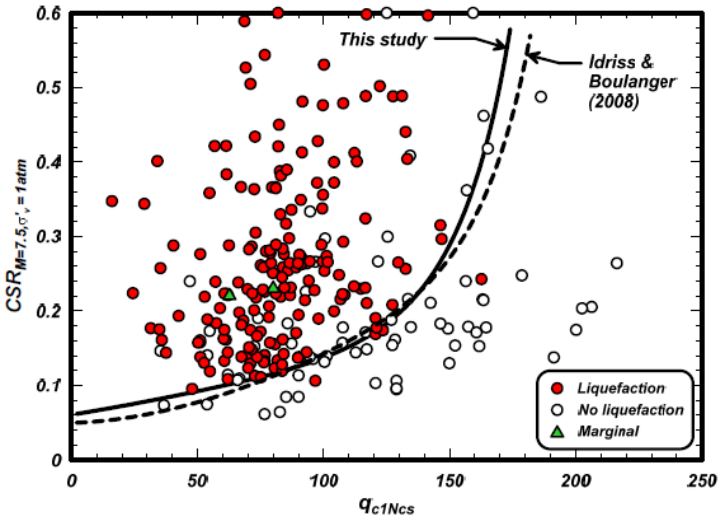

Figure 3-18: CRR curves and liquefaction curves for the deterministic case history database (after Idriss and Boulanger, 2014).

3.4.5 Probabilistic Boulanger and Idriss (2014) Procedure

Boulanger and Idriss (2014) also developed a probabilistic version of their liquefaction triggering procedure. Using their CPT case history database (Idriss and Boulanger 2008), Boulanger and Idriss developed an equation to calculate P_L. Rather than being a function of FS_L, like the Ku et al. P_L equation, this equation is a function of the seismic loading and soil stiffness and can be expressed as:

$$P_L = \Phi\left[-\frac{\left(\frac{q_{c1Ncs}}{113}\right)+\left(\frac{q_{c1Ncs}}{1000}\right)^2-\left(\frac{q_{c1Ncs}}{140}\right)^3+\left(\frac{q_{c1Ncs}}{137}\right)^4-2.60-\ln\left(CSR_{M=7.5,\sigma'_v=1atm}\right)}{\sigma_{\ln(R)}}\right] \quad (3\text{-}30)$$

where, Φ is the standard normal cumulative distribution function, q_{c1Ncs} is the clean sand corrected CPT resistance, $CSR_{M=7.5,\sigma'_v=1atm}$ is the corrected *CSR* value for a standardized magnitude and overburden pressure, and $\sigma_{\ln(R)}$ is the computed model uncertainty in the relationship. For their model, Idriss and Boulanger determined $\sigma_{\ln(R)}$ to be 0.2. It is important to note that the parameter uncertainties (uncertainty in $CSR_{M=7.5,\sigma'_v=1atm}$ and q_{c1Ncs}) are often larger than the model uncertainty, and therefore treatment of these uncertainties need to be addressed (Idriss and Boulanger, 2014).

Equation (3-17) can be used to develop liquefaction triggering curves, by calculating the P_L for a range of q_{c1Ncs} and $CSR_{M=7.5,\sigma'_v=1atm}$ values (Figure *3-19*). Idriss and Boulanger compared these curves with their deterministic triggering curve and found the deterministic triggering curve corresponds to P_L of 16% if $\sigma_{\ln(R)} = 0.2$.

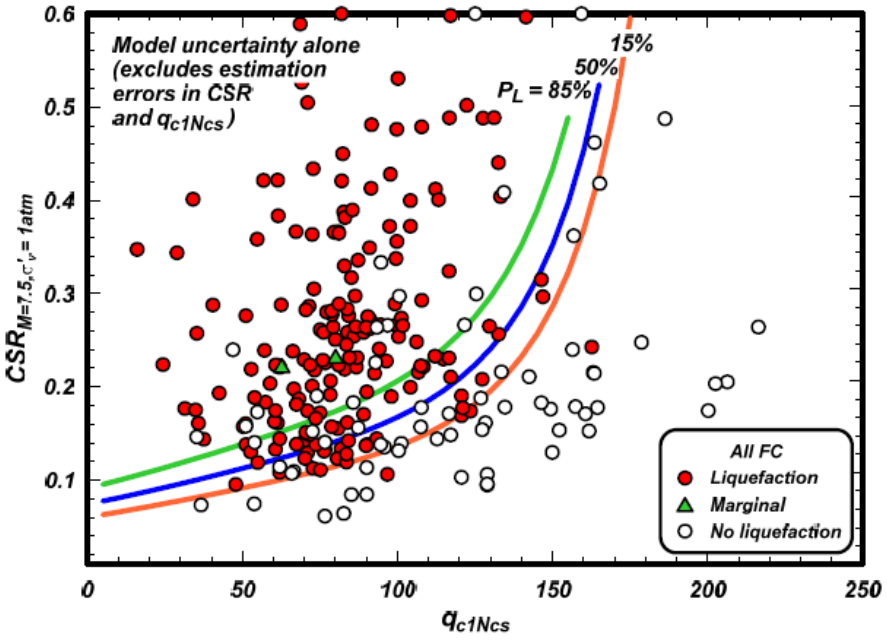

Figure 3-19: Liquefaction triggering P_L curves compared to case history data (after Idriss and Boulanger, 2014)

3.5 Liquefaction Effects

Liquefaction can affect almost all types of infrastructure including buildings, bridges, utilities, pipelines, roadways, and other constructed facilities through its effects. The effects of liquefaction cause extreme physical and financial damage after an earthquake. The purpose of this study is to improve prediction methods of liquefaction-induced effects. The most common and damaging effects are described in detail below.

3.5.1 Settlement

When liquefaction occurs in loose sands, the soil tends to densify, manifesting itself as settlement at the ground surface. When this settlement occurs unevenly, called differential settlement, more severe damage occurs. Differential settlement can sever pipelines, sever utilities, and cause damage to shallow foundation buildings. The target of this research is to

predict liquefaction-induced settlements; therefore, settlement is discussed in more detail in chapter 4.

3.5.2 Lateral Spread

Lateral spread is a liquefaction effect in which significant horizontal and vertical deformations accumulate during an earthquake. Lateral spread occurs when blocks of the soil are broken apart and essentially "float" on the liquefied soil down a slope (Figure *3-20*). The movement of these blocks can move from a few centimeters to several meters. Like settlement, lateral spread can sever pipelines and utilities and cause severe damage to foundations.

Figure 3-20: Lateral spreading from the 1989 Loma Prieta earthquake.

3.5.3 Loss of Bearing Capacity

Liquefaction causes a significant loss of bearing capacity because of a loss in shear strength during liquefaction. A loss in bearing capacity will cause severe damage to shallow footings and embankments, which will experience bearing capacity failure. Apartment buildings experienced this in the Niigata, Japan 1964 earthquake when they tipped over (Figure *3-21*).

Figure 3-21: Apartment buildings after the 1964 Niigata, Japan earthquake.

3.5.4 Alteration of Ground Motions

As a soil is seismically loaded, and liquefaction occurs, the stiffness of the soil decreases significantly. This decrease in stiffness can significantly alter ground motions, such as amplitude and frequency content. The high frequency ground motions are filtered out, resulting in only lower frequency ground motions reaching the surface. This phenomenon can result in large rolling displacements, which can cause extensive damage to buildings, especially those with low natural frequencies.

3.5.5 Increased Lateral Pressure on Walls

Liquefaction causes an increase of pore water pressure, which often pushes ground water towards the surface. Retaining walls with liquefied soils as their backfills will experience a large increase in static lateral pressures due to the hydrostatic force. Earthquake loading coupled with this increased lateral pressures is often enough to cause large deformations, or even failure.

3.5.6 Flow Failure

As discussed in section 3.4.2, flow liquefaction is one of the most serious and dangerous effects of liquefaction. Flow failures generally offer no warning because the loss of soil strength is sudden as the effective stress path reaches the FLS. For flow failures to occur, static shear stresses must already be present. Therefore, flow failures almost exclusively occur on sloping ground. At the initiation of flow failure, large soil masses flow as a fluid in the downslope direction. These flows can reach a velocity of several meters per second. All structures in the path of such flows can be completely destroyed, due to the sheer size and speed of these failures.

3.6 Chapter Summary

Liquefaction is a complex phenomenon that causes loose, saturated sands to lose all strength, and even flow as a fluid, under cyclic loading such as an earthquake. Liquefaction susceptibility depends on historical, geologic, compositional, and initial effective stress state criteria. Liquefaction will either occur as cyclic mobility or flow liquefaction, depending on the soil's initial effective stress state. This chapter presents the methods used to calculate the factor of safety against liquefaction (FS_L). Settlement, lateral spread, loss of bearing capacity, alteration of ground motions, increased pressures on walls, and flow failures are all common liquefaction-

induced effects. Each effect can cause severe damage to buildings, utility lines, and other important structures.

4 LIQUEFACTION-INDUCED SETTLEMENT

Settlement is one of the most damaging effects from an earthquake event. Settlement can occur uniformly or differentially, meaning unevenly across a site. Differential settlement is much more common and, unfortunately, is much more damaging. Differential settlement can cause buildings to tip over, severance of life or utility lines, and severe structural damage. Settlement can be life threatening, but generally in an indirect way (e.g. a building falling over, water supply cut off). However, even though settlement is not directly life-threatening, the financial toll of extreme liquefaction-induced settlements can be devastating to a city's economy. To prevent such extreme damage and design resilient structures, engineers need to fully understand how to accurately predict liquefaction-induced settlement to design adequate structures, foundations, and landlines.

4.1 Understanding Settlement

Whether or not a soil will settle is dependent on the soil's depositional environment. Very loose environments, such as Alluvial, Aeolian, and Colluvial deposits, are particularily susceptible to settlement. Very loose deposits have very large void spaces between each particle, which gives these deposits room to compact. Seismic loading can act as a compaction

mechanism by shaking the particles into a denser state creating large volumetric strains (Figure 4-1).

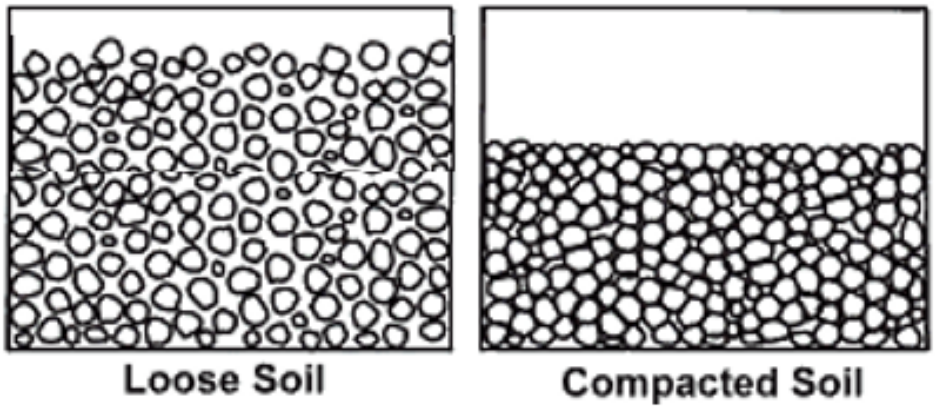

Figure 4-1: Volumetric change from settlement (after Nadgouda, 2007).

Differential settlement occurs because of varying thickness of liquefiable layers or liquefaction occurring unevenly across a site. Settlement is a function of the volumetric strain induced by a seismic event and the thickness of the liquefiable layer. When there are liquefiable soil layers, with varying thicknesses, across a site, each portion of the layer will result in varying amounts of surface settlement causing differential settlement.

When differential settlement is extreme, it can cause significant damage to surrounding infrastructure. Differential settlement can cause buildings to tip over or severely crack as half of the soil beneath a building's foundation settles, but the other half remains stable. Differential settlement is the main cause of the extreme damage and economic toll discussed previously. Figures 4-2 and 4-3 show examples of damage caused by differential settlement.

Figure 4-2: Buildings tipped over from differential settlement from the 2015 Kathmandu, Nepal earthquake (after Williams and Lopez, 2015).

Figure 4-3: Differential settlement splitting an apartment building (after Friedman, 2007).

It is important to understand that other mechanisms, such as soil-foundation-structure interaction (SFSI) and loss of soil due to piping, can affect the amount of soil deformations a site will experience (Bray & Dashti, 2014). A structure's weight and size can affect the amount settlement to occur at a specific site (Dashti & Bray, 2010). All post-liquefaction calculations and discussions for this study, therefore, only focus on free-field liquefaction-induced settlement. This study does not take into consideration SFSI or any piping effects from transient hydraulic gradients.

4.2 Calculating Settlement

There have been many settlement calculation methods created over the years, but three of the most recent and commonly used include Cetin et al. (2009), Ishihara and Yoshimine (1992), and Juang et al. (2013), which is a probabilistic extension of the Ishihara and Yoshimine method. The Cetin et al. method is a semiempirical method that is calibrated against 49 case histories of free-field liquefaction settlement and that uses the standard penetration test (SPT). Because this method is based on SPT data, it was not used for this study. This study focuses on the Ishihara and Yoshimine model, which is also a semiempirical method, but can be applied to CPT data.

4.2.1 Ishihara and Yoshimine (1992) Method

Ishihara and Yoshimine (1992) found that shear strain is a key parameter affecting post-liquefaction volumetric strain. This relationship was discovered by extensive testing of volumetric change characteristics of sand under undrained cyclic loading (Lee and Albaisa, 1974; Tatsuko et al., 1984; Nagase and Ishihara, 1988). Ishihara and Yoshimine (1992) produced a deterministic procedure to calculate post-liquefaction ground settlements based on volumetric strains in liquefiable soils, which is a function of FS_L. The database, used to create the basis for

the Ishihara and Yoshimine procedure, was developed by performing extensive simple shear tests on sand samples subjected to horizontal, undrained shear stresses with irregular time histories. These tests were performed at the University of Tokyo, the results of which were combined with the data provided by Nagase and Ishihara (1988). Ishihara and Yoshimine summarize their relationship using the curves presented in Figure *4-4*.

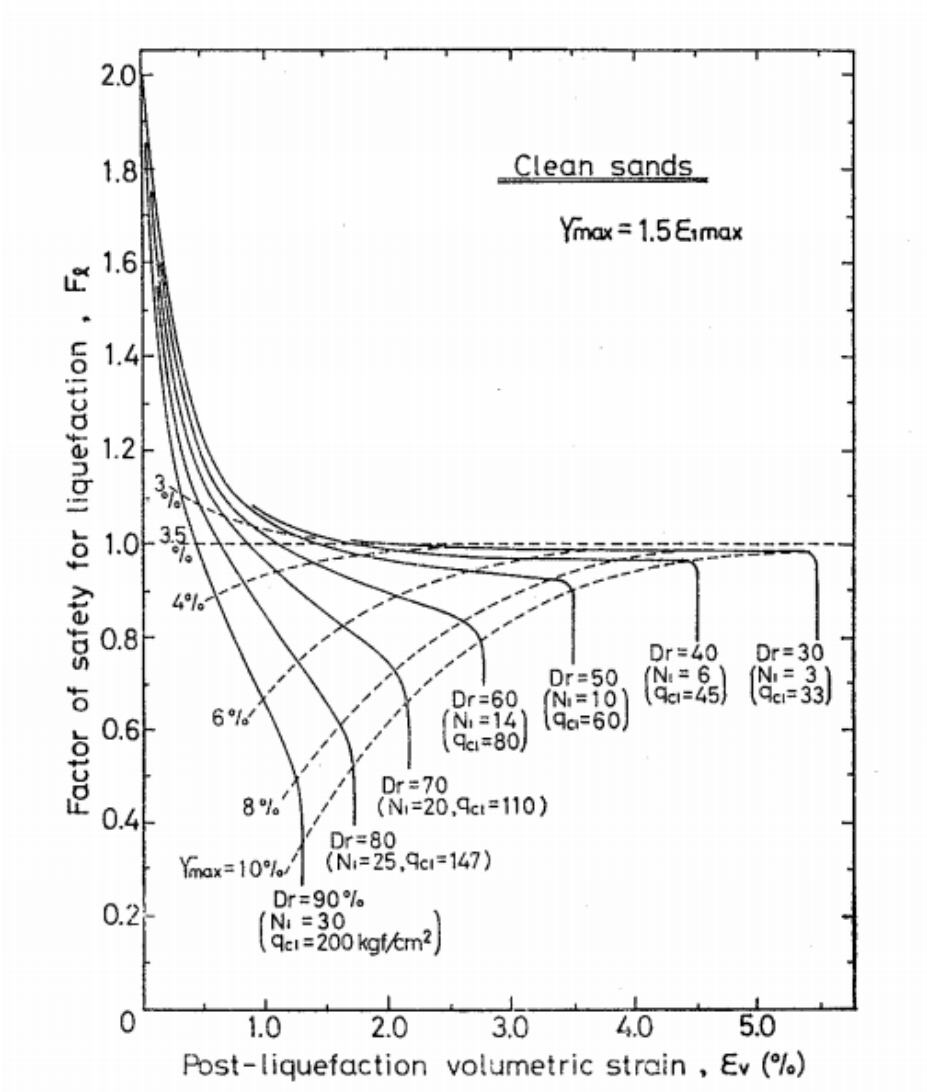

Figure 4-4: The relationship between FS_L, γ_{max}, and D_R (after Ishihara& Yoshimine, 1992).

Ishihara and Yoshimine (1992) used their method to estimate the liquefaction-induced settlements from the 1964 Niigata earthquake. The calculated values from their method compared well to actual settlements from the Niigata earthquake. It was shown that the proposed methodology may be used for predicting post-liquefaction settlements with a level of accuracy suitable for many engineering purposes.

The procedure for applying the Ishihara and Yoshimine (1992) method is given as follows: first, a factor of safety against liquefaction (FS_L) is obtained for each layer using a liquefaction triggering procedure (e.g., Robertson and Wride, 2009; Boulanger and Idris, 2014). A relative density is also calculated for each layer, using Tatsuka et al. (1990):

$$D_R = -85 + 76log\frac{q_c}{\sqrt{\sigma'_v}} \tag{4-1}$$

where q_c is the cone tip resistance and σ'_v is the vertical effective stress. Using FS_L and calculated D_R for each layer, volumetric strain can be obtained from the Ishihara and Yoshimine strain curves (Figure 4-4). Each layer's volumetric strain is multiplied by the layer's thickness, resulting in the vertical liquefaction-induced settlement (S_p) of each layer. Finally, each layer's settlement is summed together to calculate the predicted total ground surface settlement, using the following equation:

$$S_p = \sum_{i=1}^{N} \varepsilon_v \Delta Z_i \tag{4-2}$$

where ε_v is volumetric strain for the i^{th} layer, N is number of layers, and ΔZ_i is the i^{th} layer's thickness.

4.2.2 Juang et al. (2013) Procedure

The Juang et al. (2013) procedure calculates liquefaction-induced settlements by applying a probabilistic approach to the deterministic Ishihara and Yoshimine (1992) method, for the cone penetration test (CPT). Prior to the Juang et al. procedure, existing CPT-based models often overestimated liquefaction-induced settlements. Juang et al. managed to compile a database of free-field settlement case histories from recent earthquakes and used it to calibrate the Ishihara and Yoshimine (1992) model for bias using the CPT. Using this bias-corrected model, a simplified procedure was developed that allowed for the estimation of the probability of exceeding a specified settlement at a given site.

The Juang et al. (2013) procedure also uses Equation (4-2) to calculate predicted vertical settlements but adds probabilistic parameters by using the following equation:

$$S_p = M \sum_{i=1}^{N} \varepsilon_v \Delta Z_i IND_i \tag{4-3}$$

where ε_v is volumetric strain for the i^{th} layer, N is the number of layers, M represents a modal bias correction factor equal to 1.0451, IND_i represents the probability of liquefaction occurring, and ΔZ_i is layer thickness for the i^{th} layer. ε_v is calculated by using a curve-fitted equation, by Juang et al., based on the Ishihara and Yoshimine (1992) curves (Figure *4-4*), given as:

$$\varepsilon_v\,(\%) = \begin{cases} 0 & if\ FS \geq 2 \\ \min\left\{ \dfrac{a_o + a_1 \ln(q)}{{}^{1}/_{(2\ -\ FS)}\ -\ [a_2 + a_3 \ln(q)]},\ b_0 + b_1 \ln(q) + b_2 \ln(q)^2 \right\} & if\ 2 - \dfrac{1}{a_2 + a_3 \ln(q)} < FS < 2 \\ b_0 + b_1 \ln(q) + b_2 \ln(q)^2 & if\ FS \leq 2 - \dfrac{1}{a_2 + a_3 \ln(q)} \end{cases} \tag{4-4}$$

Where: $a_o = 0.3773$, $a_1 = -0.0337$, $a_2 = 1.5672$, $a_3 = -0.1833$, $b_o = 28.45$, $b_1 = -9.3372$, $b_2 = 0.7975$, $q = q_{t1Ncs}$

The model bias correction factor, *M*, was calculated by Juang et al. (2013) calibrating their model back to the case histories' data through Bayesian maximum likelihood methods. Juang et al. presents the IND_i variable as probability of liquefaction (P_L), which they calculate as:

$$IND_i = P_L = 1 - \phi\left\{\frac{0.102 + \ln(FS_L)}{\sigma_{\ln(s)}}\right\} \quad (4\text{-}5)$$

where $\sigma_{\ln(s)}$ represents the model uncertainty and is equal to 0.276.

One significant disadvantage associated with the Juang et al. (2013) probabilistic model for CPT-based settlement prediction is that the model was based on the binomial assumption that liquefaction settlements can be caused by both liquefied and non-liquefied soils. Engineers commonly consider a soil layer susceptible to post-liquefaction settlement if the soil layer has a sufficiently low factor of safety against liquefaction (usually less than 1.2 to 2.0). Engineers rarely (if ever) consider non-liquefied soils to contribute to liquefaction settlements. However, the Juang et al. (2013) model includes the probability that non-liquefied soil layers contribute to the settlement, which may make sense mathematically, but not physically. While the possibility of non-liquefied soil layers contributing to post-liquefaction settlements is likely greater than zero, it is also likely sufficiently low that most engineers choose to neglect it. Furthermore, the consideration of this possibility greatly increases the mathematical difficulty of the Juang et al. model. Therefore, this study re-solved the maximum likelihood equation developed by Juang et al. (2013), but neglected the possibility that non-liquefied layers contribute to liquefaction so as to neglect the possible settlements. The resulting values of *M* and $\sigma_{\ln(s)}$ are 1.014 and 0.3313, respectively. Any potential error introduced by this simplification is accounted for in the larger value of $\sigma_{\ln(s)}$. Therefore, these re-regressed values of *M* and $\sigma_{\ln(s)}$ are used in this study.

These re-regressed values were calculated by altering the Juang et al. (2013) maximum likelihood equation. The original Juang et al. (2013) maximum likelihood equation for the database with $m + n$ case histories, where m is the number of cases with a fixed settlement observation and n is the number of case histories in which settlement is reported as a range, is given as:

$$\begin{aligned}\ln\{L[\theta|S_a(1),S_a(2),\dots,S_a(m),S_{a,low}(1),S_{a,up}(1),\dots,S_{a,low}(n),S_{a,up}(n)]\}\\ =\sum_{k=1}^{m}\left\{-\ln[\sqrt{2\pi}\xi(k)S_a(k)]-\frac{1}{2}\left(\frac{\ln[S_a(k)]-\lambda(k)}{\xi(k)}\right)^2\right\}\\ +\sum_{l=1}^{n}\ln\left[\Phi\left(\frac{ln[S_{a,up}(l)]-\lambda(l)}{\xi(l)}\right)\right.\\ \left.-\Phi\left(\frac{ln[S_{a,low}(l)]-\lambda(l)}{\xi(l)}\right)\right]\end{aligned} \tag{4-6}$$

where S_a is the actual settlement observed, k represents the kth case history from the database with m case histories, and l is the lth case history from the database with n case histories. For the re-derivation, only the case histories containing actual recorded settlements were used. The case histories with ranges of settlement (n case histories) were removed. In Equation (4-6), the λ and ξ variables were represented as:

$$\lambda(k)=\ln\left\{\frac{\mu_a(k)}{\left[1+{\delta_a}^2(k)\right]^{0.5}}\right\} \tag{4-7}$$

and

$$\xi(k)=\ln\left\{\left[1+{\delta_a}^2(k)\right]^{0.5}\right\} \tag{4-8}$$

where $\mu_a(k)$ represents the mean of actual observed settlement for the kth case history and δ_a represents the coefficient of variation (COV) of S_a. This δ_a is given as:

$$\delta_a = \frac{(\mu_M{}^2\sigma_p{}^2 + \mu_p{}^2\sigma_M{}^2 + \sigma_M{}^2\sigma_p{}^2)^{0.5}}{\mu_M{}^2\mu_p{}^2} = (\delta_p{}^2 + \delta_M{}^2 + \delta_p{}^2\delta_M{}^2)^{0.5} \quad (4\text{-}9)$$

where μ_M is the mean of M, σ_M is the standard deviation of M, μ_p is the mean of the predicted settlement, and σ_p is the standard deviation of the predicted settlement. For the re-regression, all of the variables with a "p" term were removed to remove the assumption of non-liquefied layers adding to settlement hazard. The δ_a term was simplified to:

$$\delta_a = \frac{\sigma_M}{\mu_M} = \delta_M \quad (4\text{-}10)$$

This simplified δ_a replaced equation (4-9). The new M and $\sigma_{\ln(s)}$ values were calculated by using Juang et al. (2013) maximum likelihood equation (Equation 4-6), but by replacing Equation (4-9) with Equation (4-10) and only using the m case histories.

4.3 Settlement Calculation Corrections

When dealing with all levels of probability, some unrealistic, incorrect, or impossible strain values can be computed. Various correction methods have been developed to address and correct unrealistic strain values that can be computed using simplified, semi-empirical strain models. The corrections used in this study are described below.

4.3.1 Huang (2008) Correction for Unrealistic Vertical Strains

Huang (2008) developed a method to limit unrealistically high vertical strain values computed in probabilistic calculations. Kramer et al. (2008) explained that direct computation of probabilistic vertical strains has been found to produce significant unrealistically high

probabilities of very large strain values. Kramer et al. (2008) explains these unrealistically high strain estimations are due to the assumption of lognormal probability distributions typically associated with the calculation of vertical strains. For low soil stiffness values, the slope of the lognormal probability density function increases infinitely, appropriately allowing large probabilities to be associated with large strains. Denser soils, however, can still predict large probabilities of vertical strain, even though both laboratory and field observations have shown that large vertical strains with such soils are very unlikely.

Huang (2008) performed a study to find the maximum limited strain for different types of soil. Huang evaluated theoretical, historical (i.e., field), and laboratory evidence of a maximum vertical strain experienced by a given soil layer. He relied heavily on the apparent limiting strain observed by four previous studies: Tokimatsu and Seed (1987), Ishihara and Yoshimine (1992), Shamoto et al.(1998), and Wu and Seed (2004), to develop estimates of the maximum or limiting

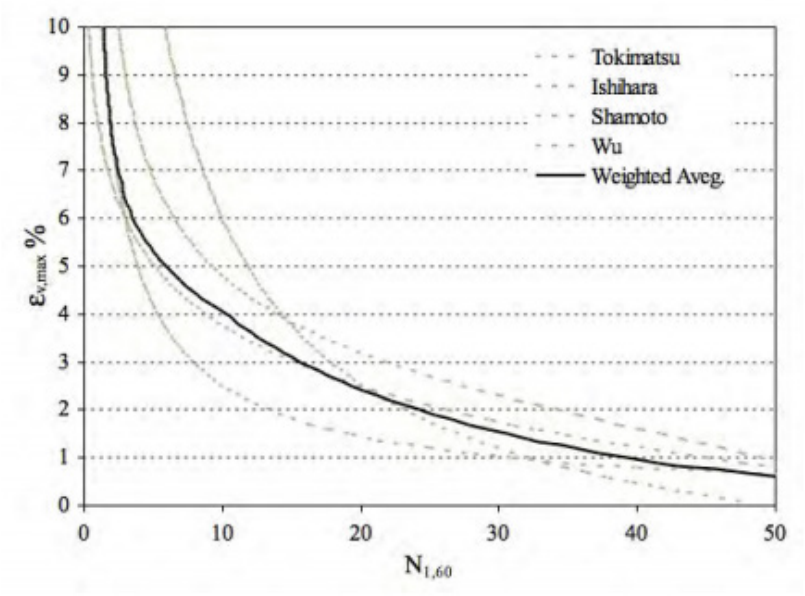

Figure 4-5: Maximum vertical strain levels inferred by deterministic vertical strain models and weighted average used to define mean value (after Huang, 2008).

vertical strain as a function of SPT blow counts. The Huang (2008) and Kramer et al. (2008) maximum vertical strain curves are shown in Figure *4-5*.

Kramer et al. (2014) approximated the weighted average relationship of the Huang (2008) and Kramer et al. (2008) maximum vertical strain curves as:

$$\varepsilon_{v,max}(\%) = 9.765 - 2.427ln[\,(N_1)_{60,cs}] \tag{4-11}$$

where $(N_1)_{60,cs}$ is the normalized, clean sand-equivalent SPT resistance. Because there is scatter in the maximum vertical strain curves based on the different studies that were evaluated, Huang (2008) suggests using an $\varepsilon_{v,max}$ range of 0.5*$\varepsilon_{v,max}$ to 1.5*$\varepsilon_{v,max}$ to account for uncertainty in the true value of $\varepsilon_{v,max}$. To make Equation (4-6) compatible with CPT data for this study, Jefferies and Davies (1993) is used to convert between CPT tip resistance and SPT resistance. This relationship is presented as:

$$\frac{(q_t/p_a)}{(N_1)_{60,cs}} = 8.5(1 - \frac{I_c}{4.6}) \tag{4-12}$$

where *Pa* is atmospheric pressure, I_c is the Soil Behavior Type Index, and q_t is the normalized tip resistance. Using Equation (4-12), Equation (4-11) can be used for the CPT and rewritten as:

$$\varepsilon_{v,max}(\%) = 9.765 - 2.427ln\left[\frac{\left(\frac{q_t}{p_a}\right)}{8.5\left(1 - \frac{I_c}{4.6}\right)}\right] \tag{4-13}$$

4.3.2 Depth Weighting Factor Correction

Calculated deformations at great depth have little influence on ground surface displacements (Iwasaki et al., 1982). A depth weighting factor (DF) recommended by Cetin et al. (2009) and Dr. Peter Robertson (personal communications) is incorporated to account and correct for this phenomenon to reduce the influence of calculated strains at depth. This depth factor aids in producing a better fit between models and case studies and is based on the following: (1) the triggering of void ratio redistribution, and resulting in unfavorably higher void ratios for shallower layers from upward seepage; (2) reduced induced shear stresses and number of shear stress cycles transmitted to deeper soil layers due to initial liquefaction of surficial layers; and (3) possible bridging effects due to nonliquefied soil layers (Cetin et al., 2009). This depth weighting correction factor developed by Cetin et al. (2009) is given as:

$$DF_i = 1 - \frac{d_i}{18m} \tag{4-14}$$

where d_i is the depth of the specific soil layer. At depths greater than 18m, the depth factor is zero which indicates liquefaction past these depths will not contribute to ground surface settlement. This depth factor is applied by multiplying the calculated strain for each layer by this factor.

4.3.3 Transition Zone Correction

The CPT is known for its ability to provide a continuous soil profile. However, the measured q_c value does not sharply change as the cone reaches the inter-layer boundary between one soil layer to another. Experimental studies have shown that the measured cone tip resistance is affected by the material properties of soil layers both ahead and behind the penetrating cone

(Treadwell, 1976). Thus, the cone will start to detect the soil layers below the cone tip before it reaches them and will continue to sense overlaying material after it has penetrated the new material. For example, the tip resistance, in a stiff layer, may start to decrease rapidly as it approaches a softer layer below (Figure 4-6). Therefore, the CPT tip resistance may not always measure the correct tip resistance in the transition zone between soil layers of significantly different penetration resistances. A transition zone is identified if there is a steep change in the soil behavior index (I_c), usually a change of 0.01 or greater, for multiple soil sublayer increments (Robertson, 2011). To account for this Robertson (2011) suggests removing these sublayers from the analysis. However, these sublayers could still potentially add to the liquefaction hazard. Therefore, for this study, transition zones are addressed by correcting the tip resistance values using the same process as thin layer correction, which is discussed in the next section.

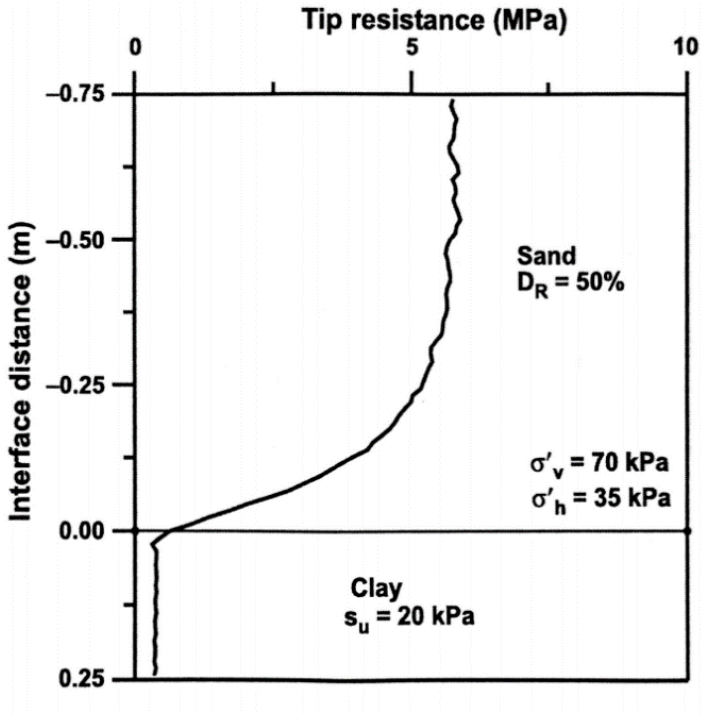

Figure 4-6: Penetration analysis for medium dense sand overlaying soft clay (after Ahmadi and Robertson 2005)

4.3.4 Thin Layer Correction

When a thin sand layer is embedded within a soft clay, the cone from the CPT will read the sand layer's cone tip resistance as much lower than the actual stiffness of the thin layer because it has started to detect the soft clay layer's resistance early (Ahmadi & Robertson, 2005). This discrepancy results in an over-prediction of post-liquefaction settlements because the cone is interpreting the sandy soil as looser than it really is. Youd et al. (2001) presents a correction factor to correct the cone tip resistance in these thin sand layers. As shown in figure 4-7, as the cone enters deposit A (thin sand layer), the soil resistance is significantly reduced before the cone reaches deposit B (soft clay layer). This phenomenon occurs because the cone is detecting the softness of deposit B before it reaches deposit B. The higher the stiffness and thinner the layer of sand interbedded within soft clay, the larger the thin layer correction factor should be.

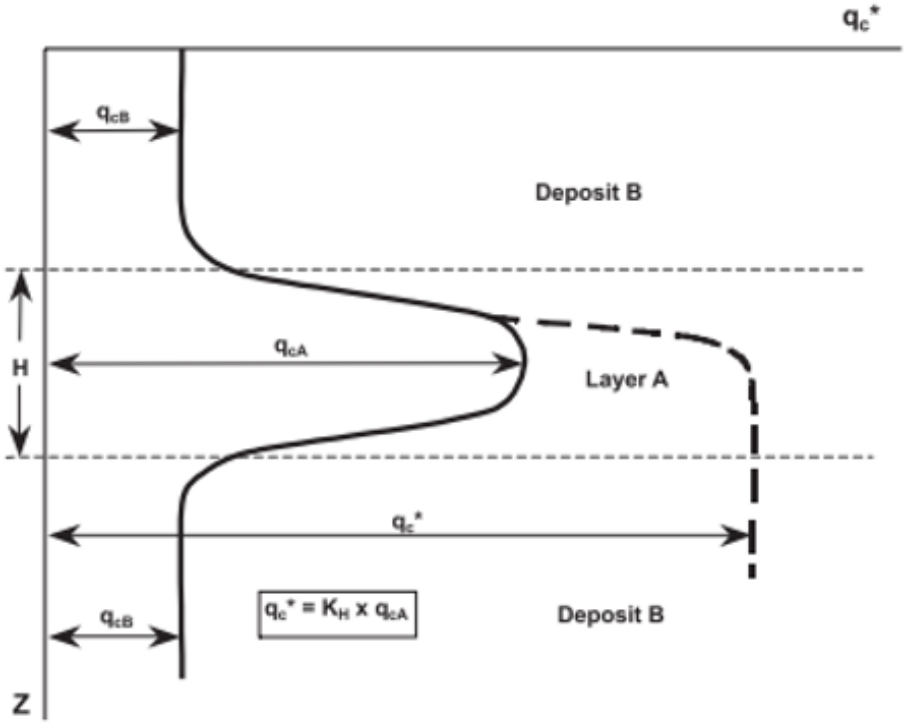

Figure 4-7: Tip resistance analysis for thin sand layer (deposit A) interbedded within soft clay layer (deposit B). (Ahmadi & Robertson, 2005).

Once a layer has been identified as needing the thin layer correction, the tip resistance can be adjusted with a correction factor. A layer is identified as a thin layer if there is a steep negative change (e.g., going from a sand layer to a clay layer) in the soil behavior index (I_c), usually a change of 0.01 or greater, for four consecutive soil sublayer increments (Robertson, 2011). Once identified, these layer's tip resistances can be corrected as:

$$q_c{}^* = K_H q_c \tag{4-15}$$

where $q_c{}^*$ is the corrected cone tip resistance and K_H is the correction factor (Youd et al., 2001). This factor is calculated as:

$$K_H = 0.25\left[\frac{\left(\frac{H}{d_c}\right)}{17} - 1.77\right]^2 + 1.0 \tag{4-16}$$

where d_c is the diameter of the cone, and H is the layer thickness.

4.4 Chapter Summary

Liquefaction-induced settlements pose a serious threat to infrastructure and to the people who rely on it. While liquefaction-induced settlements are not directly life-threatening, differential settlement can cause severe damage to structures, utility lines, and life lines, resulting in a large economic toll on a community. The ability for engineers to predict liquefaction-induced settlements is crucial to mitigate and prevent severe damage in the event of an earthquake. This chapter presented a deterministic and probabilistic method to predict liquefaction-induced settlements. Finally, this chapter addressed settlement correction factors to account for unrealistic settlement estimations.

5 GROUND MOTION SELECTION FOR LIQUEFACTION ANALYSIS

In seismic regions around the world, earthquakes pose enough of a hazard to promote careful analysis and design of structures and facilities. Earthquake design involves designing a structure to withstand a certain level of earthquake shaking or hazard. Specifying the design level of an earthquake to resist is a difficult part of geotechnical earthquake engineering. Choosing a design earthquake is difficult because there are high levels of uncertainty to deal with in determining the location, magnitude, and ground motions of an earthquake.

To account for this difficulty, many engineers will design for what they perceive to be the "worst case" scenario earthquake in their region. This approach, referred to as a deterministic seismic hazard analysis (DSHA), does not take into account the likelihood of the controlling event occurring and neglects the seismic hazard contribution of all other seismic sources near the fault. To try to improve on the accuracy of the DSHA, more seismic hazard analysis (SHA) methods have been created and applied to predicting post-liquefaction settlements. Each of these SHA approaches differ in how ground motions are selected and applied. This chapter discusses each of these approaches and presents the newly developed performance-based procedure to predict post-liquefaction settlements for the CPT. It is not generally fully understood how differing seismic hazard analyses add bias into the seismic hazard predictions. To address this

misunderstanding, this study was designed to compare conventional design methods to the new, fully-probabilistic, design procedures. This comparative study and presented in Chapter 6.

5.1 Seismic Hazard Analysis

SHA involves the process of predicting strong ground motions for a given site, in a quantitative fashion. There are two basic types of SHA, namely a DSHA and a probabilistic seismic hazard analysis (PSHA). DSHA conservatively assumes an earthquake scenario, usually ground motions from the most impactful fault near the site, and performs design calculations based on the ground motion parameters from that single earthquake scenario. PSHA explicitly takes into account the uncertainties in earthquake size, location, and time of occurrence to select design ground motion parameters. Both methods are discussed in more detail below.

5.1.1 Deterministic Seismic Hazard Analysis

In the early years of geotechnical earthquake engineering, engineers generally used the DSHA for earthquake design. DSHA involves selecting a particular seismic scenario to design from (Steven L Kramer, 1996). Design ground motion parameters are selected based off of this particular scenario. DSHA considers the fault capable of producing the largest ground motion at the site. This assumption can result in inconsistent results.

Reiter (1990) organizes the DSHA into four general steps (Figure *5-1*). The first step is to identify and characterize all possible seismic sources capable of producing significant ground motions at the site of interest. Characterizing the sources includes determining each source's geometry and level of seismicity. The second step is to determine the closest site-to-source distances for each source. These distances could be epicentral or hypocentral distances. Determining the controlling earthquake is the third step, which involves determining which

earthquake source will create the largest ground motions by comparing the levels of shaking found in step one at distances found in step two. The final, and fourth, step formally defines the seismic hazard at the site based on the controlling earthquake. Hazards are often defined in multiple parameters, such as the ones discussed in chapter two.

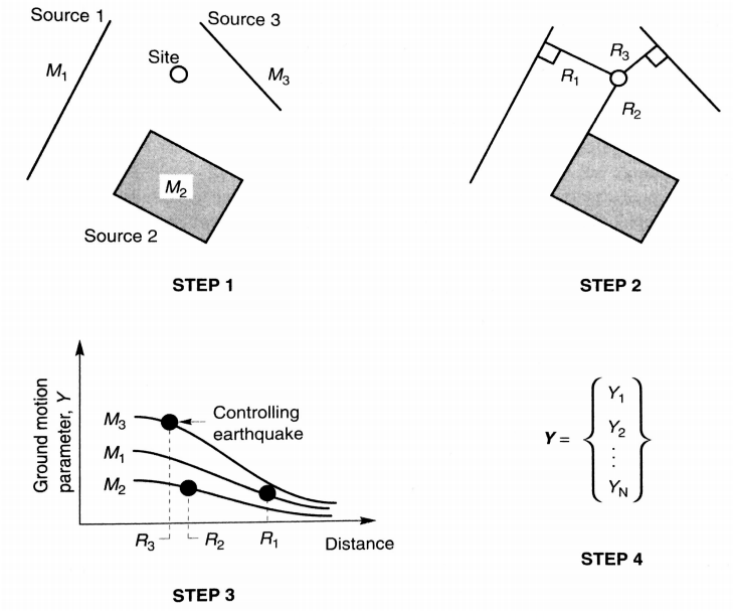

Figure 5-1: Four steps of a DSHA (Kramer, 1996).

5.1.2 Probabilistic Seismic Hazard Analysis

As geotechnical earthquake engineering has progressed, engineers have developed the probabilistic seismic hazard analysis (PSHA) method. PSHA takes into account all of the uncertainties relating to the size, location, and rate of occurrence of a seismic event. The PSHA framework in which each uncertainty can be identified, quantified, and combined to provide a clear level of site seismicity (Algermissen, 1982; Cornell, 1968).

Just as the DSHA, the PSHA can be broken into four distinct steps (Steven L Kramer, 1996; Reiter, 1990). The first step (Figure *5-2*) of the PSHA is to identify and characterize all potential earthquake sources. This step is the same for the DSHA, except the PSHA also identifies the distribution of the probability of rupture along the source. However, in most cases a uniform probability distribution is used to indicate that all points along the fault are equally likely to rupture. The second step takes into account the probability of the recurrence of a specific level of earthquake. This utilizes recurrence relationships, which indicate average rates of exceedance of a specific level of earthquake. Engineers will decide which return period, or exceedance rate, is appropriate for the design of their structure. The next step is to determine the ground motions, using attenuation relationships, at the site created by earthquakes of a given size at a given location. The fourth, and final, step combines all of the inherent uncertainties, of potential earthquake sizes, locations, and ground motions, to calculate the probability the ground motion parameter will be exceeded during a seismic event.

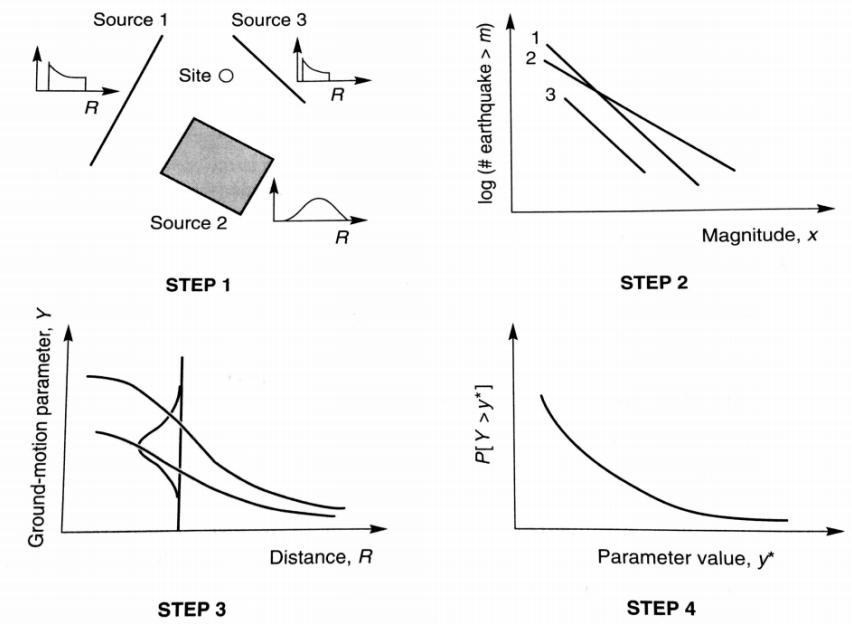

Figure 5-2: Four steps of a PSHA (Kramer, 1996).

The result of a DSHA is usually a singular value, such as a factor of safety, but because a PSHA takes into account all possible seismic events it produces a range of results, each value associated with a different likelihood. PSHA results are generally expressed in terms of the annual rate of exceedance (λ), which is the probability a specific event will be exceeded in any given year. All of the annual rate of exceedances are generally combined and displayed as a seismic hazard curve. Hazard curves are discussed in detail in the next section.

5.1.2.1 Seismic Hazard Curves

Seismic hazard curves represent the probability of exceeding a particular ground motion at a site. These curves can be obtained for individual seismic sources or combined to represent the comprehensive hazard of all surrounding sources (Kramer, 1996). Hazard curves are created by calculating the probability of exceeding a particular value (y^*) of a particular ground motion (Y) for one possible earthquake at one possible location. This probability is then multiplied by the probability that that particular earthquake will occur at a particular location. This calculation is repeated for all possible magnitudes and locations. These probabilities are summed together to calculate the total probability of exceeding (λ) the given ground motion parameter, y^*. This process is then repeated for a whole range of the ground motion parameter until it creates a complete hazard curve. The inverse of the probability of exceedance is the return period (T_R), which describes the average number of years between exceedance occurrences.

The probability that a specified ground motion will be exceeded may be calculated using the magnitude and source-to-site distance of all possible earthquakes that could affect the site. The probability of exceedance can be computed as:

$$P[\,Y > y^*] = \iint P[Y > y^* | m, r]\, f_M(m) f_R(r)\, dm\, dr \tag{5-1}$$

where $P[\,Y > y^*]$ is calculated from the selected attenuation relationship(s) and $f_M(m)$ and $f_R(r)$ are probability density functions for magnitude and source-to-site distance, respectively (Kramer, 1996). If the site is in a region of multiple seismic sources, the annual rate of exceedance can be calculated as:

$$\lambda_{y^*} = \sum_{i=1}^{N_s} v_i \iint P[Y > y^* | m, r]\, f_M(m) f_R(r)\, dm\, dr \tag{5-2}$$

where N_s represents all of the various seismic sources and v_i represents average rate of threshold magnitude exceedance, which can be computed as:

$$v_i = e^{\alpha_i - \beta_i m_0} \tag{5-3}$$

where $\alpha = 2.303a$ and $\beta = 2.303b$, and a and b are Gutenberg-Richter recurrence law coefficients. The threshold magnitude is the magnitude that must be exceeded for significant damage to be caused. The average rate of threshold magnitude exceedance limits the sources to a specific range of magnitude. This limit is used because earthquakes below a magnitude of 4.0 or 5.0 will cause very little severe damage. These smaller earthquakes are generally ignored in a hazard analysis.

Equation (5-2) is too complicated for the integrals to be evaluated with closed-form solutions, so numerical integration is required to be used. Numerical integration can be performed in a variety of ways; one approach is to divide all the possible ranges of magnitude and distance into equal segments of N_M and N_R, respectively. An estimation of the average rate of exceedance may be calculated by:

$$\lambda_{y^*} = \sum_{i=1}^{N_S} \sum_{j=1}^{N_M} \sum_{k=1}^{N_R} v_i \, P\left[Y > y^* \middle| m_j, r_k\right] f_{Mi}(m_i) f_{Ri}(r_k) \, \Delta m \, \Delta r \tag{5-4}$$

where $m_i = m_o + (j - 0.5)(m_{max} - m_o)/N_M$, $r_k = m_{min} + (k - 0.5)(r_{max} - r_o)/N_R$, $\Delta m = (m_{max} - m_o)/N_M$, and $\Delta r = (r_{max} - r_o)/N_R$. Equation (5-4) assumes that each source is only capable of generating only N_M different earthquakes at only N_R different source-to-site distances (Kramer, 1996). By using this assumption, an estimation of Equation (5-4) can be written as:

$$\lambda_{y^*} \approx \sum_{i=1}^{N_S} \sum_{j=1}^{N_M} \sum_{k=1}^{N_R} v_i \, P\left[Y > y^* \middle| m_j, r_k\right] P[M = m_j] P[R = r_k] \tag{5-5}$$

The accuracy of this numerical integration approach increases as the number of intervals of N_M and N_R increase. It should be mentioned that using a more refined method of numerical integration would produce more accurate results. Equation (5-5) produces only one point on a hazard curve. To generate the whole curve the process is repeated for a whole range of ground motion parameters (y^*).

5.2 Incorporation of Ground Motions in the Prediction of Post-Liquefaction Settlement

Accurate selection of design ground motions is crucial to accurate liquefaction hazard estimations. A structure will only be able to withstand earthquake shaking, and its effects, up to the ground motions it was designed for. Therefore, to be able to accurately design for liquefaction-induced settlements the correct level of ground motions need to be accounted for in the hazard analysis. However, selecting correct ground motions can be difficult due to the inherent uncertainty within predicting earthquake events. The most common approaches, for incorporating ground motions into post-liquefaction settlement estimations, are addressed in this study and discussed in this section.

The selection of ground motions is not directly incorporated into post-liquefaction settlement estimations, but rather into the liquefaction triggering analysis. Therefore, this section will also address how liquefaction triggering is computed for each approach and how it is incorporated into post-liquefaction settlement estimations.

To present each of these approaches more clearly, an example calculation is performed for each approach. This example calculation is performed for CPT profile at a site located in Salt Lake City, Utah at a Latitude and longitude of 40.76, -111.89 degrees, respectively. The CPT profile of interest is chosen due to its highly-liquefiable nature. The $Q_{tn,cs}$ across depth, for this profile, is plotted in Figure *5-3*. To simplify the example, settlement values are computed and compared for the 2475 return period and only the Robertson and Wride (2009) triggering procedure.

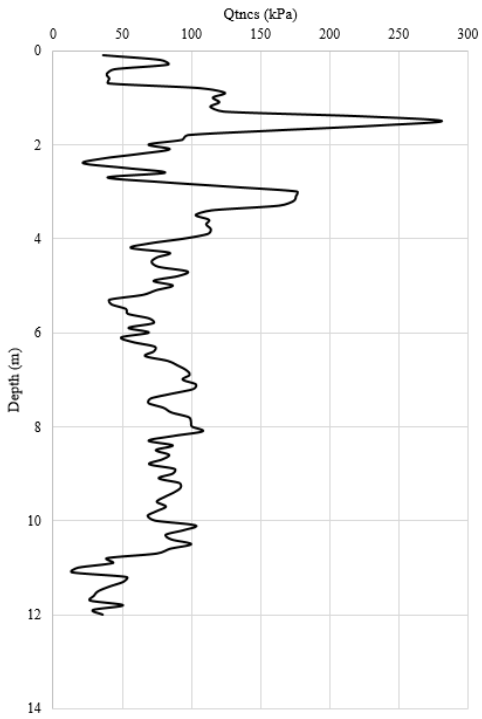

Figure 5-3: CPT profile used for example calculations.

5.2.1 Deterministic Approach

As discussed in section 5.1.1, a deterministic seismic hazard analysis involves designing for the largest and most significant ground motions at the site. The ground motions (i.e., a_{max}) and corresponding moment magnitude, M_w, from this design earthquake are used to calculate a FS_L and $Q_{tn,cs}$ using the liquefaction triggering procedures discussed in sections 3.5.2 and 3.5.4, specifically Equations (3-1) through (3-29). This FS_L is calculated for each soil sublayer in the CPT profile. This calculated FS_L, and the corresponding $Q_{tn,cs}$, is used with the Ishihara and Yoshimine (1992) deterministic strain relationship given in Equations (4-1) through (4-4). Strain values are calculated for each soil layer, multiplied by the layer thickness, and finally summed together to calculate the total ground settlement.

For the Salt Lake City, UT example, the controlling fault is the Wasatch fault because it is the closest and would have the greatest impact to Salt Lake City. The Wasatch fault has the potential to produce a 7.0 magnitude earthquake. The NGA west-2 database (Ancheta et al., 2014) is used to calculate a_{max} (0.456g) at this location for the controlling fault. These values are used to calculate $Q_{tn,cs}$ and FS_L using the Robertson and Wride (2009) triggering procedure for each layer [Equations (3-1) through (3-14)]. These values are then used to calculate settlement using the Ishihara and Yoshimine (1992) procedure. The deterministic calculated settlement, for this example, is 34.4cm.

5.2.2 Pseudo-Probabilistic Approach

The pseudo-probabilistic approach involves selecting design ground motions through probabilistic methods and applying them to a deterministic calculation of earthquake effects. This procedure involves using a deterministic triggering procedure (sections 3.5.2 and 3.5.4) to

calculate FS_L, but by using a PSHA to select input ground motions. This PSHA selection of ground motions is usually performed by using the USGS deaggregation tool (https://earthquake.usgs.gov/hazards/interactive/). This magnitude can be either the mean (i.e., average) or modal (i.e., occurring the most often) magnitude for the specific location. The FS_L and $Q_{tn,cs,}$ from the triggering procedures, values are then applied to the deterministic Ishihara and Yoshimine (1992) procedure to calculate post-liquefaction settlements. Even though the pseudo-probabilistic approach accounts for some uncertainty in ground motions, inherent uncertainty within the triggering of liquefaction and the calculation of its effects are generally ignored. Furthermore, the approach assumes that all liquefaction hazard is caused by a single return period of ground motions. Therefore, a common misperception of the pseudo-probabilistic approach is that the return period of the computed post-liquefaction settlements is the same as the return period of the input ground motions. This perception would only be true if there was no uncertainty associated with the computation of settlements.

A pseudo-probabilistic settlement analysis is performed for the Salt Lake City, UT example. From the USGS deaggregation tool as a return period of 2,475 years, the mean magnitude and PGA are 7.53 and 1.325g, respectively. The modal magnitude is 7.10. For simplicity in this example, a_{max} is assumed to equal PGA. These deaggreagation values were used with the Robertson and Wride (2009) triggering procedure, by using Equations (3-1) through (3-14). The calculated settlements using mean and modal magnitudes are 34.9cm and 34.8cm, respectively. Because the mean and modal magnitudes are so similar, they produce similar settlement estimations, in this case, but often produce very different settlements.

5.2.3 Performance-Based Approach

In an effort to promote advancement in the current building codes and to provide a fully-probabilistic seismic analysis, a new seismic hazard design approach has been developed, known as performance-based earthquake engineering (PBEE). This approach was developed by the Pacific Earthquake Engineering Research (PEER) Center (C. A. Cornell & Krawinkler, 2000; Deierlein, Krawinkler, & Cornell, 2003). The PEER framework was designed to address all earthquake risks.

The PEER framework seeks to improve seismic risk decision-making through assessment and design methods that are more transparent, scientific, and informative to stakeholders than current prescriptive approaches (Deierlein et al., 2003). Conventional design methods usually only present the earthquake risk in terms of a factor of safety, which can be hard for various stakeholders to truly understand. This misunderstanding is because each stakeholder thinks about risk differently. For example, structural engineers think of structural collapse or deformation, owners think about cost or downtime, and government agencies think about fatalities. When engineers, owners, and governing agencies are only presented with a factor of safety, it can be difficult for them to make a truly informed decision. PBEE improves this decision-making by presenting earthquake risks in metrics that matter to each stakeholder. Figure *5-4* illustrates the various levels of performance across multiple metrics, important to different stakeholders.

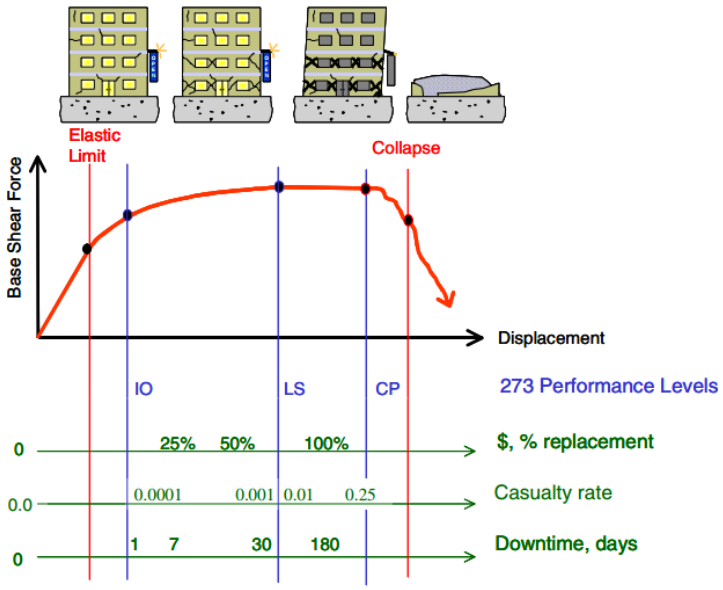

Figure 5-4: Visualization of performance-based earthquake engineering (after Moehle and Deierlein, 2004).

The objective of PBEE is to quantify all of the inherent uncertainty in predicting seismic hazards and using this calculated uncertainty to predict structural performance. This predicted structural response can help stakeholders define a desirable level of structural performance. Figure *5-5* provides a visual representation of the varying levels of seismic performance objectives. For example, critical structures (e.g. hospitals, nuclear waste facilities, power plants, emergency response facilities, etc.) must be designed to remain fully operational even after a rare seismic event, while less critical structures (e.g. shopping centers, office buildings, etc.) have a higher risk tolerance. PBEE helps stakeholders make informed decisions based on their level of tolerable risk.

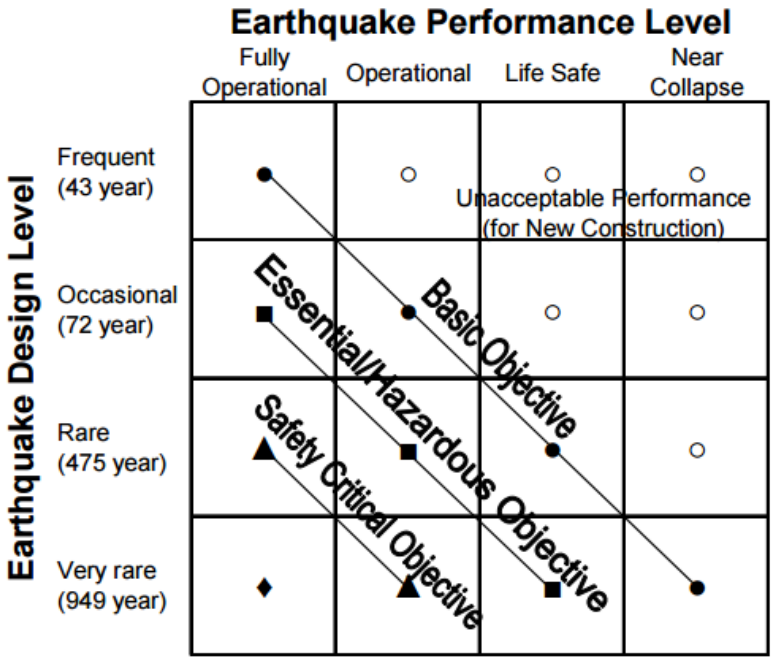

Figure 5-5: Design objectives for variable levels of risk and performance (after Porter, 2003).

The PEER framework developed an equation to represent PBEE (5-7). The PEER framework equation can be broken down into four main variables (Figure *5-6*). These variables include the following components (Deierlein et al., 2003):

- *Intensity Measure (IM):* a quantity that capture attributes of the ground motion hazard at a site. *IMs* are usually calculated by seismologists. *IMs* are scaler values that involve the consideration of nearby earthquake faults and the geologic characteristics of the surrounding region and nearby site. Examples of *IMs* include *PGA*, *PGV*, Arias Intensity (I_A), and other ground motion parameters.
- *Engineering Demand Parameter (EDP):* describes the structural response to the *IM* in terms of deformations, accelerations, or other structural response variables. The *EDP* can

relate to the structural system (e.g. story drift, strength deterioration, etc.) or the subsurface soil system below the structure (e.g. lateral spreading, settlement, FS_L, etc.). This study focuses on the *EDP* of settlement.

- *Damage Measure (DM):* describes the resulting physical condition of the structure and its components as a function of the imposed *EDPs*. *DMs* could include pile deflection, cracking, and collapse potential.
- *Decision Variable (DV):* quantifies *DM* into levels of risk. *DVs* translate damage measures into quantities that relate risk management decisions concerning economic and safety loss. Examples of *DVs* could include repair cost, lives lost, and down time.

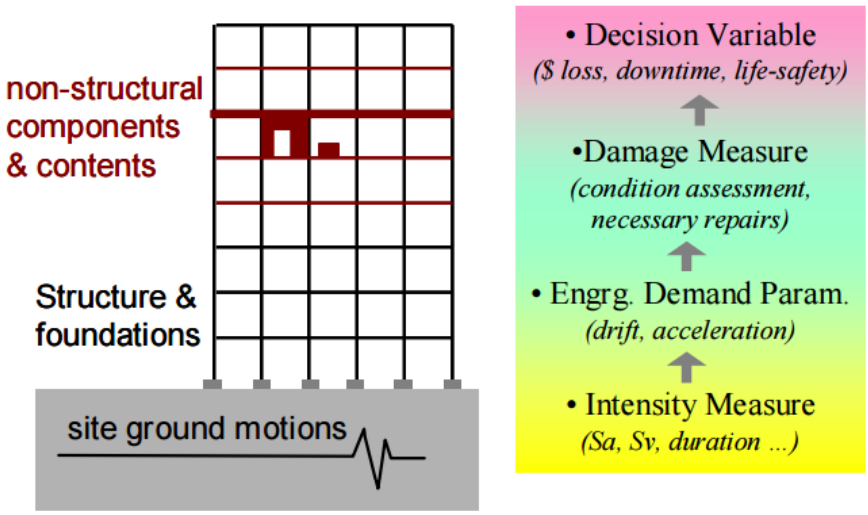

Figure 5-6: Variable components of the performance-based earthquake engineering framework equation (after Deierlein et al., 2003).

The PBEE framework equation is structured similarily to PSHA, in that it also calculates the mean annual rate of exceedance (λ) of a specific outcome for a range of possible seismic

scenarios. The outcome and possible siesmic scenarios are a specific *EDP* and ranges of a certain *IM*, respectively. The equation to calculate λ_{EDP} is given as:

$$\lambda_{EDP} = \int P[\, EDP > edp | IM = \, im_j] \Delta\lambda_{IM} \tag{5-6}$$

where $P[\, EDP > edp | IM = \, im_j]$ represents the probability that a specific *EDP* will exceed a certain level of edp, given a particular *IM*, and $\Delta\lambda_{IM}$ represents the incremental rate of exceedance of the *IM*. This process is then repeated for a specific range of levels of *EDPs* to calculate the total mean annual rate of eceedance of a DV (λ_{DV}). The complete PBEE framework equation can be represented by:

$$\lambda_{DV} = \int\int\int P[DV|DM]dP[DM|EDP]dP[EDP|IM]d\lambda_{IM} \tag{5-7}$$

which can be estimated numerically by:

$$\lambda_{DV} = \sum_{k=1}^{N_{DM}} \sum_{j=1}^{N_{EDP}} \sum_{i=1}^{N_{IM}} P[DV > dv|DM = dm_k] \times P\big[DM = dm_k \big| EDP = edp_j\big] \times P\big[EDP = edp_j \big| IM = im_i\big] \Delta\lambda_{IM} \tag{5-8}$$

where N_{DM}, N_{EDP}, and N_{IM} are the number of increments of *DM, EDP,* and *IM,* respectively. By iterating through a range of *DVs*, using equation (5-8), a hazard curve will be developed (Figure *5-7*). A hazard curve clearly indicates the probability of exceeding a range of specific *DVs*. Stakeholders can choose what level of risk, or *DV*, is needed for their project. Then, by using the hazard curve, engineers can obtain the λ_{DV} for the given risk level. The λ_{DV} will provide enigneers with a clear understanding of what seismic hazard risk level they need to design for.

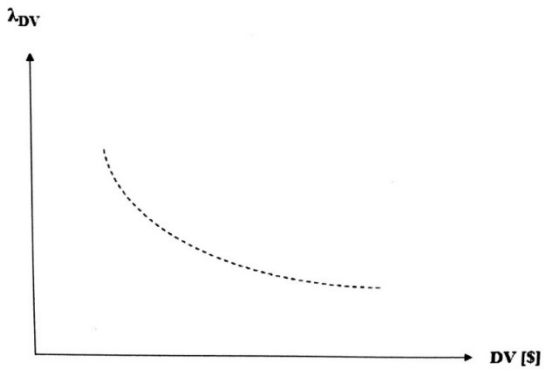

Figure 5-7: Example hazard curve for a given DV.

To apply the PEER framework to the estimation of post-liquefaction settlements, the PEER framework is also applied to liquefaction triggering. To apply a performance-based procedure to the liquefaction triggering calculations, FS_L hazard curves are developed using the Kramer and Mayfield (2007) PBEE approach. This approach utilizes the PEER PBEE framework by assigning the joint occurrence of M_w and a_{max} as an intensity measure and the FS_L as the engineering demand parameter. Engineers are more interested in when FS_L is expected to *not* exceed a certain value because FS_L, unlike other *EDPs*, is more favorable the larger it is. Therefore, Equation 5-6 is altered to predict the probability of non-exceedance, rather than the probability of exceedance. This new equation of non-exceedance is presented as:

$$\Lambda_{FS^*_L} = \sum_{j=1}^{N_M} \sum_{i=1}^{N_{a_{max}}} P[FS_L < FS^*_L | a_{max,i}, m_j] \Delta\lambda_{a_{max,i},m_j} \tag{5-9}$$

where $\Lambda_{FS^*_L}$ is the mean annual rate of *not* exceeding some given value of factor of safety (FS^*_L), N_M and $N_{a_{max}}$ are the number of magnitude and a_{max} increments into which the hazard space is subdivided, and $\Delta\lambda_{a_{max,i},m_j}$ is the incremental mean annual rate of exceedance for intensity measures $a_{max,i}$ and m_j.

Kramer and Mayfield also related performance based methodology with in-situ soil resistance by using the term N_{req}, which represents the SPT resistance required to prevent liquefaction. In other words, N_{req} is the number of blow counts required to prevent liquefaction or the condition of FS_L= 1. To apply this to the CPT q_{req} (i.e., the required tip resistance) can be used. Following the work of Kramer and Mayfield an expression for the mean annual rate of exceedance of the value q^*_{req} at a depth of interest can be defined as:

$$\lambda_{q^*_{req}} = \sum_{j=1}^{N_M} \sum_{i=1}^{N_{a_{max}}} P[q_{req} > q^*_{req} | a_{max,i}, m_j] \Delta\lambda_{a_{max,i}, m_j} \tag{5-10}$$

where

$$P\left[q_{req} > q^*_{req} \middle| a_{max,i}, m_j\right] = P_L(q^*_{req}) \tag{5-11}$$

Each of the two triggering procedures calculate Equation (5-11) differently. The Robertson and Wride (2009) P_L can be calculated as:

$$P_L = 1 - \Phi\left[\frac{0.102 + \ln\left(\frac{CRR}{CSR}\right)}{\sigma_{total}}\right] \tag{5-12}$$

where σ_{total} is the parameter and model uncertainty and is equal to 0.3537. The CRR and CSR are calculated according to Equations (3-3) through (3-14), but the input $Q_{tn,cs}$ is replaced with q^*_{req}. For the Boulanger and Idriss (2014) procedure, the P_L is calculated as:

$$P_L = \Phi\left[-\frac{\left(\frac{q^*_{c1Ncs}}{113}\right) + \left(\frac{q^*_{c1Ncs}}{1000}\right)^2 - \left(\frac{q^*_{c1Ncs}}{140}\right)^3 + \left(\frac{q^*_{c1Ncs}}{137}\right)^4 - 2.60 - \ln\left(CSR_{M=7.5,\sigma'_v=1atm}\right)}{\sigma_{\text{total}}}\right] \tag{5-13}$$

where σ_{total} is the parameter and model uncertainty and is equal to 0.506, q^*_{c1Ncs} is equal to q^*_{req}, and the $CSR_{M=7.5,\sigma'_v=1atm}$ is calculated using Equations (3-25) through (3-29).

Equation (5-10) is repeated for a range of q^*_{req} (1 to 250) for each triggering method and for every soil layer. These calculations result in a range of probabilities of exceedance (λ) corresponding to q_{req} values. This process develops a q_{req} hazard curve. Because FS_L and ΔN_L essentially provide the same information, Kramer and Mayfield (2007) provides a useful conversion between the two:

$$FS_L^{site} = \frac{CRR}{CSR} = \frac{CRR\ (N_{site})}{CRR\ (N_{req}^{site})} \tag{5-14}$$

This conversion may be applied to CPT data by using:

$$FS_L^{site} = \frac{CRR}{CSR} = \frac{CRR\ (q_{site})}{CRR\ (q_{req}^{site})} \tag{5-15}$$

where q_{site} is the measured corrected clean-sand equivalent CPT cone-tip resistance, and q_{req}^{site} is the computed corrected clean-sand equivalent CPT cone-tip resistance required to resist liquefaction at the site of interest. By using Equations (5-14) and (5-15), the q_{req} hazard curves are converted to FS_L hazard curves. When q_{req} is converted to FS_L the value $\lambda_{q^*_{req}}$ is automatically converted to an annual rate of non-exceedance of FS_L ($\Lambda_{FS^*_L}$).

These calculations complete the process of creating a FS_L hazard curve for one soil layer. This process is repeated for each soil layer so that a FS_L hazard curve exists for each soil layer and for each triggering method. An example FS_L hazard curve for one soil layer is presented in (Figure 5-8). Each of these FS_L hazard curves are used to calculate the PBEE predicted settlements.

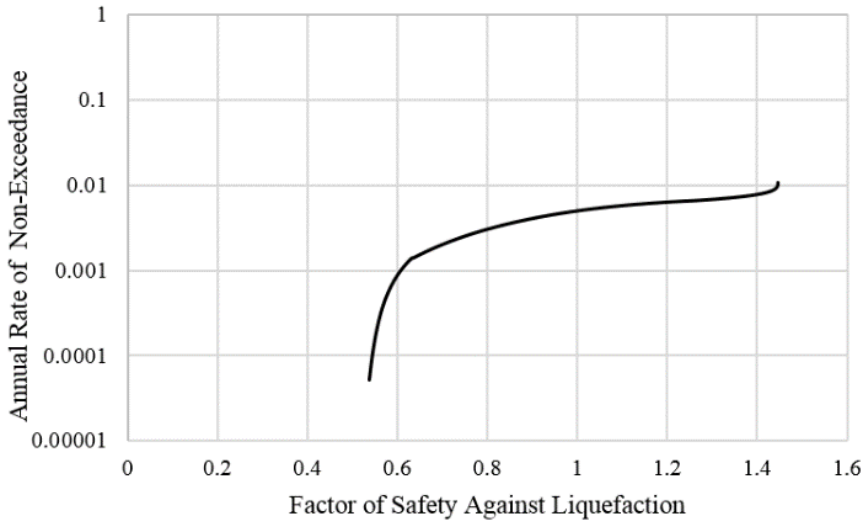

Figure 5-8: Example FS_L curve from one soil layer at a depth of 6m of a CPT profile shown in Figure 5-3 calculated at Eureka, CA.

After the PBEE liquefaction triggering assessment is completed, a PBEE post-liquefaction analysis can be performed. Equation (5-6) can be modified to calculate liquefaction-induced settlements by using the developed FS_L hazard curves, described above. The intensity measure is FS_L, which is used to calculate mean annual rate of exceedance of volumetric strain, the engineering demand parameter. The modified equation is given as:

$$\lambda_{\varepsilon_v{}^*} = \sum_{j=1}^{N_{FS_L}} P\left[\bar{\varepsilon_v} > \varepsilon_v{}^* \middle| q_{c1Ncsi}, FS_{Lj}\right] \Delta\lambda_{FS_{Lj}} \tag{5-16}$$

where $\lambda_{\varepsilon_v{}^*}$ is the mean annual rate of exceeding a specified level of strain ($\varepsilon_v{}^*$), N_{FS_L} is the number of FS_L increments within the current soil layer's FS_L hazard space, q_{c1Ncs} is the current layer's corrected cone tip resistance, $\Delta\lambda_{FS_{Lj}}$ is the incremental mean annual rate of exceedance for intensity measure FS_L, and $P\left[\varepsilon_v > \varepsilon_v{}^* \middle| q_{c1Ncsi}, FS_{Lj}\right]$ represents the probability the

calculated strain will exceed a specified level of strain ($\varepsilon_v{}^*$) given a specific incremental value from the FS_L hazard curve. The equation to calculate $P\left[\bar{\varepsilon_v} > \varepsilon_v{}^* \middle| q_{c1Ncsi}, FS_{Lj}\right]$ is given as:

$$P\left[\bar{\varepsilon_v} > \varepsilon_v{}^* \middle| q_{c1Ncsi}, FS_{Lj}\right] = \Phi\left[\frac{\ln(\bar{\varepsilon_v}) - \ln(\varepsilon^*{}_v)}{\sigma_{\ln(\varepsilon_v)}}\right] \quad (5\text{-}17)$$

where $\bar{\varepsilon_v}$ is the calculated strain using the Juang et al. (2013) strain equation (Equation 4-4) multiplied by P_L (Equation 4-5), $\sigma_{\ln(\varepsilon_v)}$ is taken to equal $\sigma_{\ln(s)}$ from Equation (4-5). $\sigma_{\ln(\varepsilon_v)}$ can be assumed to equal $\sigma_{\ln(s)}$because settlement is computed as a simple additive function of ε_v. The $P\left[\varepsilon_v > \varepsilon_v{}^* \middle| q_{c1Ncsi}, FS_{Lj}\right]$ values are computed for all of the incremental FS_L values. These probabilities are then summed to calculate the total mean annual rate of exceedance of that specific $\varepsilon_v{}^*$ value.

The calculated strain ($\bar{\varepsilon_v}$) is compared to the incremental $\varepsilon_v{}^*$ value. Equation (5-16) is repeated for a range of $\varepsilon_v{}^*$ values (0-20%), to account for all possible values of strain. All of the calculated $\lambda_{\varepsilon_v{}^*}$ values, with the corresponding $\varepsilon_v{}^*$ values, develop a hazard curve for one soil layer (Figure 5-9). This process is repeated for each soil layer to develop a strain hazard curve for each individual soil layer.

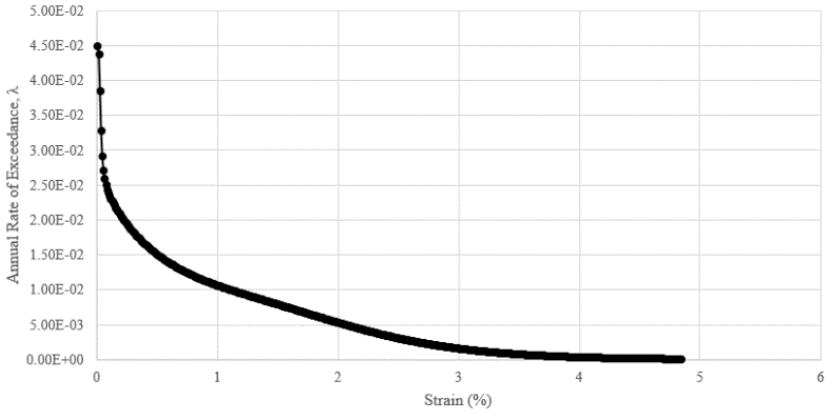

Figure 5-9: Example of one strain hazard curve from one specific soil layer at a depth of 6m of the CPT profile shown in Figure 5-3 calculated at Eureka, CA.

After strain hazard curves are developed for each soil layer, settlement is calculated. A hazard curve of total ground surface settlement is developed, by using each strain hazard curve from each layer. This calculation is done by using equation (4-3), from the Juang et al. (2013) procedure:

$$S_p = M \sum_{i=1}^{N} \varepsilon_v \Delta Z_i \tag{5-18}$$

where ε_v is a strain value is obtained from each strain hazard curve at the return period of interest from every soil layer. The strains from each soil layer are summed together and multiplied by the layer thickness to calculate ground surface settlement. This process is repeated for a range of mean annual rate of exceedances, corresponding to return periods from 475 years to 10,000 years, to develop a total settlement hazard curve (Figure *5-10*).

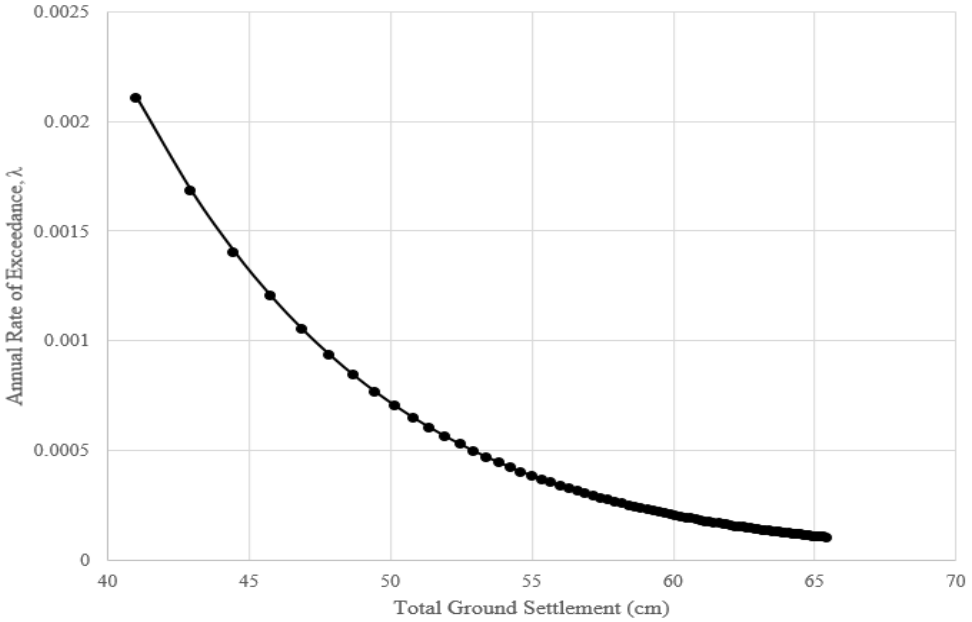

Figure 5-10: Example of a total ground settlement hazard curve using the CPT profile shown in Figure 5-3 calculated at Eureka, CA.

The PBEE settlement calculation has a higher level of accuracy and consistency than conventional methods due to its fully-probabilistic nature, and is presented in a more robust format than traditional methods. The PBEE calculation methods take into account all possible earthquake scenarios and all uncertainty attributed to predicting liquefaction triggering and uncertainty in predicting volumetric strain. In addition, by presenting settlement as a hazard curve rather than a single value, engineers confidently design for a level of post-liquefaction that is consistent with a targeted settlement to expect for a specific return period or level of hazard. Settlement hazard curves are very useful for an engineer to decide how much settlement a structure should be designed for, depending on structural importance. PBEE settlement results from this study are presented in chapter 6.

A PBEE settlement analysis is performed for the Salt Lake City, UT site. The analysis is performed using *CPTLiquefy* (see Section 5.3), an analysis tool. The analysis computed FS_L and strain hazard curves for each soil layer, just as the hazard curves presented in Figures 5-8 and 5-9. The FS_L, corresponding to the 2475 year return period, can be obtained from each layer's hazard curve and plotted with depth. This process is done for this example and is plotted in Figure *5-11*.

Figure 5-11: Fully-probabilistic FS_L values plotted across depth for the 2475 year return period at the Salt Lake City, UT site.

A strain hazard curve is computed for each individual soil layer using the procedure discussed in this section above. For this specific profile (Figure 5-3) a CPT reading was taken every 0.1m and, therefore, a strain hazard curve is computed every 0.1m from 0m to 12m, creating a total of 120 strain hazard curves. (Figure 5-12) depicts a few of these hazard curves at a range of depths. The performance-based procedure also allows strain to be plotted by depth for varying return periods (Figure 5-13).

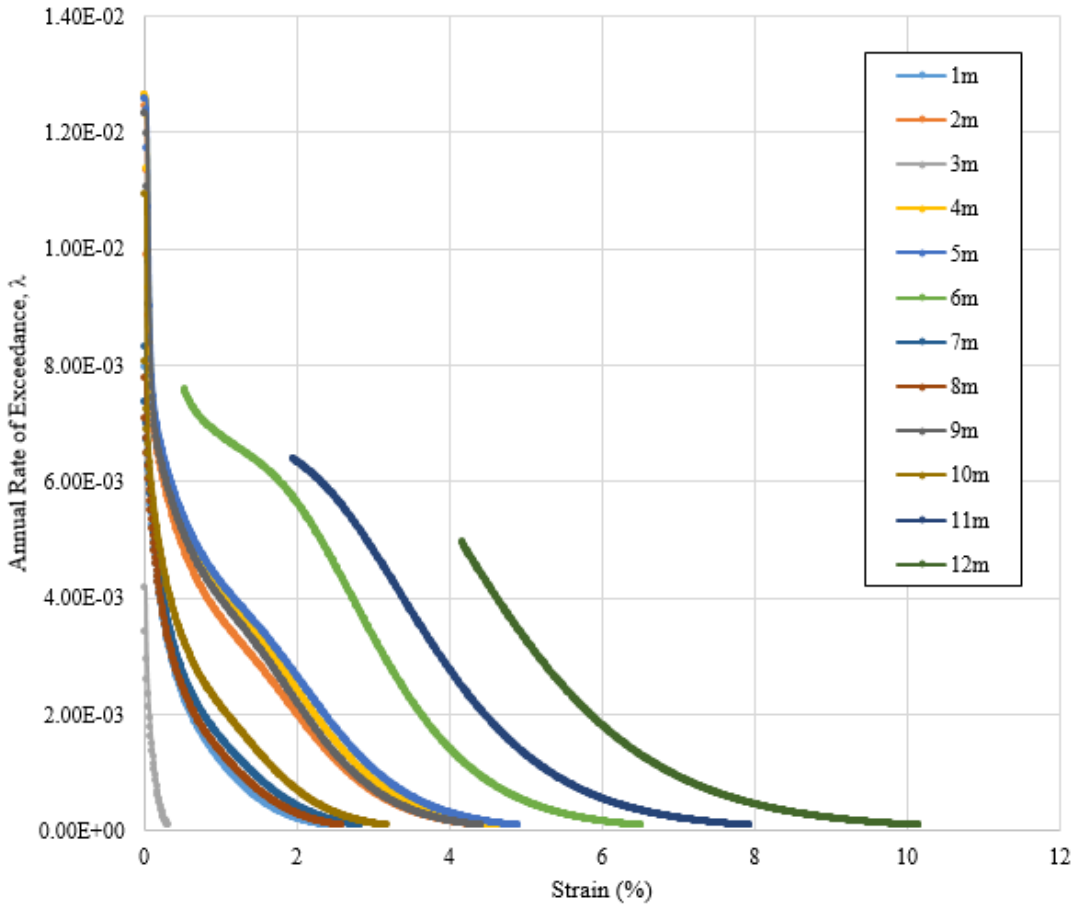

Figure 5-12: Strain hazard curves at the Salt Lake City Site at a range of depths.

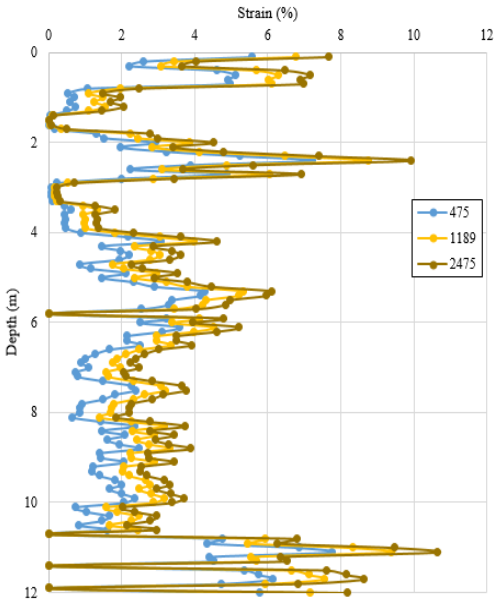

Figure 5-13: Strain across depth for the 475, 1189, and 2475 year return periods at the Salt Lake City Site.

These strain hazard curves are used to calculate a ground surface settlement hazard curve. The calculated ground surface settlement hazard curve, calculated using the process described above, for this example is plotted in Figure *5-14*. The dotted grey line corresponds to a return period of 2475 years, at which the calculated settlement is about 42.5cm.

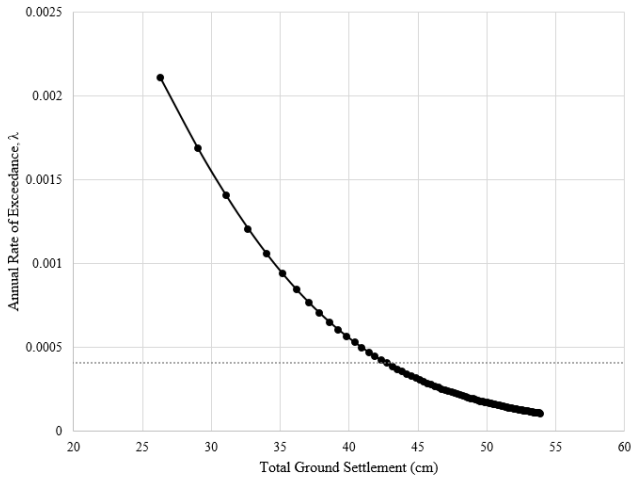

Figure 5-14: Salt Lake City, UT example calculated fully-probabilistic settlement estimation hazard curve.

5.2.4 Semi-Probabilistic Approach

Semi-probabilistic methods calculate FS_L using the fully probabilistic methods, described in section 5.2.3, and applies this FS_L to deterministic settlement calculations. This method accounts for the inherent uncertainty in predicting liquefaction triggering and correctly computes the return period of soil liquefaction. However, this method fails to account for the uncertainty in calculating post-liquefaction settlement.

For the Salt Lake City example, the calculated FS_L values (Figure *5-11*) for the 2475 year return period, are applied to the deterministic Ishihara and Yoshimine (1992) settlement estimation procedure. These FS_L values are obtained by selecting each FS_L value that corresponds to a 2475 return period from each FS_L hazard curve. The calculated strain values, calculated using the probabilistic FS_L values, are multiplied by their respective layer thicknesses and summed together to calculate ground surface settlement. The calculated semi-probabilistic post-liquefaction settlement, for the 2475 year return period, is about 34cm.

5.3 CPTLiquefY

To simplify PBEE (i.e., fully-probabilistic) procedures, the creation of tools to run such analyses is a very important step. Many practicing engineers simply do not have the understanding of, or the time to delve into, probability theory. The creation of tools can simplify the probabilistic design process by offering engineers a tool to run such calculations.

CPTLiquefY is an analysis tool which was created for the purpose of the analyses in this study and future research projects. *CPTLiquefY* was created by Mikayla Hatch, Tyler Coutu, and Alex Arndt under the direction of Dr. Kevin Franke at Brigham Young University. This program was created within Microsoft Visual Studio using C++. *CPTLiquefY* has the capability to load a

CPT profile and run deterministic, pseudo-probabilistic, semi-probabilistic, and full-probabilistic PBEE calculations for liquefaction triggering, post-liquefaction settlements, and lateral spreading. A tutorial on how to run these analyses, with *CPTLiquefY*, can be found in Appendix A.

As previously mentioned, this research is the first step to facilitate the creation of simplified probabilistic design tools, which engineers can instantly implement. Future research research will create settlement hazard maps, as done in previous PBEE studies for the SPT (Franke et al. 2014). Hazard maps will be developed by using the newly developed procedure for the CPT and *CPTLiquefY*. Hazard maps will depict contours of expected liquefaction-induced settlements, for specific locations, with a reference soil profile. See Ulmer (2015) and Ekstrom (2015) for more explanation on the development of liquefaction hazard maps and the benefit they provide to probabilistic design.

5.4 Chapter Summary

Earthquake engineers strive to design a structure at or above an estimated seismic event. There is a high level of uncertainty in determining the most likely earthquake event to occur at a site, making earthquake engineering design very difficult. Historically engineers used a DSHA, where design utilized the ground motions from the closest and most significant fault to the specified site. However, DSHA neglects the seismic hazard contribution of all other seismic sources near the fault and neglects the likelihood of the occurrence of the governing scenario earthquake. To address these issues, the PSHA was developed. PSHA takes into account all of the uncertainties relating to the size, location, and rate of occurrence of a seismic event by quantifying the likelihoods of each event actually occurring.

The PBEE method was advanced and refined by the PEER. The PEER PBEE framework seeks to improve risk decision-making through assessment and design methods that are more transparent, scientific, and informative to stakeholders than current prescriptive methods (Deierlein et al., 2003). The PEER framework facilitates crucial communication between stakeholders by presenting the risk and performance in a format each stakeholder can relate to. This chapter presented a new PBEE (i.e., fully-probabilistic) post-liquefaction settlement estimation procedure for the CPT. An analysis tool called *CPTLiquefY* was developed to perform these calculations.

It is not generally fully understood how the different ways of characterizing probabilistic ground motions in a post-liquefaction settlement analysis (i.e., pseudo-probabilistic, semi-probabilistic, and PBEE) effect the prediction of settlement. To address this lack of understanding, this research will now perform a comparative study between these different approaches. This comparative study will be presented and discussed in Chapter 6.

6 COMPARISON OF PERFORMANCE-BASED, PSEUDO-PROBABILISTIC, AND SEMI-PROBABILISTIC APPROACHES TO SETTLEMENT ANALYSIS

This study focuses on the quantified comparison of the difference in settlement calculations of the pseudo-probabilistic, semi-probabilistic, and PBEE (i.e., fully-probabilistic) methods. Post-liquefaction settlement estimations are calculated for each of the approaches, for multiple CPT profiles at multiple sites, and compared. The insufficiencies of conventional methods have been highlighted in this study, by comparing conventional methods to the PBEE approach. These results prove the need for a transition to fully-probabilistic design practices.

6.1 Methodology

To perform a thorough comparison of design methods, a comprehensive range of various soil conditions and site seismicity level needs to be considered. The methods to create a thorough comparative study are discussed below.

6.1.1 Soil Profiles

20 actual CPT soundings are selected, containing a comprehensive range of soil stiffness and type. These CPT soundings are collected from the United States Geologic Survey (USGS) database of CPT data (https://earthquake.usgs.gov/research/cpt/data/table/). The CPT profiles are selected with the intention to have a thorough range of soil type and relative density/stiffness. This range in relative density/stiffness is evident by investigating the plot of corrected cone tip resistance (Q_{tncs}) shown in Figure *6-1*. Note the lack of "holes" (i.e., white space) in Figure 6-1.

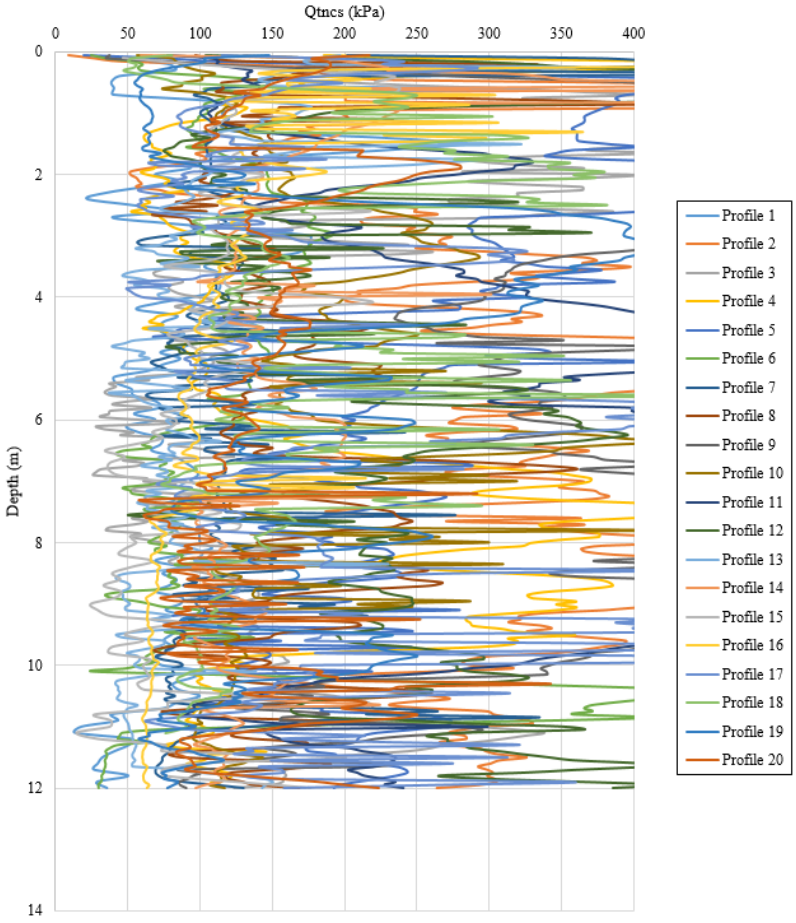

Figure 6-1: Stiffness of CPT profiles plotted at depth.

Figure 6-1 shows how the chosen profiles adequately cover all potentially impactful Q_{tncs}, or stiffness, values across the depth. Only a few profiles are found with a Q_{tncs} value less than 50kPa, because there are very few soils that exist naturally that are soft enough to have such a low value of Q_{tncs}. Also, any soil with a Q_{tncs} value greater than 250kPa is automatically considered too dense to liquefy per the liquefaction triggering databases of Boulanger and Idriss (2014) and Robertson and Wride (1998). Therefore, it is not imperative to collect comprehensive Q_{tncs} data greater than 250kPa. All collect profiles are summarized in Table 6-1.

Table 6-1: Summary of Soil Profiles

Profile	Name	Location	Latitude	Longitude	Source	Sand Content	Stiffness	Full Depth (m)	Date Collected
1	SFO029	San Francisco	37.824	-122.364	USGS	Medium	soft/very soft	17	1/21/1994
2	LWE001	Lawrence(ville), Ill	38.747	-87.511	USGS	High	med to hard	12.5	10/6/2004
3	HNC005	Evansville, IN/ KT	37.872	-87.702	USGS	Medium	med	20	12/6/2003
4	BDY002	Arkansas	33.278	-92.333	USGS	Medium	med	12	12/14/2005
5	SBC030	Riverside,CA	34.070	-117.290	USGS	High	med/hard	19	3/24/2001
6	BKY006	Charleston, SC	32.905	-79.924	USGS	High	soft	20	11/6/2004
7	MGA003	Matagorda, TX	28.765	-95.787	USGS	Low	soft	18.15	1/5/2006
8	SCR001	East St. Louis, Ill	38.620	-90.162	USGS	High	med	24	10/6/2008
9	SOC024	Oceano, CA	35.104	-120.631	USGS	High	med/hard	15	3/2/2004
10	POR006	Chesterton, IN	41.660	-87.051	USGS	Medium	soft/med	15	9/24/2004
11	HTN003	Upper peninsula, MI	47.159	-88.245	USGS	High	soft to hard	17	9/15/2004
12	SYC001	Memphis, TN	35.195	-89.987	USGS	Medium	soft/med	20	10/29/2003
13	BZA001	Freeport, TX	28.979	-95.285	USGS	low(interbedded)	soft	30	1/3/2006
14	CMN002	Rio grande valley, TX	25.953	-97.560	USGS	Medium	soft	20	1/14/2005
15	LAC076	Northridge, CA	34.227	-118.560	USGS	Low	soft	14	6/18/1996
16	RCD052	Fargo, ND	46.471	-96.834	USGS	very low	very soft	18	9/8/2008
17	SCC097	Santa Clara, CA	37.427	-122.041	USGS	Low	soft	18	6/26/2000
18	Oak061	Oakland, CA	37.818	-122.281	USGS	very low	very soft	20	3/30/1999
19	SCS001	St. Charles, MO	38.856	-90.212	USGS	very high	medium	24	10/6/2008
20	BKY021	North Charleston, SC	33.036	-79.736	USGS	Low	medium	20	11/14/2004

To accurately demonstrate the differences between design methods, independent variables such as total depth and water table depth are standardized. Each sounding had a different bottom depth. For this study, all profiles are truncated to 12m. This depth is chosen because the vast majority of liquefaction triggering case histories correspond to depths less than 12 meters (Boulanger et al., 2012). The depth of the water table can have a considerable impact on the about of liquefiable soil layers. For liquefaction to occur soils have to be saturated,

therefore any soils above the water table cannot liquefy. For this study, the water table is assumed to be at the ground surface. Finally, none of the CPT profiles from the USGS database contained a cone pore water pressure reading. For this study, the cone pore water pressure is assumed to be zero for each soil layer. Although altering the water table depth and assuming zero for the cone pore water pressure reading will alter the $Q_{tn,cs}$ values from what they actually are in the field, the purpose of this study is to compare the calculations from different design methods. These changes would be problematic if the purpose was to accurately predict liquefaction effects at a specific site. Because the purpose of this study is to simply compare calculation approaches, the specific CPT used in the study are irrelevant as long as they are consistent for the various approaches being tested. Therefore, these assumptions do not affect the accuracy or validity of this comparative study's results.

6.1.2 Site Locations

To address the potential variable levels of seismicity a site could have, ten different cities are examined in this study. Each city is chosen to represent a different level of seismicity and in part because they have been used in other PBEE studies (Kramer and Mayfield 2007, Franke et al. 2014). The chosen cities are distributed as such: 4 on the west coast near the San Andreas Fault, 2 in the pacific north-west near the Cascadia Subduction zone and associated faults, 2 near the Wasatch fault and rocky mountain region, 1 near the New Madrid fault system, and 1 near the Charleston liquefaction features. A map of the cities are shown in Figure 6-2.

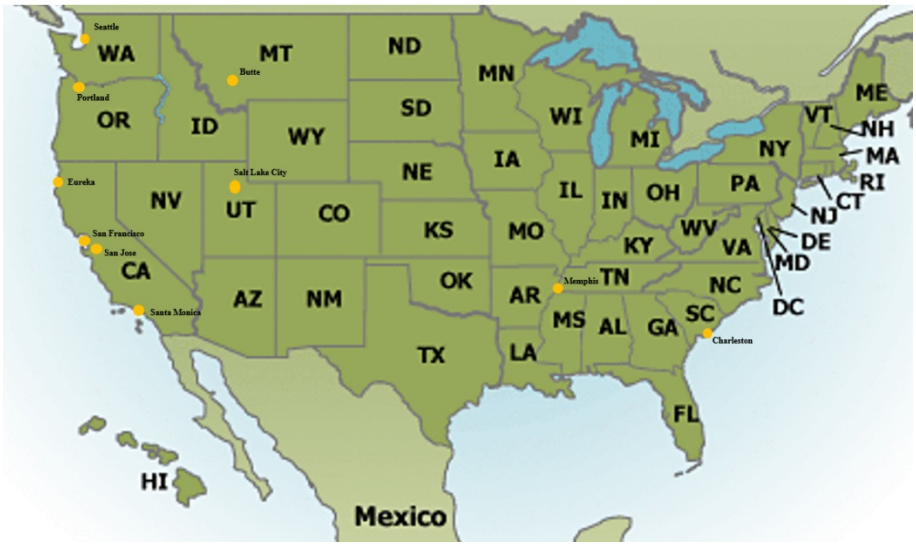

Figure 6-2: Map of all ten cities in this study.

Recently, USGS has released a new version of its seismic source model. This release provides several updates to probabilistic earthquake hazard calculation for the conterminous United States (Peterson et. al. 2015). The 2014 model has now replaced the 2008 USGS seismic source model as the most current version of the USGS National Seismic Hazard Mapping Project (NSHMP). This study utilizes the 2014 USGS model. This model is used to obtain the earthquake magnitude (mean and modal) and maximum acceleration (a_{max}) at each location. These values are presented in Table 6-2 for two return periods (475 year and 2475 year). The a_{max} values presented are calculated from the PGA using site amplification factors for AASHTO site class D. The values of a_{max} seen below were applied to the conventional pseudo-probabilistic analysis to represent the relative ground acceleration expected to possibly occur at each location.

Table 6-2: Magnitude (Mean and Modal) and Acceleration Values (USGS 2014), Using Site Amplification Factors for AASHTO Site Class D, Corresponding to T_R= 475 years and T_R=2475 years for each Site

City	Latitude	Longitude	Mean Magnitude (475 T_R / 2475 T_R)	Modal Magnitude (475 T_R / 2475 T_R)	PGA (g) (475 T_R / 2475 T_R)
Butte, MT	46.0038	-112.535	6.03 / 6.05	5.20 / 6.20	0.08344 / 0.1785
Charleston, S.C.	32.7765	-79.9311	6.61 / 7.00	7.36 / 7.37	0.1513 / 0.7287
Eureka, CA	40.8021	-124.164	7.33 / 7.45	6.99 / 6.99	0.6154 / 1.4004
Memphis, TN	35.1495	-90.049	6.98 / 7.24	7.70 / 7.70	0.1604 / 0.5711
Portland, OR	45.5231	-122.677	7.24 / 7.31	9.00 / 9.00	0.199 / 0.4366
Salt Lake City, UT	40.7608	-111.891	6.75 / 6.90	6.99 / 6.99	0.2126 / 0.6717
San Fran, CA	37.7749	-122.419	7.31 / 7.44	7.99 / 7.98	0.4394 / 0.7254
San Jose, CA,	37.3382	-121.886	6.66 / 6.66	6.60 / 6.60	0.456 / 0.6911
Santa Monica, CA	34.0195	-118.491	6.74 / 6.84	7.21 / 7.22	0.3852 / 0.7415
Seattle, WA	47.6062	-122.332	6.75 / 6.88	6.60 / 6.80	0.311 / 0.6432

6.1.3 Return Periods

Every structure is designed for a different level of earthquake depending on either the importance of that structure (e.g., hospitals, fire stations, etc.) or the level of negative impact resulting from structural failure (e.g., nuclear facilities, football stadiums, etc.). Less critical structures are designed for seismic events with shorter return periods, in other words smaller seismic events. While more critical structures are designed for higher return periods. This study focuses on return periods 475 years, 1039 years, and 2475 years, which correspond to probabilities of exceedance of 10% in 50 years, 7% in 75 years, and 2% in 50 years, respectively. These return periods represent relatively low, medium, and high levels of seismic loading, respectively.

6.2 Results and Discussion

This section presents the complete results from this study. As previously explained, all calculations are performed by applying a PBEE procedure to the Ishihara and Yoshimine (1992)

strain method, by using the Robertson and Wride (2009) and Boulanger and Idriss (2014) methods for the required FS_L inputs. The results are organized by city for each of the separate methods used. A discussion of the trends, patterns, and findings from these results is presented after the results sections. The results of the comparative analysis of the different hazard analyses and the sensitivity analysis of settlement correction factors, are also presented and discussed below.

6.2.1 Robertson and Wride (2009) Results

Tables 6-3 through 6-12 display all calculated results for the Robertson and Wride (2009) triggering procedure. These tables contain results for the fully-probabilistic, pseudo-probabilistic (both mean and modal magnitude), and semi-probabilistic methods for the 475 year, 1039 year, and 2475 year return periods. All settlement values are presented in centimeters.

Table 6-3: Butte, MT Settlement (cm) Calculated with Robertson and Wride Method

	Full Probabilistic			Mean Magnitude			Modal Magnitude			Semi-Probabilistic		
Profile	475	1039	2475	475	1039	2475	475	1039	2475	475	1039	2475
1	11.7	20.3	28.9	18.2	27.3	32.1	5.7	19.4	27.5	18.3	25.9	31.2
2	1.0	1.8	2.6	1.7	2.2	2.7	0.3	1.8	2.2	1.7	2.4	3.1
3	5.0	9.5	13.8	8.5	12.3	14.7	1.2	9.1	12.4	8.8	12.7	15.5
4	2.1	6.7	11.4	4.2	10.5	15.2	0.3	5.3	10.6	4.5	10.6	14.9
5	0.5	0.9	1.5	0.6	1.0	1.4	0.4	0.7	1.0	0.7	1.6	2.6
6	7.6	14.3	20.5	12.7	19.3	22.4	2.3	13.9	19.4	13.2	19.4	23.1
7	0.5	1.3	2.0	1.1	1.7	2.4	0.1	1.2	1.7	1.0	1.9	2.5
8	0.3	1.3	2.7	0.3	1.5	3.3	0.0	0.5	1.6	1.1	3.1	5.4
9	0.3	0.5	0.7	0.4	0.5	0.6	0.3	0.4	0.5	0.4	0.7	0.9
10	0.4	1.1	2.0	0.6	1.6	2.5	0.1	0.7	1.6	1.0	2.2	3.5
11	0.1	0.6	1.2	0.1	0.6	1.7	0.0	0.2	0.6	0.5	1.4	2.5
12	0.4	1.4	2.8	0.6	2.1	3.8	0.0	0.7	2.1	1.1	2.8	4.8
13	2.9	7.2	11.3	5.8	11.2	12.8	0.5	6.7	11.3	5.5	10.4	13.0
14	0.2	1.0	2.4	0.1	1.0	3.6	0.0	0.2	1.0	1.0	2.6	4.6
15	2.5	3.9	5.3	3.7	4.8	5.4	1.6	3.8	4.8	3.8	4.7	5.5
16	0.0	0.1	0.1	0.0	0.0	0.1	0.0	0.0	0.0	0.1	0.2	0.3
17	0.2	0.7	1.2	0.3	0.7	1.5	0.0	0.4	0.7	0.6	1.3	2.0
18	0.0	0.1	0.1	0.0	0.0	0.1	0.0	0.0	0.0	0.1	0.2	0.4
19	3.0	6.9	10.6	5.8	9.2	12.2	0.6	6.1	9.3	5.8	9.9	12.9
20	0.4	2.1	4.6	0.6	2.9	6.6	0.0	0.8	2.9	1.7	4.6	8.1

Table 6-4: Eureka, CA Settlement (cm) Calculated with Robertson and Wride Method

	Full Probabilistic			Mean Magnitude			Modal Magnitude			Semi-Probabilistic		
Profile	475	1039	2475	475	1039	2475	475	1039	2475	475	1039	2475
1	41.0	47.6	54.5	34.7	34.8	34.9	34.5	34.7	34.8	34.0	34.2	34.3
2	4.2	4.9	5.7	4.8	6.0	7.6	4.3	5.2	6.2	4.5	4.7	4.9
3	21.6	25.4	29.4	21.4	21.8	22.1	21.1	21.6	21.9	19.2	19.7	20.0
4	21.3	25.4	29.6	20.4	20.9	21.4	20.2	20.5	20.9	19.6	19.9	20.0
5	3.6	4.5	5.3	6.7	8.8	10.2	5.4	7.5	9.1	4.8	5.3	5.6
6	30.4	35.5	40.9	29.7	29.7	29.8	29.6	29.7	29.8	26.6	27.3	27.7
7	3.6	4.3	5.0	3.7	3.8	3.8	3.7	3.8	3.8	3.3	3.4	3.4
8	7.8	9.8	11.8	14.5	15.5	16.3	13.4	14.8	15.7	9.9	10.8	11.4
9	1.3	1.7	2.0	2.3	2.8	3.6	2.0	2.4	2.9	1.9	2.1	2.3
10	5.0	6.2	7.4	8.5	9.5	10.3	7.6	8.8	9.7	5.9	6.3	6.6
11	3.9	5.0	6.0	6.7	7.8	8.6	6.1	7.0	7.9	5.1	5.6	5.9
12	7.1	8.8	10.4	10.0	11.8	13.1	9.0	10.5	12.0	8.3	8.7	9.0
13	17.1	20.1	23.1	15.1	15.2	15.2	15.1	15.2	15.2	14.3	14.5	14.6
14	7.9	9.9	11.9	12.2	12.6	12.6	11.6	12.5	12.6	9.5	10.1	10.5
15	7.5	8.7	10.0	6.8	7.0	7.0	6.7	6.8	7.0	6.3	6.5	6.5
16	0.4	0.5	0.6	0.9	0.9	0.9	0.8	0.9	0.9	0.5	0.6	0.6
17	3.2	3.9	4.7	4.9	5.2	5.4	4.7	5.0	5.2	3.7	4.0	4.1
18	0.6	0.7	0.9	1.6	2.1	2.4	1.3	1.8	2.2	0.9	1.1	1.1
19	17.8	21.1	24.6	19.0	20.1	20.8	18.4	19.3	20.2	16.8	17.3	17.7
20	12.2	15.1	18.1	17.7	18.5	18.9	17.0	18.0	18.6	13.9	14.6	15.2

Table 6-5: Santa Monica, CA Settlement (cm) Calculated with Robertson and Wride Method

	Full Probabilistic			Mean Magnitude			Modal Magnitude			Semi-Probabilistic		
Profile	475	1039	2475	475	1039	2475	475	1039	2475	475	1039	2475
1	39.4	45.8	52.7	34.1	34.3	34.6	34.3	34.5	34.7	33.7	34.0	34.1
2	3.8	4.5	5.3	3.4	4.0	4.7	3.8	4.3	5.0	4.1	4.4	4.6
3	20.0	23.7	27.5	19.4	20.7	21.3	20.3	21.1	21.5	18.4	19.0	19.4
4	19.3	23.3	27.4	19.4	19.9	20.3	19.8	20.2	20.4	18.9	19.4	19.7
5	2.9	3.7	4.4	3.4	4.7	6.3	4.3	5.4	7.0	4.2	4.7	5.1
6	28.7	33.6	38.8	28.4	29.2	29.7	28.9	29.6	29.7	25.7	26.3	26.9
7	3.2	3.9	4.6	3.5	3.7	3.7	3.6	3.7	3.7	3.1	3.2	3.3
8	6.2	7.9	9.7	10.4	12.6	14.1	12.0	13.4	14.6	8.6	9.5	10.3
9	1.1	1.4	1.6	1.3	1.8	2.2	1.6	2.0	2.3	1.6	1.8	2.0
10	4.2	5.2	6.3	5.5	7.0	8.2	6.7	7.6	8.6	5.3	5.8	6.1
11	3.1	4.0	4.9	4.9	5.6	6.5	5.4	6.1	6.8	4.5	5.0	5.3
12	5.9	7.4	8.9	7.3	8.3	9.6	8.0	9.0	10.2	7.5	8.1	8.5
13	16.3	19.1	22.1	14.6	14.9	15.1	14.8	15.1	15.2	14.0	14.2	14.4
14	6.2	8.0	9.8	10.2	11.3	12.0	11.1	11.6	12.3	8.5	9.3	9.8
15	7.1	8.3	9.5	6.5	6.6	6.7	6.6	6.7	6.8	6.2	6.3	6.4
16	0.3	0.4	0.5	0.5	0.8	0.9	0.7	0.8	0.9	0.4	0.5	0.5
17	2.6	3.2	3.9	3.9	4.5	4.8	4.3	4.7	4.9	3.2	3.5	3.8
18	0.4	0.6	0.7	0.8	1.1	1.5	1.0	1.3	1.7	0.8	0.9	1.0
19	16.3	19.5	22.7	16.8	17.9	18.8	17.5	18.4	19.1	15.9	16.6	17.0
20	10.1	12.7	15.4	14.5	16.4	17.5	15.9	17.0	17.8	12.5	13.5	14.2

Table 6-6: Portland, OR Settlement (cm) Calculated with Robertson and Wride Method

	Full Probabilistic			Mean Magnitude			Modal Magnitude			Semi-Probabilistic		
Profile	475	1039	2475	475	1039	2475	475	1039	2475	475	1039	2475
1	24.9	33.5	41.4	31.7	33.8	34.0	30.6	33.9	34.1	30.3	33.4	33.8
2	2.3	3.2	4.1	2.6	2.9	3.3	2.5	3.0	3.4	2.9	3.9	4.3
3	12.0	16.9	21.4	14.4	17.2	19.0	13.8	17.8	19.3	15.2	17.8	18.7
4	10.3	16.1	21.1	14.6	18.3	19.2	13.1	18.6	19.3	14.1	18.2	19.2
5	1.3	2.3	3.3	1.4	2.0	3.0	1.3	2.3	3.2	2.4	3.7	4.4
6	17.7	24.4	30.3	22.2	24.7	28.0	21.3	25.7	28.3	22.5	25.2	26.1
7	1.8	2.7	3.5	2.3	2.9	3.3	2.1	3.0	3.4	2.4	3.0	3.2
8	2.6	5.0	7.2	3.1	5.9	9.5	2.5	6.9	10.1	4.9	7.8	9.1
9	0.6	0.9	1.2	0.6	0.7	1.1	0.5	0.8	1.2	0.9	1.4	1.7
10	1.9	3.4	4.7	2.4	3.7	5.0	2.1	4.0	5.3	3.3	4.9	5.6
11	1.2	2.5	3.6	1.5	3.2	4.6	1.1	3.6	4.7	2.3	4.1	4.8
12	2.6	4.8	6.7	3.6	5.9	6.9	3.0	6.2	7.2	4.4	6.9	7.8
13	9.9	13.8	17.3	12.8	13.7	14.4	12.5	13.9	14.6	12.7	13.8	14.2
14	2.3	4.9	7.3	3.1	7.2	9.7	2.1	8.0	10.0	4.2	7.6	9.0
15	4.5	6.0	7.5	5.3	6.0	6.4	5.2	6.2	6.4	5.4	6.0	6.2
16	0.1	0.2	0.4	0.1	0.2	0.5	0.1	0.3	0.5	0.2	0.4	0.5
17	1.1	2.1	2.9	1.4	2.6	3.7	1.1	2.9	3.8	1.9	3.0	3.4
18	0.1	0.3	0.5	0.1	0.3	0.6	0.0	0.4	0.7	0.4	0.7	0.9
19	9.4	13.7	17.6	12.0	14.5	16.4	11.0	15.1	16.7	12.4	15.3	16.3
20	4.3	8.1	11.5	6.1	10.5	13.7	5.0	11.4	14.2	7.4	11.6	13.1

Table 6-7: Salt Lake City, UT Settlement (cm) Calculated with Robertson and Wride Method

	Full Probabilistic			Mean Magnitude			Modal Magnitude			Semi-Probabilistic		
Profile	475	1039	2475	475	1039	2475	475	1039	2475	475	1039	2475
1	26.3	34.9	42.7	33.8	34.1	34.5	33.8	34.2	34.5	31.6	33.6	34.0
2	2.4	3.4	4.3	2.9	3.5	4.3	3.0	3.6	4.4	3.2	4.1	4.5
3	12.8	17.9	22.5	17.3	19.6	21.1	17.6	19.7	21.1	15.9	18.3	19.1
4	11.5	17.5	22.4	18.4	19.5	20.2	18.5	19.6	20.2	15.4	18.9	19.5
5	1.5	2.7	3.7	2.1	3.6	5.3	2.2	3.7	5.5	2.7	4.1	4.8
6	18.8	25.6	31.6	24.8	28.5	29.6	25.3	28.6	29.6	23.5	25.7	26.5
7	2.0	2.9	3.7	2.9	3.5	3.7	3.0	3.6	3.7	2.6	3.1	3.2
8	3.1	5.9	8.2	6.1	10.8	13.3	6.5	11.1	13.4	5.7	8.6	9.8
9	0.6	1.0	1.4	0.7	1.3	2.0	0.8	1.4	2.0	1.0	1.6	1.9
10	2.2	3.9	5.3	3.8	5.8	7.6	3.9	6.0	7.6	3.7	5.3	5.9
11	1.5	3.0	4.2	3.3	5.0	6.0	3.5	5.1	6.1	2.7	4.5	5.1
12	3.1	5.5	7.5	5.9	7.5	8.9	6.1	7.6	9.0	5.0	7.4	8.2
13	10.6	14.5	17.9	13.7	14.7	15.1	13.8	14.7	15.1	13.1	14.0	14.3
14	2.9	5.9	8.3	7.3	10.5	11.6	7.7	10.6	11.7	5.0	8.4	9.5
15	4.7	6.3	7.7	6.0	6.5	6.7	6.1	6.5	6.7	5.6	6.2	6.3
16	0.1	0.3	0.4	0.2	0.6	0.8	0.3	0.6	0.8	0.3	0.4	0.5
17	1.3	2.4	3.3	2.6	4.0	4.7	2.8	4.1	4.7	2.2	3.2	3.6
18	0.2	0.4	0.6	0.3	0.8	1.2	0.4	0.8	1.3	0.5	0.8	0.9
19	10.2	14.7	18.6	14.6	17.0	18.3	14.9	17.1	18.4	13.3	15.9	16.7
20	5.2	9.4	12.9	10.6	14.8	16.9	11.1	15.1	17.0	8.6	12.5	13.8

Table 6-8: San Francisco, CA Settlement (cm) Calculated with Robertson and Wride Method

	Full Probabilistic			Mean Magnitude			Modal Magnitude			Semi-Probabilistic		
Profile	475	1039	2475	475	1039	2475	475	1039	2475	475	1039	2475
1	40.6	47.1	53.9	34.3	34.5	34.7	34.4	34.6	34.7	33.8	34.0	34.2
2	4.0	4.7	5.5	3.8	4.3	4.9	4.1	4.5	5.2	4.2	4.5	4.7
3	20.9	24.6	28.5	20.3	21.0	21.4	20.9	21.2	21.6	18.6	19.2	19.5
4	20.5	24.5	28.6	19.8	20.1	20.4	20.0	20.3	20.5	19.2	19.6	19.8
5	3.2	4.0	4.7	4.3	5.3	6.8	4.9	5.9	7.4	4.4	4.8	5.2
6	29.8	34.7	39.9	28.9	29.6	29.7	29.4	29.6	29.7	26.0	26.5	27.0
7	3.4	4.1	4.7	3.6	3.7	3.7	3.7	3.7	3.8	3.1	3.2	3.3
8	6.9	8.7	10.4	11.9	13.3	14.5	12.9	13.8	14.8	9.0	9.8	10.5
9	1.2	1.5	1.8	1.6	2.0	2.3	1.8	2.1	2.4	1.7	1.9	2.1
10	4.6	5.6	6.7	6.6	7.5	8.5	7.2	7.9	8.8	5.5	5.9	6.2
11	3.5	4.4	5.3	5.4	6.0	6.8	5.8	6.3	7.0	4.7	5.1	5.4
12	6.5	8.0	9.5	8.0	8.9	10.0	8.5	9.3	10.5	7.7	8.2	8.6
13	16.9	19.7	22.7	14.8	15.1	15.1	15.0	15.1	15.2	14.1	14.3	14.4
14	7.0	8.8	10.6	11.0	11.6	12.2	11.4	11.9	12.5	8.8	9.5	9.9
15	7.3	8.5	9.8	6.6	6.7	6.8	6.6	6.7	6.8	6.2	6.3	6.4
16	0.3	0.4	0.5	0.7	0.8	0.9	0.8	0.8	0.9	0.5	0.5	0.5
17	2.8	3.5	4.2	4.3	4.7	4.9	4.6	4.8	5.0	3.4	3.6	3.9
18	0.5	0.6	0.8	1.0	1.2	1.6	1.1	1.4	1.8	0.8	0.9	1.0
19	17.2	20.3	23.6	17.5	18.3	19.0	18.0	18.6	19.3	16.2	16.8	17.2
20	11.1	13.8	16.5	15.9	16.9	17.8	16.6	17.3	18.0	13.0	13.8	14.4

Table 6-9: San Jose, CA Settlement (cm) Calculated with Robertson and Wride Method

	Full Probabilistic			Mean Magnitude			Modal Magnitude			Semi-Probabilistic		
Profile	475	1039	2475	475	1039	2475	475	1039	2475	475	1039	2475
1	62.1	71.0	80.5	34.3	34.5	34.7	34.3	34.4	34.6	33.9	34.1	34.2
2	4.4	5.0	5.8	3.8	4.3	4.8	3.8	4.2	4.6	4.3	4.5	4.7
3	23.2	26.6	30.2	20.3	21.1	21.4	20.2	21.0	21.3	18.8	19.2	19.5
4	22.4	26.0	30.0	19.8	20.2	20.4	19.7	20.1	20.3	19.3	19.6	19.8
5	3.4	4.0	4.7	4.3	5.4	6.6	4.2	5.1	6.2	4.5	4.9	5.2
6	32.3	37.1	42.3	28.9	29.6	29.7	28.9	29.5	29.7	26.1	26.6	27.0
7	3.8	4.3	5.0	3.6	3.7	3.7	3.6	3.7	3.7	3.2	3.3	3.3
8	7.3	8.8	10.3	11.9	13.3	14.4	11.8	13.1	14.0	9.3	9.9	10.5
9	1.3	1.5	1.8	1.6	2.0	2.2	1.6	1.9	2.2	1.7	1.9	2.1
10	4.9	5.8	6.8	6.6	7.6	8.4	6.6	7.4	8.1	5.7	6.0	6.2
11	3.7	4.4	5.3	5.4	6.0	6.7	5.4	5.9	6.5	4.8	5.2	5.4
12	6.9	8.2	9.6	8.0	8.9	9.9	7.9	8.7	9.5	7.9	8.3	8.6
13	18.7	21.4	24.3	14.8	15.1	15.1	14.8	15.0	15.1	14.2	14.3	14.4
14	7.3	8.9	10.5	11.0	11.6	12.2	11.0	11.5	12.0	9.1	9.6	9.9
15	8.2	9.3	10.5	6.6	6.7	6.8	6.6	6.7	6.7	6.3	6.4	6.4
16	0.4	0.4	0.5	0.7	0.8	0.9	0.7	0.8	0.9	0.5	0.5	0.5
17	3.0	3.6	4.2	4.3	4.7	4.9	4.3	4.6	4.8	3.5	3.7	3.9
18	0.5	0.6	0.7	1.0	1.3	1.6	0.9	1.2	1.5	0.9	0.9	1.0
19	18.9	21.8	24.9	17.5	18.3	18.9	17.4	18.2	18.7	16.4	16.8	17.2
20	11.7	14.1	16.5	15.9	17.0	17.7	15.8	16.7	17.4	13.3	13.9	14.4

Table 6-10: Seattle, WA Settlement (cm) Calculated with Robertson and Wride Method

	Full Probabilistic			Mean Magnitude			Modal Magnitude			Semi-Probabilistic		
Profile	475	1039	2475	475	1039	2475	475	1039	2475	475	1039	2475
1	34.3	41.2	48.2	33.9	34.1	34.3	34.0	34.2	34.4	33.3	33.8	34.0
2	3.2	4.0	4.8	3.1	3.5	4.0	3.3	3.7	4.2	3.8	4.2	4.4
3	17.1	21.1	25.0	18.3	19.5	20.8	19.0	20.0	21.0	17.6	18.5	19.1
4	16.1	20.5	24.8	18.9	19.4	20.0	19.2	19.7	20.1	18.0	19.1	19.5
5	2.3	3.1	3.9	2.6	3.5	4.7	3.0	4.0	5.2	3.6	4.3	4.8
6	24.8	30.1	35.4	26.6	28.5	29.3	28.0	28.7	29.5	25.1	25.9	26.4
7	2.7	3.4	4.1	3.1	3.5	3.7	3.3	3.6	3.7	3.0	3.1	3.2
8	4.8	6.7	8.5	8.0	10.6	12.7	9.5	11.5	13.1	7.5	8.9	9.7
9	0.9	1.2	1.5	0.9	1.3	1.8	1.1	1.5	1.9	1.3	1.6	1.8
10	3.3	4.5	5.6	4.3	5.6	7.1	5.0	6.3	7.4	4.8	5.4	5.9
11	2.4	3.4	4.3	4.0	4.9	5.7	4.5	5.2	5.9	4.0	4.7	5.1
12	4.6	6.3	7.9	6.5	7.4	8.4	6.9	7.8	8.8	6.6	7.6	8.2
13	14.0	17.1	20.2	14.1	14.7	15.0	14.4	14.8	15.0	13.7	14.1	14.3
14	4.7	6.7	8.7	8.7	10.3	11.3	9.6	10.8	11.5	7.3	8.7	9.4
15	6.2	7.4	8.7	6.2	6.5	6.6	6.4	6.6	6.7	6.0	6.2	6.3
16	0.2	0.3	0.4	0.3	0.6	0.8	0.5	0.7	0.8	0.4	0.4	0.5
17	2.0	2.8	3.5	3.2	4.0	4.5	3.7	4.2	4.7	2.9	3.3	3.6
18	0.3	0.5	0.6	0.5	0.8	1.1	0.6	0.9	1.2	0.7	0.8	0.9
19	13.8	17.2	20.6	15.7	16.9	17.9	16.4	17.3	18.2	15.1	16.1	16.7
20	7.9	10.9	13.7	12.3	14.6	16.4	13.7	15.5	16.8	11.2	12.9	13.7

Table 6-11: Memphis, TN Settlement (cm) Calculated with Robertson and Wride Method

	Full Probabilistic			Mean Magnitude			Modal Magnitude			Semi-Probabilistic		
Profile	475	1039	2475	475	1039	2475	475	1039	2475	475	1039	2475
1	19.9	30.6	39.0	33.4	34.1	34.3	33.9	34.2	34.6	27.8	33.3	33.9
2	1.8	2.9	3.9	2.9	3.3	4.0	3.0	3.8	4.5	2.6	3.8	4.3
3	9.4	15.4	20.4	16.4	19.2	20.8	18.1	20.1	21.2	13.7	17.5	18.8
4	7.6	14.8	20.3	17.6	19.3	20.0	18.8	19.7	20.3	11.9	18.0	19.3
5	1.0	2.1	3.3	1.8	3.2	4.8	2.5	4.1	5.8	1.8	3.6	4.5
6	14.1	22.2	28.8	23.7	28.2	29.3	26.2	28.8	29.6	20.6	25.1	26.1
7	1.4	2.5	3.4	2.7	3.4	3.7	3.1	3.6	3.7	2.1	3.0	3.2
8	1.7	4.6	7.2	5.0	10.0	12.7	7.5	11.7	13.7	3.7	7.5	9.2
9	0.5	0.8	1.2	0.6	1.2	1.8	0.9	1.5	2.1	0.7	1.3	1.7
10	1.3	3.2	4.7	3.4	5.2	7.1	4.2	6.5	7.9	2.6	4.8	5.6
11	0.7	2.3	3.6	2.8	4.7	5.7	3.9	5.3	6.3	1.7	3.9	4.8
12	1.7	4.4	6.6	5.2	7.1	8.4	6.3	7.9	9.3	3.4	6.6	7.9
13	7.7	12.6	16.4	13.4	14.6	15.0	14.0	14.8	15.1	11.4	13.7	14.2
14	1.4	4.6	7.3	6.0	9.9	11.3	8.4	10.9	11.8	3.1	7.3	9.0
15	3.7	5.5	7.1	5.8	6.4	6.6	6.2	6.6	6.7	5.0	6.0	6.3
16	0.1	0.2	0.4	0.2	0.5	0.8	0.3	0.7	0.8	0.2	0.4	0.5
17	0.8	1.9	2.9	2.2	3.8	4.6	3.1	4.3	4.8	1.5	2.9	3.4
18	0.1	0.3	0.5	0.2	0.7	1.1	0.4	0.9	1.4	0.3	0.7	0.9
19	7.2	12.6	16.9	13.6	16.6	17.9	15.5	17.4	18.6	10.9	15.1	16.3
20	2.8	7.5	11.4	9.2	14.1	16.5	11.9	15.7	17.3	5.5	11.2	13.2

Table 6-12: Charleston, SC Settlement (cm) Calculated with Robertson and Wride Method

	Full Probabilistic			Mean Magnitude			Modal Magnitude			Semi-Probabilistic		
Profile	475	1039	2475	475	1039	2475	475	1039	2475	475	1039	2475
1	18.2	29.8	38.5	33.2	34.1	34.6	33.9	34.2	34.7	26.3	33.3	33.9
2	1.6	2.9	3.9	2.8	3.4	4.5	3.0	3.8	4.9	2.5	3.8	4.4
3	8.5	15.1	20.3	16.1	19.4	21.2	18.0	20.2	21.4	12.9	17.6	18.9
4	6.6	14.5	20.3	17.2	19.4	20.3	18.7	19.7	20.4	10.9	18.0	19.4
5	0.8	2.1	3.4	1.7	3.3	5.9	2.4	4.2	6.9	1.6	3.6	4.6
6	12.8	21.7	28.6	23.4	28.4	29.6	26.0	28.8	29.7	19.7	25.1	26.3
7	1.2	2.4	3.4	2.7	3.5	3.7	3.0	3.6	3.7	1.9	3.0	3.2
8	1.4	4.6	7.5	4.6	10.3	13.8	7.2	11.7	14.6	3.2	7.6	9.5
9	0.4	0.8	1.2	0.6	1.3	2.1	0.8	1.5	2.3	0.7	1.3	1.8
10	1.1	3.1	4.8	3.2	5.5	7.9	4.1	6.5	8.5	2.3	4.8	5.7
11	0.6	2.3	3.8	2.7	4.8	6.3	3.8	5.3	6.8	1.5	4.0	4.9
12	1.4	4.4	6.8	5.0	7.3	9.3	6.3	7.9	10.1	2.9	6.7	8.0
13	6.9	12.3	16.2	13.3	14.6	15.1	14.0	14.8	15.2	10.6	13.8	14.2
14	1.1	4.6	7.5	5.5	10.2	11.9	8.2	10.9	12.3	2.7	7.4	9.2
15	3.4	5.4	7.0	5.8	6.5	6.7	6.2	6.6	6.8	4.8	6.0	6.3
16	0.1	0.2	0.4	0.2	0.5	0.8	0.3	0.7	0.9	0.2	0.4	0.5
17	0.7	1.9	3.0	2.0	3.9	4.8	3.0	4.3	4.9	1.3	2.9	3.5
18	0.1	0.3	0.5	0.2	0.7	1.4	0.4	0.9	1.7	0.2	0.7	0.9
19	6.4	12.3	16.8	13.3	16.8	18.6	15.3	17.4	19.1	10.1	15.2	16.5
20	2.3	7.5	11.7	8.7	14.4	17.3	11.7	15.7	17.8	4.8	11.3	13.5

6.2.2 Boulanger and Idriss (2014) Results

Tables 6-13 through 6-22 display all calculated results for the Boulanger and Idriss (2014) triggering procedure. These tables contain results for the full-probabilistic, pseudo-probabilistic (both mean and modal magnitude), and semi-probabilistic methods for the 475 year, 1039 year, and 2475 year return periods. All settlement values are presented in centimeters.

Table 6-13: Butte, MT Settlement (cm) Calculated with Boulanger and Idriss Method

	Full Probabilistic			Mean Magnitude			Modal Magnitude			Semi-Probabilistic		
Profile	475	1039	2475	475	1039	2475	475	1039	2475	475	1039	2475
1	14.2	25.9	34.5	24.1	29.2	29.6	19.3	28.2	29.5	21.6	29.1	29.6
2	2.0	3.2	4.5	3.0	3.4	3.9	2.7	3.3	3.7	2.8	3.5	4.1
3	4.7	12.2	18.7	10.2	15.5	17.6	6.6	13.9	16.8	8.3	15.4	18.1
4	5.6	13.9	20.6	12.3	17.5	19.1	8.5	15.7	18.7	9.8	17.4	19.4
5	0.4	1.3	2.5	0.8	1.9	2.7	0.5	1.5	2.3	0.7	1.9	3.0
6	8.7	17.9	26.0	16.0	21.2	24.1	11.4	19.9	22.5	13.9	21.4	25.2
7	1.1	2.6	3.9	2.3	3.2	3.5	1.7	3.0	3.4	2.0	3.2	3.7
8	1.1	4.1	7.9	2.8	6.3	9.0	1.6	5.1	7.6	2.4	6.5	10.1
9	0.4	0.6	0.8	0.5	0.6	0.7	0.5	0.5	0.6	0.5	0.6	0.8
10	0.9	3.0	5.8	2.1	4.6	6.4	1.3	3.6	5.6	1.8	4.7	7.2
11	0.5	2.2	4.1	1.3	3.5	4.5	0.8	3.0	4.0	1.1	3.5	4.8
12	1.4	5.1	8.4	3.5	7.3	8.1	2.0	6.4	7.9	2.7	7.2	8.3
13	5.2	11.3	15.7	10.2	13.1	13.8	7.4	12.7	13.5	8.5	13.1	14.0
14	0.4	2.7	7.2	1.4	5.0	9.1	0.5	3.2	7.3	1.3	5.2	10.3
15	2.4	5.0	6.8	4.5	5.7	5.7	3.5	5.4	5.7	3.8	5.6	5.7
16	0.2	0.6	1.0	0.5	0.8	1.1	0.3	0.7	0.9	0.3	0.8	1.1
17	0.9	3.3	5.6	2.2	4.8	5.5	1.3	3.9	5.3	1.8	4.7	5.7
18	0.3	1.4	2.7	0.8	2.2	2.9	0.4	1.8	2.7	0.7	2.2	3.0
19	4.4	10.0	14.9	8.2	12.5	14.5	6.0	11.4	13.6	7.2	12.6	15.1
20	1.1	5.9	12.0	3.2	9.4	13.5	1.5	7.5	11.7	2.7	9.7	14.9

Table 6-14: Eureka, CA Settlement (cm) Calculated with Boulanger and Idriss Method

	Full Probabilistic			Mean Magnitude			Modal Magnitude			Semi-Probabilistic		
Profile	475	1039	2475	475	1039	2475	475	1039	2475	475	1039	2475
1	43.1	49.3	56.1	30.1	30.3	30.4	29.9	30.1	30.4	30.0	30.3	30.4
2	6.3	7.3	8.4	4.8	5.1	5.6	4.7	4.9	5.3	4.8	5.0	5.3
3	26.6	30.8	35.3	19.6	19.8	20.0	19.4	19.6	19.8	19.5	19.8	19.9
4	28.1	32.4	37.0	20.2	20.4	20.6	20.2	20.3	20.4	20.2	20.4	20.5
5	5.4	6.9	8.5	5.5	6.5	7.4	4.9	5.7	6.5	5.3	6.5	7.4
6	36.9	42.5	48.5	26.6	26.6	26.7	26.6	26.6	26.6	26.6	26.6	26.6
7	5.5	6.4	7.4	4.0	4.0	4.5	4.0	4.0	4.3	4.0	4.0	4.0
8	15.5	18.9	22.3	14.3	14.8	15.2	13.6	14.4	14.9	14.1	14.8	15.2
9	1.7	2.3	2.9	2.1	2.4	2.7	1.6	2.1	2.5	1.9	2.4	2.7
10	11.5	13.9	16.4	9.8	10.2	10.7	9.5	9.9	10.2	9.7	10.2	10.7
11	7.4	9.0	10.7	6.6	6.9	7.3	6.3	6.7	6.9	6.5	6.9	7.2
12	12.4	14.6	17.0	9.6	10.1	10.6	9.4	9.7	10.1	9.5	10.1	10.6
13	20.8	23.8	27.1	14.4	14.4	14.8	14.4	14.4	14.6	14.4	14.4	14.4
14	15.1	18.1	21.2	13.1	13.1	13.2	13.0	13.1	13.2	13.1	13.1	13.1
15	8.8	10.1	11.5	5.9	6.0	6.6	5.9	6.0	6.4	5.9	6.0	6.0
16	1.6	1.9	2.2	1.2	1.2	1.7	1.2	1.2	1.5	1.2	1.2	1.2
17	8.3	9.8	11.3	6.2	6.3	6.7	6.1	6.3	6.6	6.2	6.3	6.4
18	4.5	5.4	6.2	3.6	3.6	4.0	3.5	3.6	3.9	3.6	3.6	3.6
19	22.1	25.8	29.8	17.4	17.7	18.2	17.1	17.5	17.9	17.3	17.7	18.0
20	22.8	27.3	31.8	18.7	19.0	19.1	18.4	18.8	19.0	18.7	19.0	19.1

Table 6-15: Santa Monica, CA Settlement (cm) Calculated with Boulanger and Idriss Method

	Full Probabilistic			Mean Magnitude			Modal Magnitude			Semi-Probabilistic		
Profile	475	1039	2475	475	1039	2475	475	1039	2475	475	1039	2475
1	42.2	48.2	54.7	29.7	29.8	30.0	29.7	29.9	30.1	29.7	29.9	30.2
2	5.9	6.9	8.0	4.6	4.7	4.8	4.7	4.7	4.9	4.6	4.7	4.8
3	25.4	29.6	34.1	19.2	19.4	19.5	19.3	19.5	19.6	19.3	19.5	19.6
4	27.1	31.4	36.0	20.0	20.1	20.2	20.1	20.2	20.3	20.1	20.2	20.3
5	4.5	5.6	6.8	4.1	4.6	5.2	4.4	4.9	5.5	4.3	5.0	5.7
6	35.5	41.2	47.2	26.6	26.6	26.6	26.6	26.6	26.6	26.6	26.6	26.6
7	5.2	6.1	7.1	3.8	3.9	4.0	3.9	4.0	4.0	3.9	4.0	4.0
8	13.7	16.7	19.9	12.6	13.3	14.0	13.1	13.7	14.3	12.9	13.7	14.4
9	1.3	1.7	2.0	1.3	1.5	1.8	1.4	1.6	2.1	1.4	1.7	2.2
10	10.3	12.7	15.0	9.0	9.4	9.7	9.3	9.5	9.8	9.2	9.6	9.9
11	6.5	8.0	9.5	5.7	6.1	6.5	5.9	6.3	6.6	5.8	6.4	6.7
12	11.5	13.7	15.9	8.8	9.2	9.5	9.1	9.4	9.6	8.9	9.4	9.7
13	20.1	23.2	26.6	14.4	14.4	14.4	14.4	14.4	14.4	14.4	14.4	14.4
14	13.4	16.5	19.6	12.2	12.9	13.1	12.7	13.0	13.1	12.5	13.1	13.1
15	8.5	9.8	11.2	5.8	5.8	5.9	5.8	5.9	5.9	5.8	5.9	5.9
16	1.5	1.8	2.1	1.2	1.2	1.2	1.2	1.2	1.2	1.2	1.2	1.2
17	7.9	9.3	10.7	6.0	6.1	6.2	6.1	6.1	6.2	6.0	6.1	6.3
18	4.1	4.9	5.8	3.3	3.5	3.5	3.4	3.5	3.6	3.4	3.5	3.6
19	20.7	24.3	28.2	16.5	17.0	17.3	16.8	17.1	17.4	16.7	17.2	17.5
20	20.6	25.0	29.4	17.6	18.1	18.6	18.0	18.4	18.7	17.8	18.5	18.8

Table 6-16: Portland, OR Settlement (cm) Calculated with Boulanger and Idriss Method

	Full Probabilistic			Mean Magnitude			Modal Magnitude			Semi-Probabilistic		
Profile	475	1039	2475	475	1039	2475	475	1039	2475	475	1039	2475
1	28.0	35.5	42.7	29.6	29.6	29.6	29.5	29.6	29.7	29.6	29.6	29.8
2	3.5	4.8	6.1	3.9	4.2	4.5	3.8	4.3	4.5	3.8	4.4	4.7
3	15.0	21.0	26.2	17.4	18.6	19.1	17.1	18.8	19.1	17.6	19.1	19.4
4	16.5	22.5	27.7	19.0	19.7	20.0	18.8	19.8	20.0	19.0	19.9	20.2
5	1.9	3.5	5.0	2.5	3.5	3.9	2.4	3.6	4.0	2.6	3.8	4.8
6	20.8	29.5	36.5	23.5	26.3	26.6	22.9	26.4	26.6	23.4	26.5	26.6
7	3.1	4.3	5.4	3.5	3.8	3.8	3.4	3.8	3.8	3.5	3.8	4.0
8	6.2	10.9	14.8	8.5	11.1	12.4	8.1	11.4	12.5	8.8	12.2	13.5
9	0.6	1.0	1.5	0.7	0.9	1.2	0.6	0.9	1.3	0.7	1.2	1.6
10	4.4	8.1	11.2	6.1	8.0	8.8	5.8	8.2	8.9	6.1	8.7	9.5
11	3.2	5.2	7.0	4.3	5.0	5.6	4.2	5.1	5.6	4.4	5.5	6.2
12	6.6	9.4	12.1	8.1	8.4	8.7	8.0	8.4	8.8	8.1	8.6	9.3
13	12.6	16.8	20.5	13.7	14.2	14.3	13.6	14.2	14.3	13.7	14.3	14.4
14	5.6	10.6	14.6	8.6	11.1	12.0	7.9	11.4	12.2	8.7	11.8	13.0
15	5.5	7.2	8.7	5.7	5.8	5.8	5.7	5.8	5.8	5.7	5.8	5.9
16	0.8	1.3	1.6	1.0	1.2	1.2	1.0	1.2	1.2	1.0	1.2	1.2
17	4.5	6.5	8.2	5.5	5.8	6.0	5.4	5.9	6.0	5.5	5.9	6.1
18	2.1	3.3	4.3	2.8	3.0	3.3	2.7	3.1	3.3	2.8	3.2	3.5
19	12.0	17.0	21.6	14.2	15.6	16.3	13.9	15.8	16.4	14.3	16.2	17.0
20	9.3	16.4	22.1	12.9	16.3	17.4	12.3	16.7	17.5	13.0	17.2	18.3

Table 6-17: San Francisco, CA Settlement (cm) Calculated with Boulanger and Idriss Method

	Full Probabilistic			Mean Magnitude			Modal Magnitude			Semi-Probabilistic		
Profile	475	1039	2475	475	1039	2475	475	1039	2475	475	1039	2475
1	42.7	48.8	55.4	29.7	29.9	30.1	29.8	30.0	30.2	29.8	30.0	30.3
2	6.1	7.1	8.2	4.6	4.7	4.8	4.7	4.8	4.9	4.7	4.8	4.9
3	26.1	30.3	34.7	19.3	19.4	19.6	19.4	19.5	19.7	19.4	19.5	19.7
4	27.6	31.9	36.5	20.1	20.2	20.2	20.2	20.2	20.3	20.1	20.2	20.3
5	4.8	6.0	7.3	4.4	4.9	5.5	4.8	5.2	5.8	4.6	5.3	6.1
6	36.3	42.0	48.0	26.6	26.6	26.6	26.6	26.6	26.6	26.6	26.6	26.6
7	5.4	6.3	7.2	3.9	4.0	4.0	3.9	4.0	4.0	3.9	4.0	4.0
8	14.5	17.6	20.8	13.1	13.6	14.2	13.5	13.9	14.5	13.2	14.1	14.6
9	1.5	1.8	2.3	1.4	1.6	2.0	1.6	1.8	2.2	1.5	1.9	2.3
10	10.9	13.2	15.5	9.3	9.5	9.8	9.4	9.7	9.9	9.4	9.7	10.1
11	6.9	8.4	10.0	5.9	6.3	6.6	6.2	6.5	6.7	6.1	6.5	6.8
12	11.9	14.1	16.3	9.1	9.4	9.6	9.3	9.5	9.8	9.2	9.5	9.9
13	20.5	23.6	26.9	14.4	14.4	14.4	14.4	14.4	14.4	14.4	14.4	14.4
14	14.3	17.3	20.4	12.7	13.0	13.1	13.0	13.1	13.1	12.9	13.1	13.1
15	8.7	9.9	11.3	5.8	5.9	5.9	5.8	5.9	5.9	5.8	5.9	6.0
16	1.6	1.9	2.1	1.2	1.2	1.2	1.2	1.2	1.2	1.2	1.2	1.2
17	8.1	9.5	11.0	6.1	6.1	6.2	6.1	6.2	6.3	6.1	6.2	6.3
18	4.3	5.1	6.0	3.4	3.5	3.6	3.5	3.5	3.6	3.5	3.6	3.6
19	21.4	25.0	28.9	16.8	17.1	17.4	17.0	17.2	17.5	16.9	17.3	17.6
20	21.7	26.1	30.5	18.0	18.4	18.7	18.3	18.6	18.8	18.1	18.6	18.9

Table 6-18: Salt Lake City, UT Settlement (cm) Calculated with Boulanger and Idriss Method

	Full Probabilistic			Mean Magnitude			Modal Magnitude			Semi-Probabilistic		
Profile	475	1039	2475	475	1039	2475	475	1039	2475	475	1039	2475
1	28.7	36.2	43.4	29.6	29.7	29.9	29.6	29.7	29.9	29.6	29.7	29.9
2	3.8	5.1	6.4	4.2	4.6	4.7	4.2	4.6	4.8	4.1	4.6	4.7
3	16.1	22.0	27.1	18.6	19.2	19.4	18.7	19.3	19.5	18.1	19.2	19.5
4	17.5	23.3	28.5	19.7	20.0	20.2	19.7	20.0	20.2	19.4	20.0	20.2
5	2.3	3.9	5.5	3.4	4.2	4.9	3.5	4.2	4.9	3.0	4.2	5.1
6	22.5	30.7	37.5	26.1	26.6	26.6	26.2	26.6	26.6	25.1	26.6	26.6
7	3.4	4.5	5.6	3.8	3.8	4.0	3.8	3.9	4.0	3.6	3.8	4.0
8	7.3	12.0	16.0	10.9	12.7	13.6	11.1	12.8	13.7	10.0	12.7	13.8
9	0.7	1.2	1.7	0.9	1.3	1.6	0.9	1.3	1.6	0.8	1.3	1.8
10	5.4	9.1	12.0	7.8	9.1	9.5	8.0	9.1	9.5	7.0	9.1	9.6
11	3.7	5.7	7.6	5.0	5.7	6.3	5.0	5.8	6.3	4.8	5.8	6.4
12	7.2	10.0	12.7	8.4	8.8	9.4	8.4	8.9	9.4	8.3	8.9	9.4
13	13.3	17.3	21.1	14.2	14.4	14.4	14.2	14.4	14.4	14.0	14.4	14.4
14	7.0	11.8	15.7	11.0	12.4	13.0	11.2	12.5	13.1	10.2	12.4	13.1
15	5.7	7.3	8.8	5.8	5.8	5.9	5.8	5.8	5.9	5.7	5.8	5.9
16	0.9	1.3	1.7	1.2	1.2	1.2	1.2	1.2	1.2	1.1	1.2	1.2
17	4.9	6.8	8.5	5.8	6.0	6.1	5.9	6.0	6.1	5.7	6.0	6.2
18	2.4	3.6	4.6	3.0	3.3	3.5	3.1	3.4	3.5	2.9	3.3	3.5
19	12.9	17.9	22.4	15.6	16.5	17.1	15.7	16.6	17.1	15.0	16.6	17.2
20	11.2	18.1	23.6	16.1	17.7	18.4	16.3	17.8	18.4	14.7	17.7	18.5

Table 6-19: San Jose, CA Settlement (cm) Calculated with Boulanger and Idriss Method

	Full Probabilistic			Mean Magnitude			Modal Magnitude			Semi-Probabilistic		
Profile	475	1039	2475	475	1039	2475	475	1039	2475	475	1039	2475
1	64.8	73.3	82.5	29.7	29.9	30.0	29.7	29.8	30.0	29.8	30.1	30.3
2	6.7	7.6	8.7	4.7	4.7	4.8	4.7	4.7	4.8	4.7	4.8	4.9
3	28.9	33.0	37.3	19.3	19.4	19.5	19.3	19.4	19.5	19.4	19.5	19.7
4	30.7	34.8	39.3	20.1	20.2	20.2	20.1	20.2	20.2	20.2	20.2	20.3
5	5.4	6.5	7.6	4.4	4.9	5.3	4.4	4.8	5.1	4.8	5.4	6.1
6	39.4	44.9	50.8	26.6	26.6	26.6	26.6	26.6	26.6	26.6	26.6	26.6
7	6.0	6.8	7.7	3.9	4.0	4.0	3.9	4.0	4.0	4.0	4.0	4.0
8	16.3	19.1	22.1	13.0	13.6	14.1	13.0	13.5	13.9	13.5	14.1	14.6
9	1.6	2.0	2.3	1.4	1.6	1.9	1.4	1.6	1.8	1.6	2.0	2.3
10	12.3	14.4	16.6	9.3	9.5	9.8	9.3	9.5	9.7	9.5	9.8	10.1
11	7.8	9.1	10.5	5.9	6.3	6.5	5.9	6.2	6.4	6.2	6.5	6.8
12	13.3	15.4	17.5	9.1	9.4	9.5	9.0	9.3	9.5	9.3	9.6	9.9
13	22.7	25.7	29.0	14.4	14.4	14.4	14.4	14.4	14.4	14.4	14.4	14.4
14	16.1	18.9	21.8	12.8	13.0	13.1	12.7	13.0	13.1	13.0	13.1	13.1
15	9.6	10.8	12.2	5.8	5.9	5.9	5.8	5.9	5.9	5.9	5.9	6.0
16	1.8	2.0	2.3	1.2	1.2	1.2	1.2	1.2	1.2	1.2	1.2	1.2
17	9.1	10.4	11.8	6.1	6.1	6.2	6.1	6.1	6.2	6.1	6.2	6.3
18	4.8	5.6	6.4	3.4	3.5	3.6	3.4	3.5	3.5	3.5	3.6	3.6
19	23.7	27.2	30.9	16.8	17.1	17.3	16.8	17.1	17.2	17.1	17.3	17.6
20	24.4	28.4	32.6	18.0	18.4	18.6	18.0	18.3	18.6	18.3	18.7	18.9

Table 6-20: Seattle, WA Settlement (cm) Calculated with Boulanger and Idriss Method

	Full Probabilistic			Mean Magnitude			Modal Magnitude			Semi-Probabilistic		
Profile	475	1039	2475	475	1039	2475	475	1039	2475	475	1039	2475
1	37.3	43.6	50.2	29.6	29.7	29.8	29.6	29.7	29.8	29.6	29.7	30.0
2	5.0	6.2	7.3	4.3	4.6	4.7	4.4	4.6	4.7	4.4	4.6	4.7
3	21.9	26.4	31.0	18.9	19.2	19.4	19.1	19.3	19.4	19.0	19.4	19.5
4	23.5	28.1	32.8	19.9	20.0	20.1	20.0	20.1	20.2	19.9	20.1	20.2
5	3.6	4.8	6.0	3.7	4.1	4.6	3.9	4.3	4.8	3.8	4.5	5.2
6	30.7	36.9	43.1	26.5	26.6	26.6	26.6	26.6	26.6	26.5	26.6	26.6
7	4.5	5.4	6.4	3.8	3.8	4.0	3.8	3.9	4.0	3.8	3.9	4.0
8	11.1	14.5	17.8	11.8	12.7	13.3	12.2	12.9	13.6	12.0	13.1	14.0
9	1.1	1.4	1.8	1.0	1.3	1.5	1.2	1.4	1.6	1.1	1.5	1.8
10	8.3	10.9	13.4	8.5	9.0	9.4	8.8	9.2	9.5	8.6	9.3	9.7
11	5.3	6.9	8.5	5.3	5.7	6.1	5.5	5.8	6.3	5.4	6.0	6.5
12	9.8	12.1	14.4	8.5	8.8	9.2	8.7	9.0	9.3	8.6	9.1	9.5
13	17.6	20.9	24.3	14.3	14.4	14.4	14.3	14.4	14.4	14.3	14.4	14.4
14	10.8	14.2	17.5	11.6	12.3	12.9	11.9	12.6	13.0	11.8	12.8	13.1
15	7.5	8.8	10.2	5.8	5.8	5.8	5.8	5.8	5.9	5.8	5.8	5.9
16	1.3	1.6	1.9	1.2	1.2	1.2	1.2	1.2	1.2	1.2	1.2	1.2
17	6.8	8.2	9.7	5.9	6.0	6.1	5.9	6.0	6.1	5.9	6.1	6.2
18	3.4	4.3	5.2	3.2	3.3	3.5	3.2	3.4	3.5	3.2	3.4	3.5
19	17.7	21.6	25.6	16.0	16.5	17.0	16.2	16.7	17.1	16.1	16.8	17.3
20	16.9	21.8	26.5	17.0	17.6	18.2	17.3	17.9	18.3	17.1	18.0	18.5

Table 6-21: Memphis, TN Settlement (cm) Calculated with Boulanger and Idriss Method

	Full Probabilistic			Mean Magnitude			Modal Magnitude			Semi-Probabilistic		
Profile	475	1039	2475	475	1039	2475	475	1039	2475	475	1039	2475
1	24.5	33.1	40.5	29.6	29.7	29.8	29.6	29.7	29.9	29.4	29.6	29.8
2	3.0	4.5	5.9	4.1	4.5	4.7	4.2	4.6	4.8	3.6	4.3	4.7
3	12.5	19.5	25.0	18.2	19.1	19.4	18.8	19.3	19.5	16.4	18.9	19.4
4	14.0	20.9	26.5	19.4	20.0	20.1	19.7	20.1	20.2	18.4	19.9	20.1
5	1.4	3.2	4.8	3.1	4.0	4.7	3.6	4.4	5.1	2.1	3.7	4.7
6	17.5	27.3	34.8	25.3	26.6	26.6	26.3	26.6	26.6	22.0	26.5	26.6
7	2.6	4.0	5.2	3.7	3.8	4.0	3.8	3.9	4.0	3.3	3.8	3.9
8	4.6	9.9	14.2	10.2	12.5	13.3	11.4	13.0	13.8	7.3	11.8	13.4
9	0.6	0.9	1.4	0.8	1.2	1.5	1.0	1.4	1.8	0.6	1.0	1.5
10	3.4	7.5	10.8	7.2	8.9	9.4	8.1	9.2	9.6	5.2	8.5	9.4
11	2.5	4.8	6.8	4.8	5.6	6.1	5.1	5.9	6.4	3.8	5.3	6.2
12	5.4	8.8	11.6	8.3	8.7	9.2	8.4	9.0	9.5	7.6	8.6	9.2
13	10.9	15.6	19.6	14.0	14.3	14.4	14.2	14.4	14.4	13.3	14.3	14.4
14	3.7	9.7	14.0	10.4	12.1	12.9	11.3	12.7	13.1	6.4	11.6	12.9
15	4.8	6.7	8.2	5.7	5.8	5.8	5.8	5.8	5.9	5.7	5.8	5.8
16	0.6	1.2	1.5	1.1	1.2	1.2	1.2	1.2	1.2	0.9	1.2	1.2
17	3.6	6.0	7.8	5.7	6.0	6.1	5.9	6.0	6.2	5.2	5.9	6.1
18	1.6	3.0	4.2	3.0	3.3	3.5	3.1	3.4	3.5	2.4	3.2	3.5
19	10.0	15.7	20.6	15.1	16.4	17.0	15.8	16.7	17.2	13.2	16.0	17.0
20	6.9	15.2	21.2	15.0	17.5	18.2	16.5	17.9	18.5	10.9	17.0	18.2

Table 6-22: Charleston, SC Settlement (cm) Calculated with Boulanger and Idriss Method

	Full Probabilistic			Mean Magnitude			Modal Magnitude			Semi-Probabilistic		
Profile	475	1039	2475	475	1039	2475	475	1039	2475	475	1039	2475
1	24.3	32.9	40.5	29.6	29.7	29.9	29.6	29.7	30.1	29.4	29.6	29.9
2	3.0	4.5	5.9	4.1	4.6	4.8	4.2	4.6	4.9	3.6	4.4	4.7
3	12.6	19.7	25.2	18.2	19.2	19.5	18.8	19.3	19.6	16.5	19.0	19.4
4	14.1	21.0	26.6	19.4	20.0	20.2	19.7	20.1	20.2	18.5	19.9	20.2
5	1.5	3.3	5.0	3.1	4.1	5.0	3.6	4.4	5.5	2.2	3.8	4.9
6	17.5	27.5	34.9	25.4	26.6	26.6	26.4	26.6	26.6	22.2	26.5	26.6
7	2.7	4.1	5.2	3.7	3.8	4.0	3.8	3.9	4.0	3.3	3.8	4.0
8	4.8	10.3	14.6	10.2	12.6	13.8	11.4	13.0	14.3	7.4	12.0	13.6
9	0.5	1.0	1.5	0.8	1.3	1.7	0.9	1.4	2.0	0.6	1.1	1.6
10	3.5	7.7	11.0	7.2	9.0	9.6	8.1	9.3	9.8	5.3	8.6	9.5
11	2.6	4.9	7.0	4.8	5.7	6.4	5.1	5.9	6.6	3.9	5.4	6.3
12	5.6	8.9	11.8	8.3	8.8	9.4	8.4	9.0	9.6	7.7	8.6	9.3
13	10.9	15.7	19.6	14.0	14.4	14.4	14.2	14.4	14.4	13.3	14.3	14.4
14	4.0	10.0	14.4	10.4	12.2	13.1	11.3	12.7	13.1	6.7	11.8	13.0
15	4.8	6.7	8.3	5.8	5.8	5.9	5.8	5.8	5.9	5.7	5.8	5.9
16	0.6	1.2	1.6	1.1	1.2	1.2	1.2	1.2	1.2	0.9	1.2	1.2
17	3.7	6.1	7.9	5.7	6.0	6.2	5.9	6.0	6.2	5.2	5.9	6.1
18	1.7	3.1	4.3	3.0	3.3	3.5	3.1	3.4	3.6	2.5	3.2	3.5
19	10.1	15.9	20.8	15.2	16.5	17.2	15.8	16.7	17.4	13.3	16.1	17.1
20	7.2	15.6	21.7	15.2	17.6	18.5	16.6	17.9	18.7	11.1	17.2	18.3

6.2.3 Comparison Analysis of Pseudo-Probabilistic, Semi-Probabilistic, and Performance-Based Methods

From the data above, and by comparing the pseudo-probabilistic and PBEE (i.e., fully-probabilistic) methods, several trends are identified from the data. First, in areas of low seismicity the pseudo-probabilistic methods calculated about 10-50% higher settlement values than the PBEE method. This relationship is logical because the pseudo-probabilistic method does not take into account the low probability of large earthquakes occurring. However, with higher return periods, the PBEE method predicted about 5-50% more settlement than pseudo-probabilistic procedures. Second, in areas of medium to high seismicity the pseudo-probabilistic method predicts similar settlement values to the full-probabilistic method for lower return periods, but about 30-100% less settlement values at higher return periods. The higher the return period and the seismicity of a city, the more the pseudo-probabilistic method under-predicts settlements. Observations support those found in a similar PBEE liquefaction-induced settlement study for the SPT (B. D. Peterson, 2016). Finally, by comparing the liquefaction triggering methods, both methods generally calculate similar settlement values, but the Boulanger and Idriss method proves to be more conservative than the Robertson and Wride method.

A comparative study is also performed for the semi-probabilistic settlement approach and the PBEE settlement approach. Similar trends observed from the pseudo-probabilistic comparative study are observed from the semi-probabilistic approach. However, at the higher return periods, the semi-probabilistic approach tends to under-predict settlements marginally more than the pseudo-probabilistic approach. Also, across all return periods, the data scatter for the semi-probabilistic approach is tighter than the pseudo-probabilistic results. This trend

indicates a slightly higher level of consistency and efficiency as compared to the pseudo-probabilistic approach.

To see these trends visually, comparison plots are created to compare the pseudo-probabilistic and semi-probabilistic results to the full-probabilistic results. These plots are presented in Figures 6-3 through 6-20. The solid black line represents the one-to-one line (i.e., a perfect match between the two approaches), and the data from each liquefaction triggering method is plotted on separate plots. Best-fit linear regression lines are plotted on each plot. If the pseudo-probabilistic or semi-probabilistic methods correlated perfectly with the PBEE methods the data would fall directly on the 1 to 1 line. However, a data trend line that falls above the 1 to 1 line indicates an over-prediction of settlement by the pseudo-probabilistic and semi-probabilistic methods and, conversely, when the data trend line plots below the 1 to 1 line pseudo-probabilistic and semi-probabilistic methods are under predicting settlement.

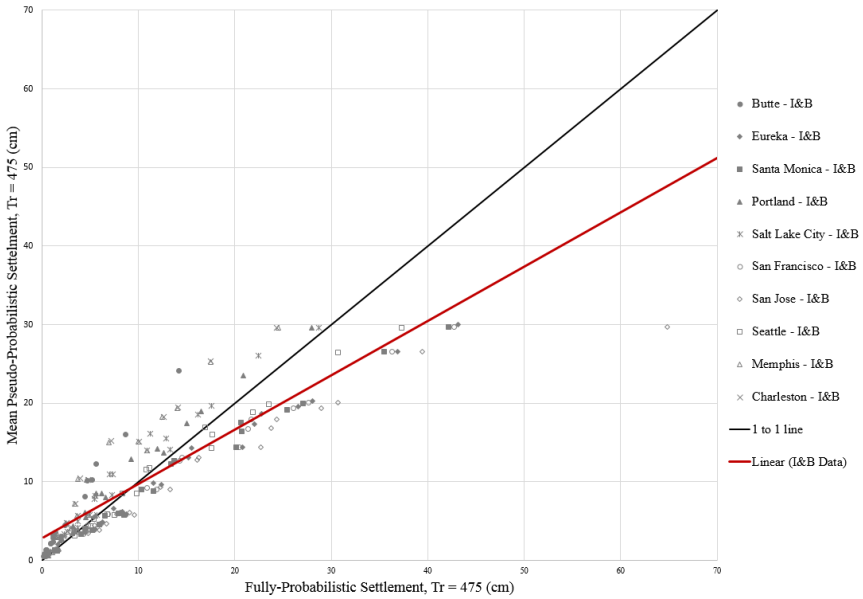

Figure 6-3: Idriss and Boulanger (2014) mean pseudo-probabilistic method compared to the PBEE procedure for the 475 year return period.

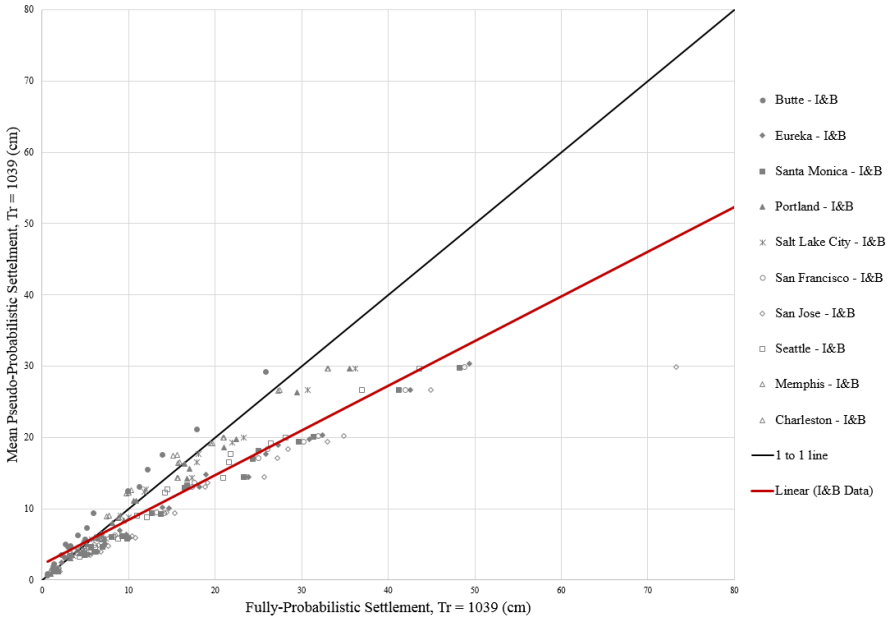

Figure 6-4: Idriss and Boulanger (2014) mean pseudo-probabilistic method compared to the PBEE procedure for the 1039 year return period.

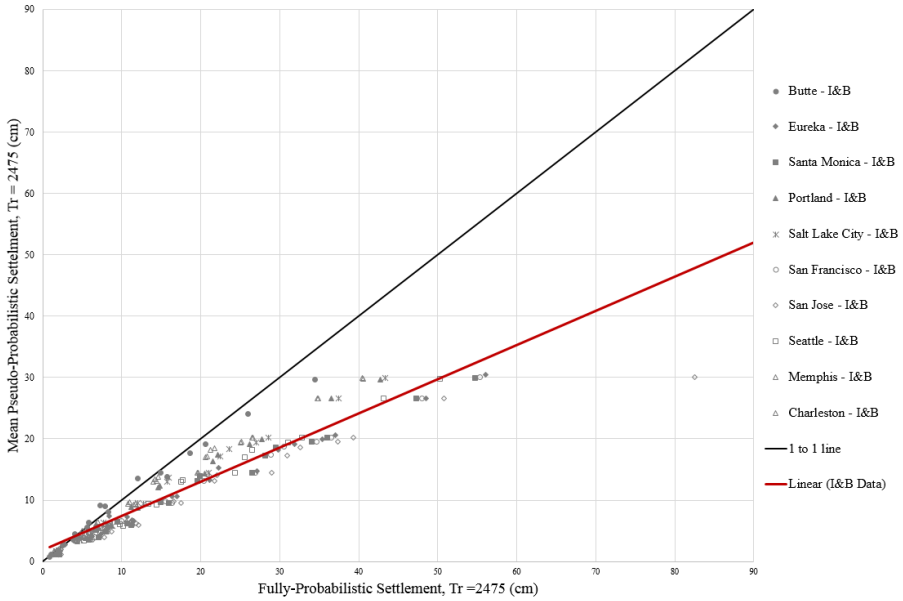

Figure 6-5: Idriss and Boulanger (2014) mean pseudo-probabilistic method compared to the PBEE procedure for the 2475 year return period.

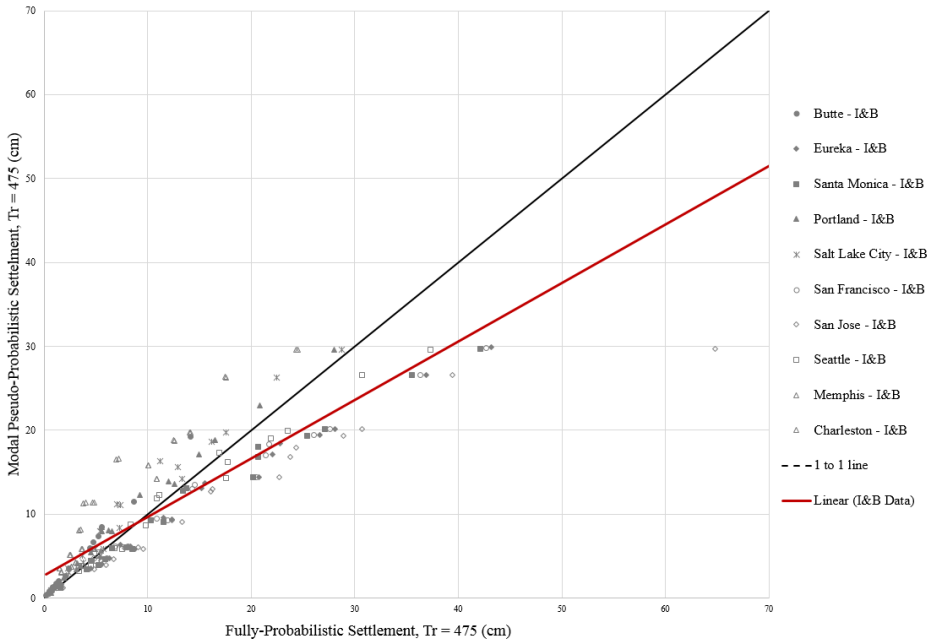

Figure 6-6: Idriss and Boulanger (2014) modal pseudo-probabilistic method compared to the PBEE procedure for the 475 year return period.

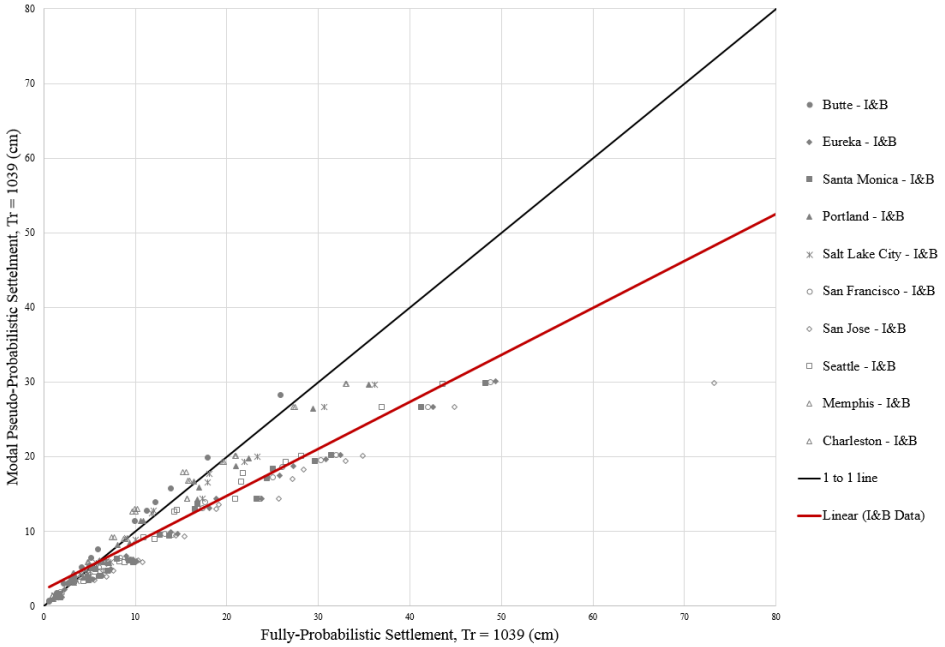

Figure 6-7: Idriss and Boulanger (2014) modal pseudo-probabilistic method compared to the PBEE procedure for the 1039 year return period.

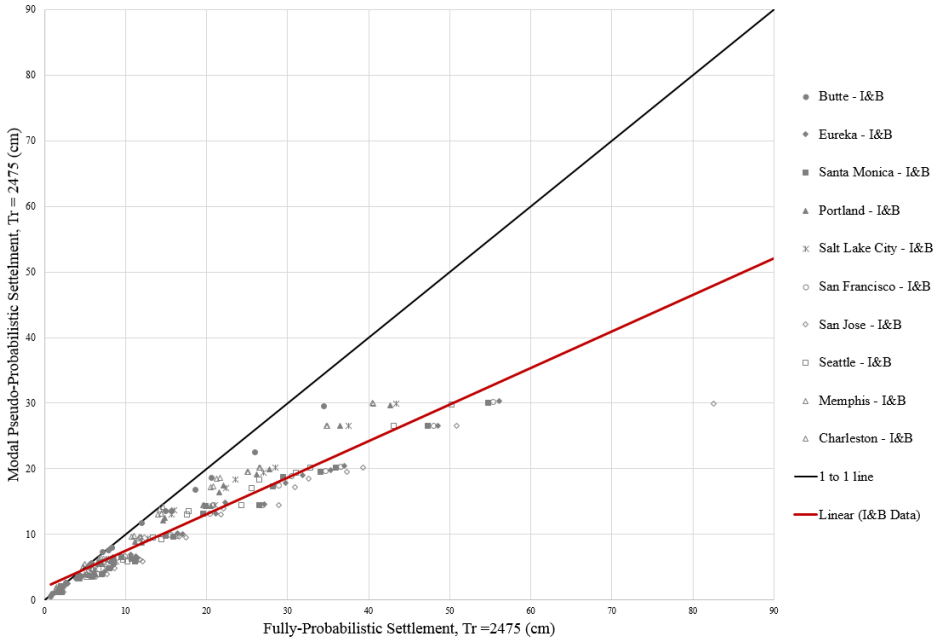

Figure 6-8: Idriss and Boulanger (2014) modal pseudo-probabilistic method compared to the PBEE procedure for the 2475 year return period.

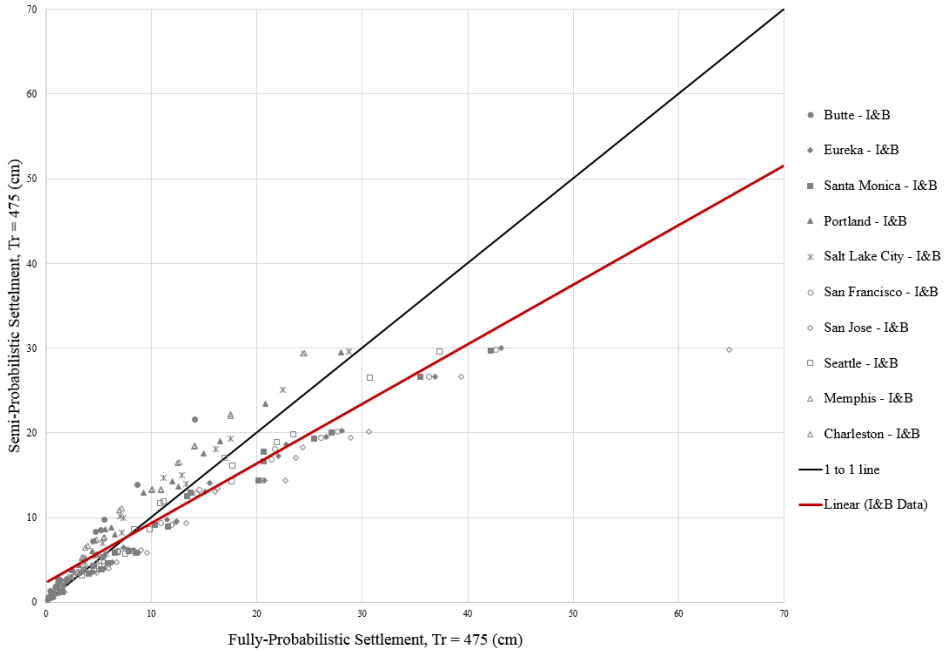

Figure 6-9: Idriss and Boulanger (2014) semi-probabilistic method compared to the PBEE procedure for the 475 year return period.

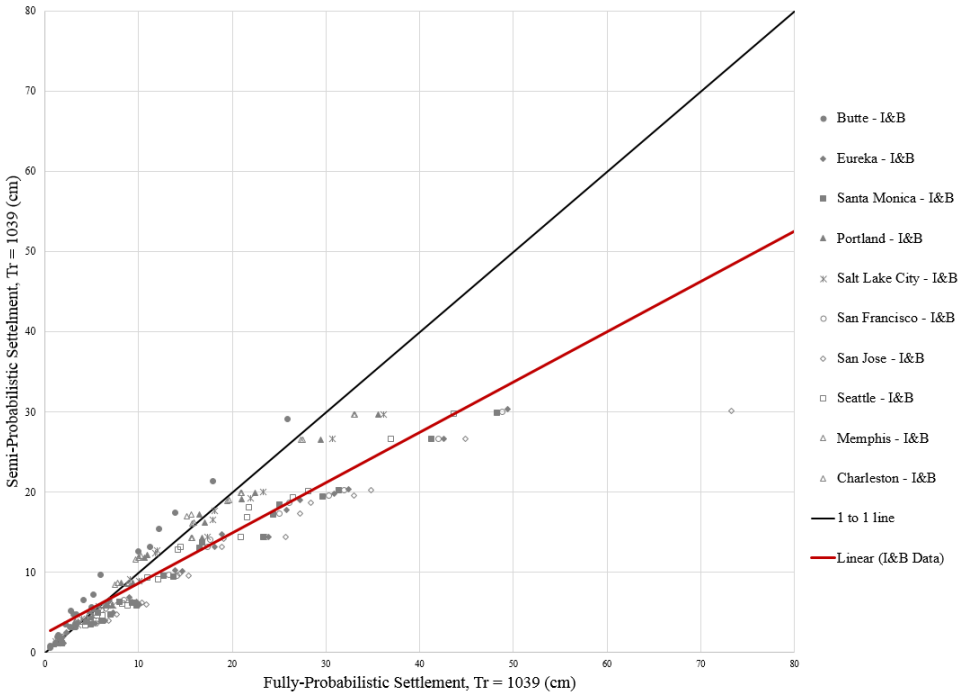

Figure 6-10: Idriss and Boulanger (2014) semi-probabilistic method compared to the PBEE procedure for the 1039 year return period

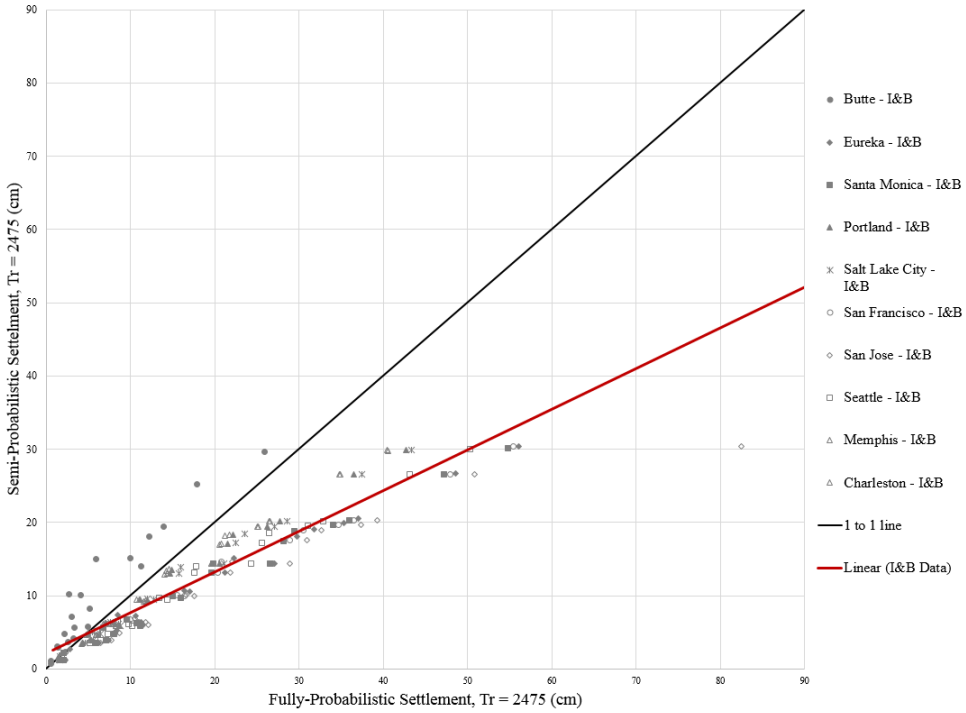

Figure 6-11: Idriss and Boulanger (2014) semi-probabilistic method compared to the PBEE procedure for the 2475 year return period

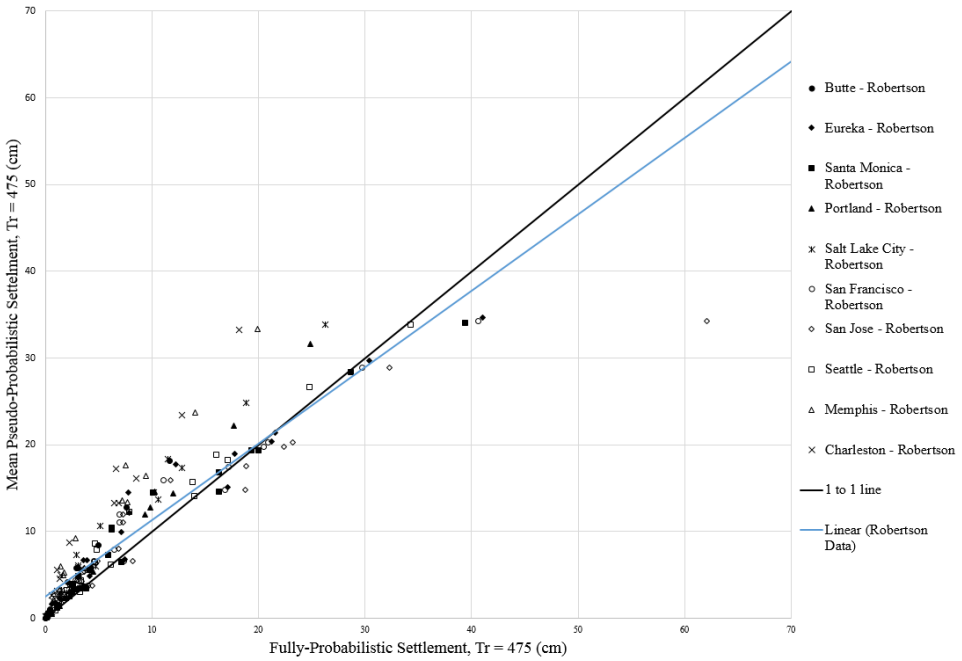

Figure 6-12: Robertson and Wride (2009) mean pseudo-probabilistic method compared to the PBEE procedure for the 475 year return period.

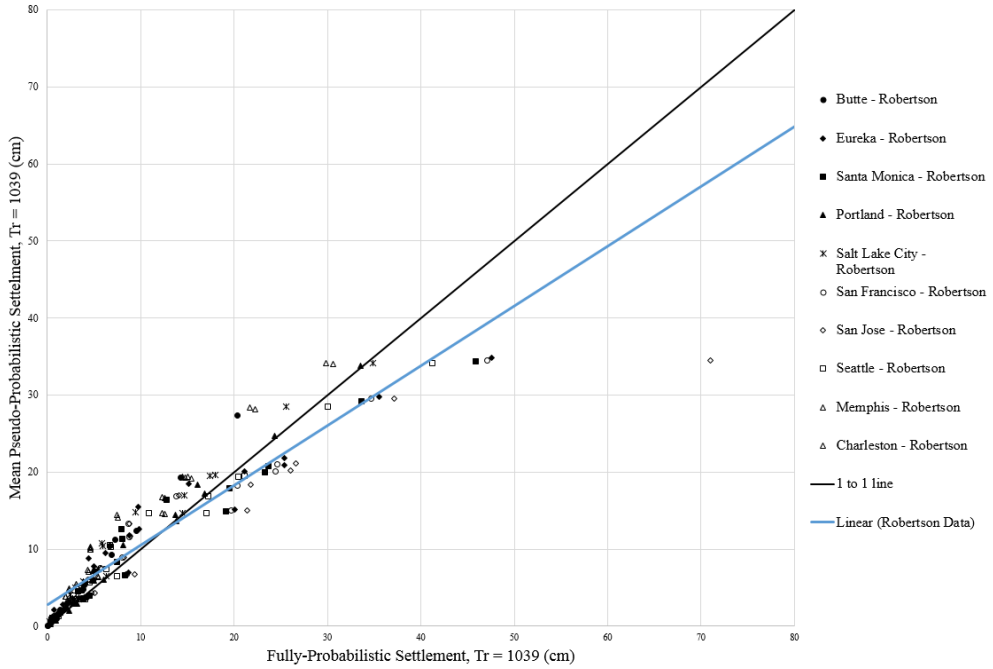

Figure 6-13: Robertson and Wride (2009) mean pseudo-probabilistic method compared to the PBEE procedure for the 1039 year return period.

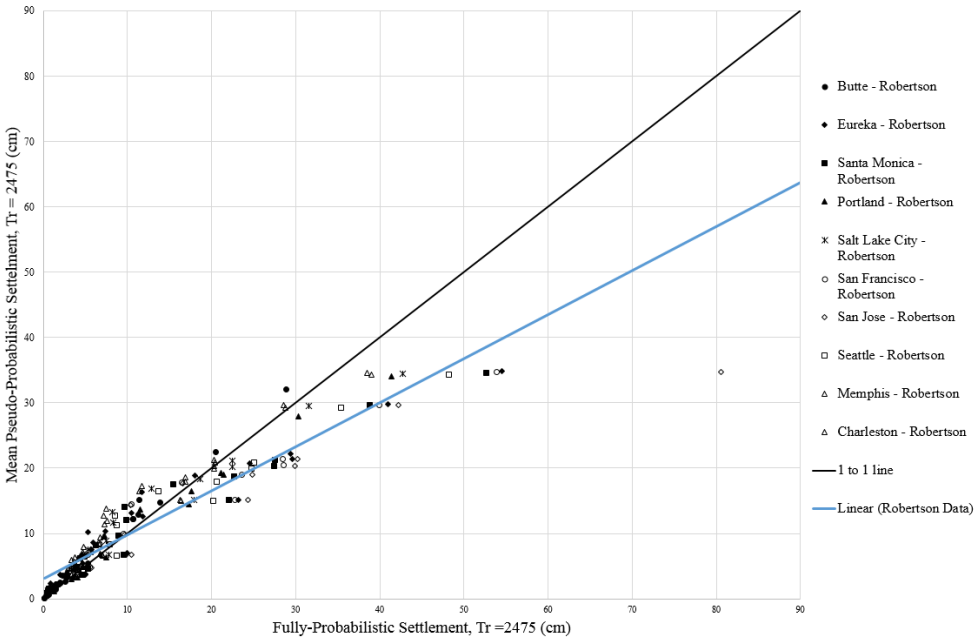

Figure 6-14: Robertson and Wride (2009) mean pseudo-probabilistic method compared to the PBEE procedure for the 2475 year return period.

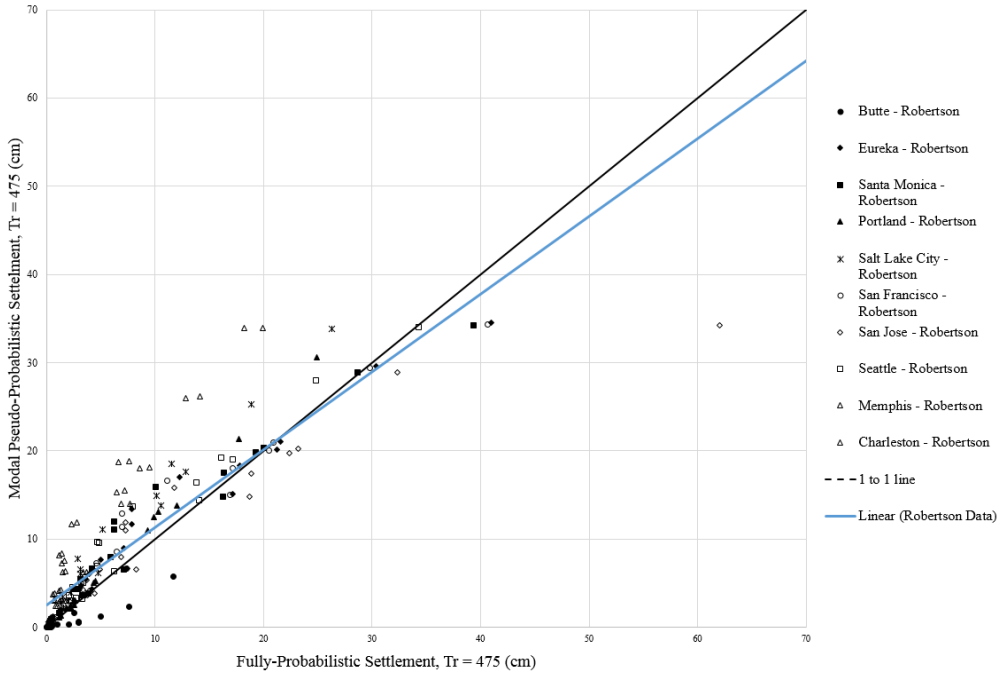

Figure 6-15: Robertson and Wride (2009) modal pseudo-probabilistic method compared to the PBEE procedure for the 475 year return period.

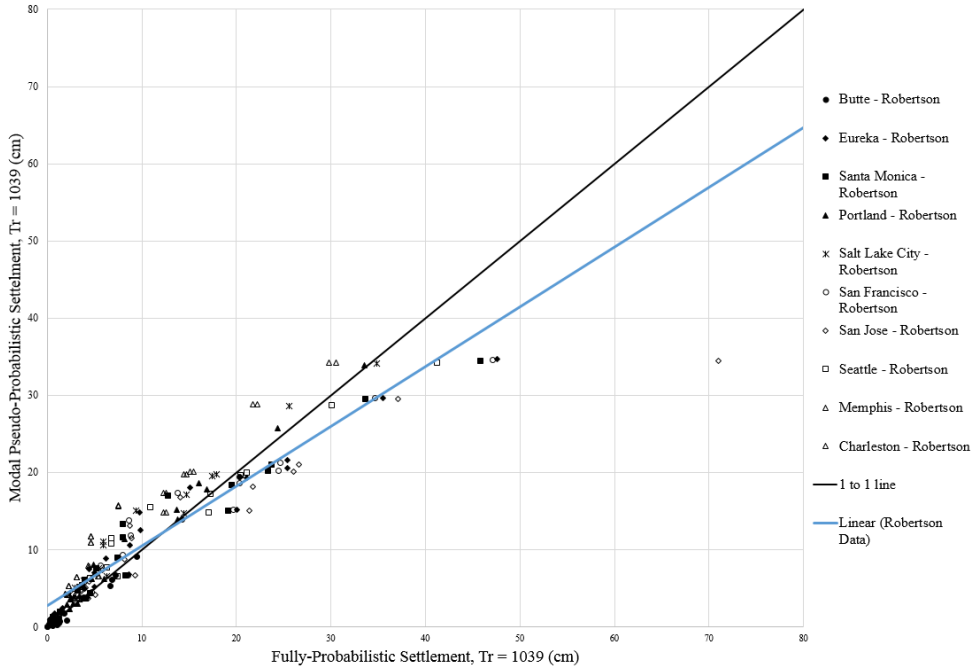

Figure 6-16: Robertson and Wride (2009) modal pseudo-probabilistic method compared to the PBEE procedure for the 1039 year return period.

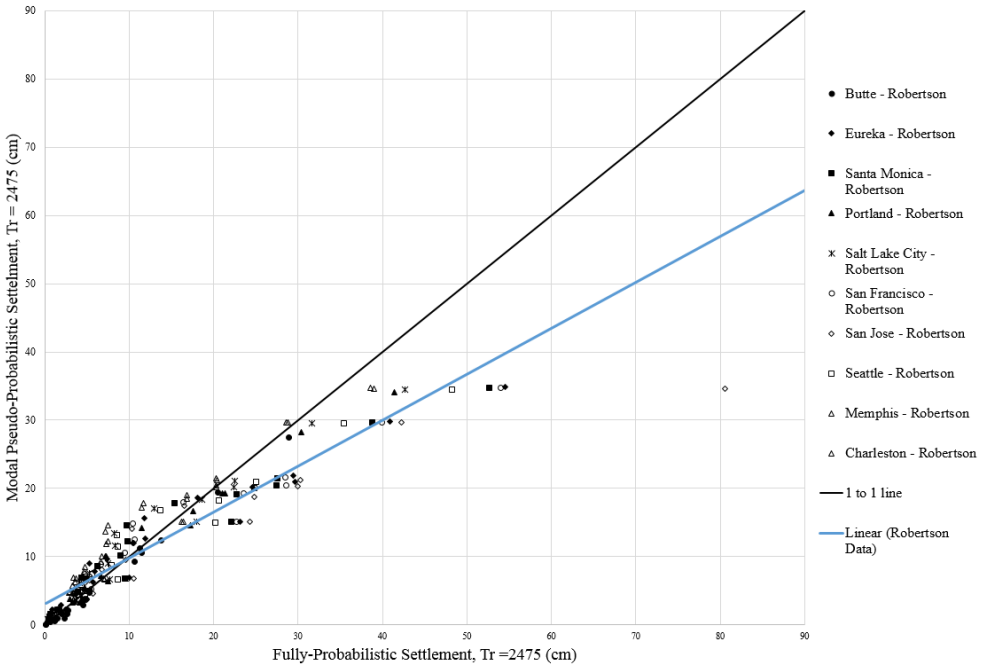

Figure 6-17: Robertson and Wride (2009) modal pseudo-probabilistic method compared to the PBEE procedure for the 2475 year return period.

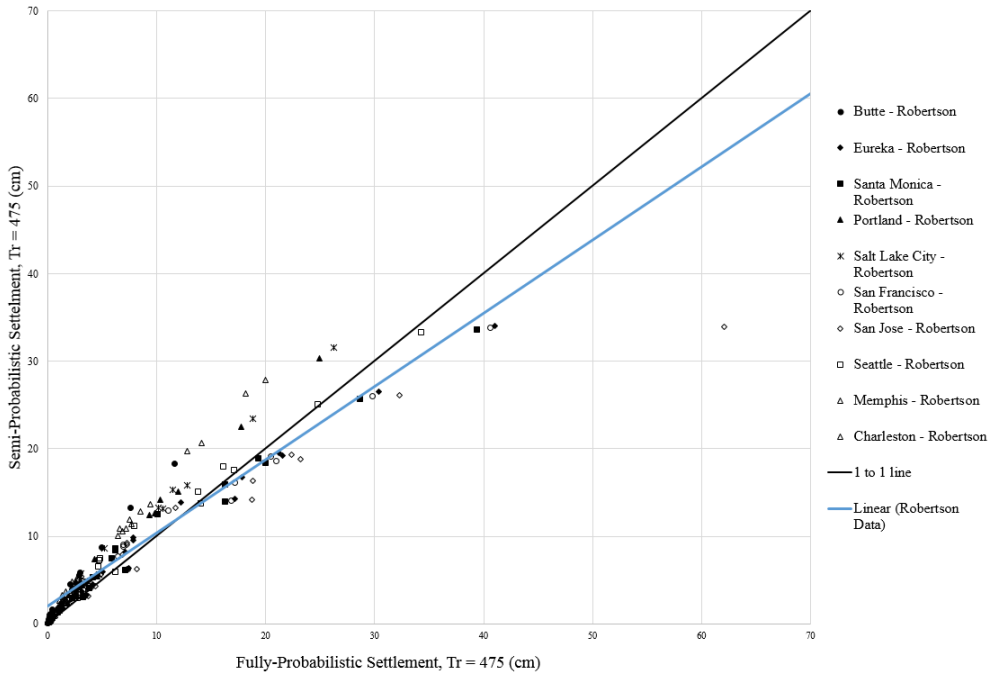

Figure 6-18: Robertson and Wride (2009) semi-probabilistic method compared to the PBEE procedure for the 475 year return period.

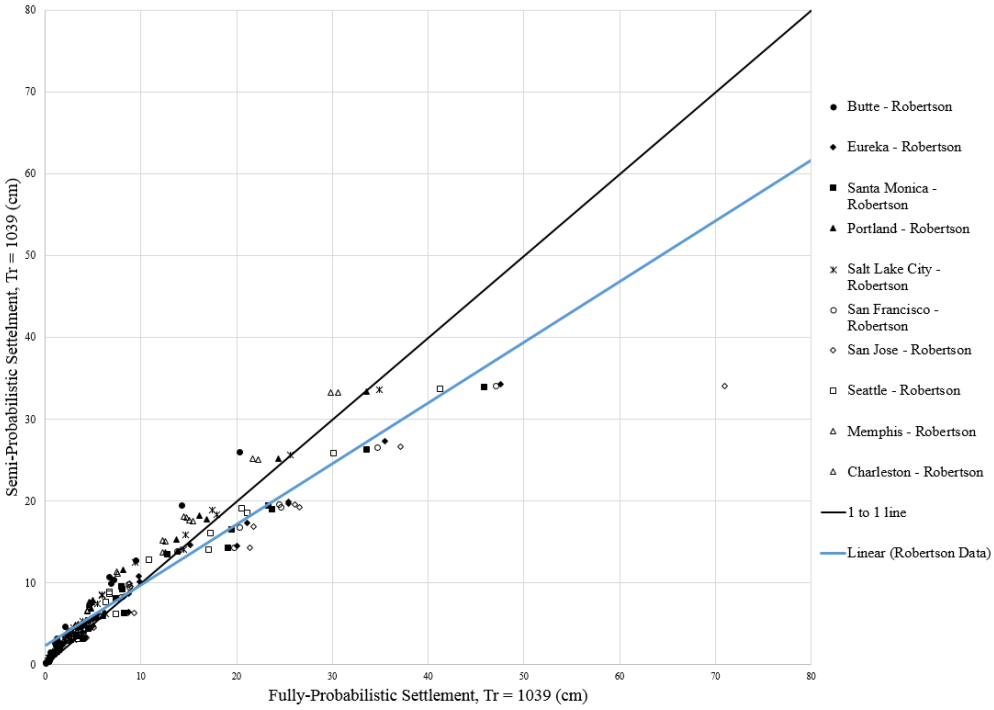

Figure 6-19: Robertson and Wride (2009) semi-probabilistic method compared to the PBEE procedure for the 1039 year return period.

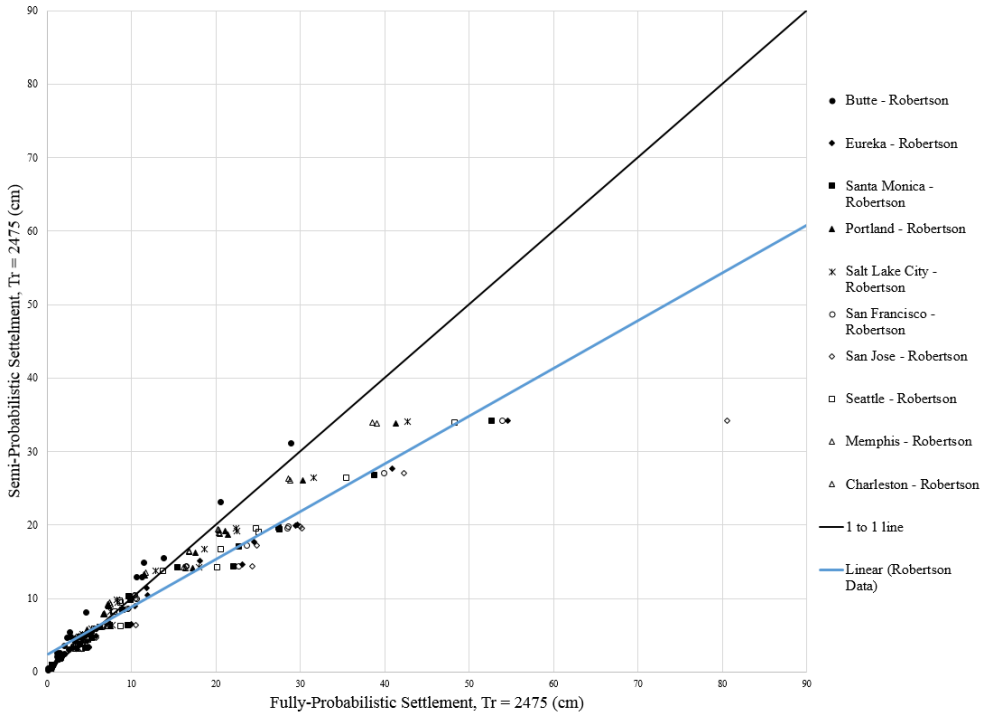

Figure 6-20: Robertson and Wride (2009) semi-probabilistic method compared to the PBEE procedure for the 2475 year return period.

The data trend lines tend to correlate with the one-to-one line fairly well up to a certain level of settlement for each return period when comparing the PBEE approach to the pseudo-probabilistic (mean magnitude) approach. The Robertson and Wride (2009) data, from the two settlement approaches, tend to match up well until about 20cm, 15cm, and 10cm of settlement for the 475 year, 1039 year, and 2475 year return periods, respectively. While the Boulanger and Idriss (2014) data, from the two settlement approaches, tend to line up fairly well until about 10cm, 5cm, and 3cm for the 475 year, 1039 year, and 2475 year return periods, respectively. The modal magnitude pseudo-probabilistic approach follows similar trends, but digress from the one-to-one line at lower values. The Robertson and Wride (2009) modal magnitude pseudo-probabilistic data lines up with the PBEE data fairly well until about 13cm, 10cm, and 6cm for the 475 year, 1039 year, and 2475 year return periods, respectively. While the Boulanger and

Idriss (2014) data averages line up fairly well until about 8cm, 6cm, and 5cm for the 475 year, 1039 year, and 2475 year return periods, respectively.

To further examine the source of the trends mentioned above, the settlement values computed from pseudo and semi-probabilistic methods, for the 1039 year and 2475 year return periods, were entered into the probabilistic hazard curve to back-calculate the actual return period associated with that settlement value. The results of this process are presented in Appendix B (Figures B-1 through B-20), but summarized as box and whisker plots in Figures 6-21 through 6-24.

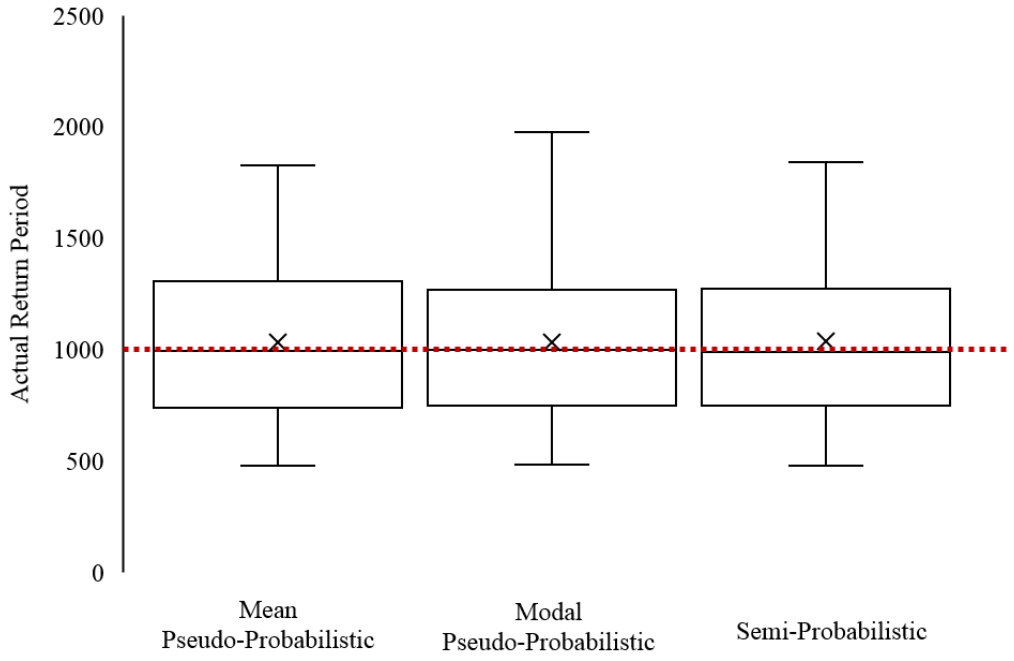

Figure 6-21: Box and whisker plots of actual return periods versus assumed 1039 year return period for the Idriss and Boulanger (2014) Triggering Method.

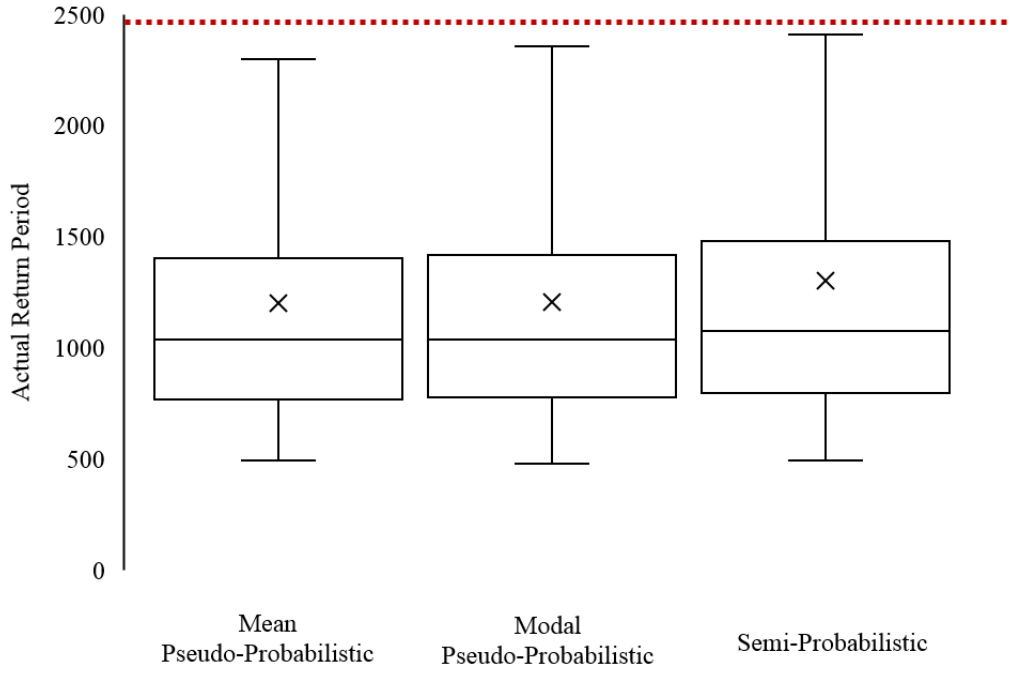

Figure 6-22: Box and whisker plots of actual return periods versus assumed 2475 year return period for the Idriss and Boulanger (2014) Triggering Method.

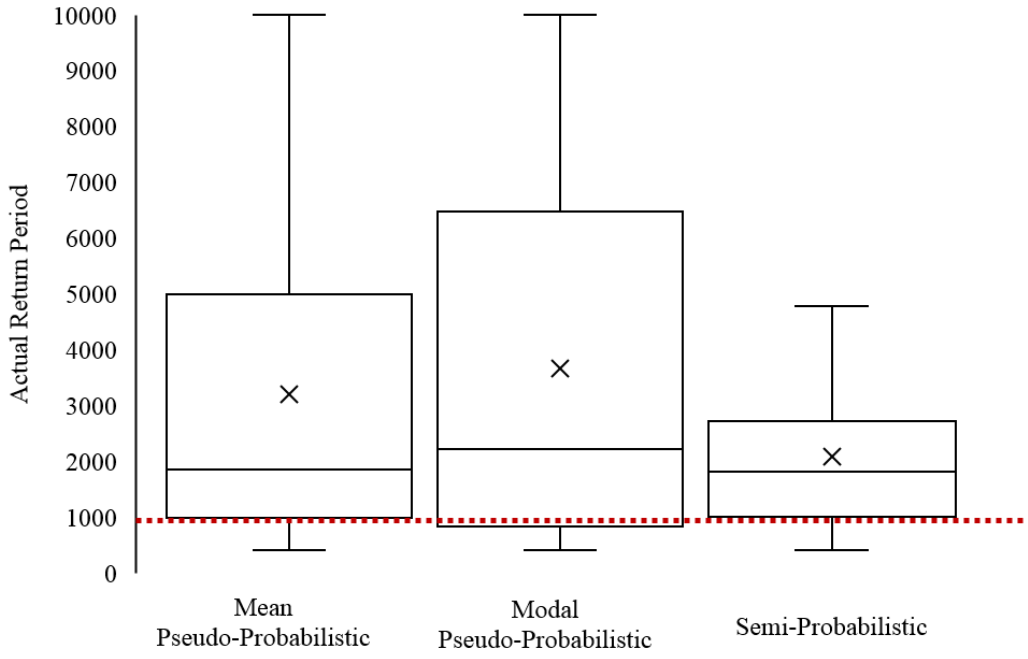

Figure 6-23: Box and whisker plots of actual return periods versus assumed 1039 year return period for the Robertson and Wride (2009) Triggering Method.

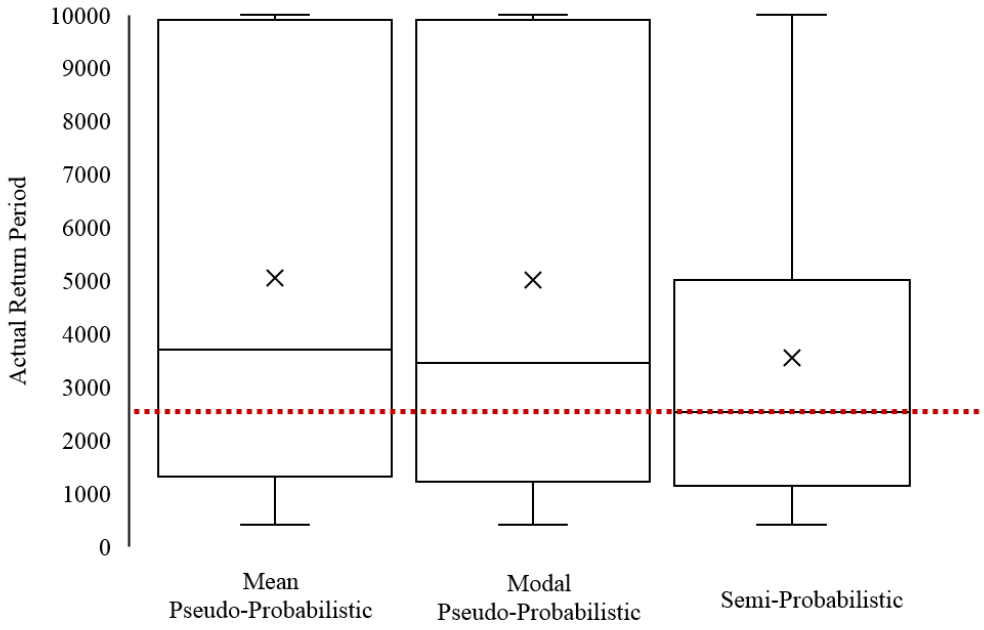

Figure 6-24: Box and whisker plots of actual return periods versus assumed 2475 year return period for the Robertson and Wride (2009) Triggering Method.

The box and whisker plots shown in Figures 6-21 through 6-24 illustrate the median, first and third quartiles, maximum and minimum values, and the average (marked by an "x") values of the return periods presented in the tables in Appendix B. As noted previously, these values represent actual return periods because they are generated from the fully-probabilistic settlement hazard curve. The assumed return period is presented as a red dashed line for reference.

The results for the 1039 return period (Figures 6-21 and 6-23) box plots seem to match the results from Figures 6-3 through 6-20 fairly well. The one-to-one plots and the box and whisker plots both indicated a fairly good match between approaches for the 1039 return period. The Idriss and Boulanger (2014) results for the 2475 return period (Figure 6-22) also line up with the results from the one-to-one plots, by indicating an under-prediction of post-liquefaction

settlements from conventional standards. The data suggests that 100% of the Idriss and Boulanger (2014) settlement calculations (using conventional methods) under predicted settlement compared to the PBEE settlement values.

The Robertson and Wride (2009) method also follows similar trends by under-predicting settlement more as the return period is increased. However, this method did not under predict settlements as much because it generated nearly vertical hazard curves for the stiffer soil profiles. For example, one of the hazard curves had 0.3cm of settlement at the 475 return period and only increased to 0.99cm of settlement by the 10,000 year return period. The steep slope of the hazard curve caused a back calculation of extremely high return periods. For example, if the pseudo-probabilistic methods produced 0.9cm of settlement, it would correlate to a return period of 9,500 years. The Robertson and Wride (2009) triggering method tended to produce these nearly vertical hazard curves for the stiffer soil profiles. However, for the more-liquefiable profiles, the Robertson and Wride (2009) method under-predicted settlement up to 84%. It was the steep hazard curves that caused the spikes in actual return periods calculated in the Robertson and Wride (2009) box and whisker plots (Figures 6-23 and 6-24). The Idriss and Boulanger (2014) procedure did not result in any of these steep hazard curves. This discrepancy is likely due to the different methods used to calculate the *CRR*. The data is suggesting that the Idriss and Boulanger (2014) procedure is conservatively indicating these stiffer soil profiles are more liquefiable than the Robertson and Wride (2009) indicates they are.

To examine the comparison, between conventional methods and the PBEE method, even further a heat map was generated (Figure 6-25). Each number in the map represents the number of CPT soundings, out of the total 20, in which the pseudo-probabilistic approach predicted less settlement than the PBEE approach. These values are presented for both triggering procedures,

each return period, and both magnitudes (mean and modal) at each city. The cities are ordered from the lowest a_{max} values to the highest from top down.

	Robertson & Wride (2009)						Idriss & Boulanger (2014)					
	475		1039		2475		475		1039		2475	
	Mean	Modal	Mean	Modal	Mean	Modal	Mean	Modal	Mean	Modal	Mean	Modal
Butte, MT	2	20	4	20	3	19	0	0	1	1	12	18
Portland, OR	2	8	7	3	11	11	0	0	18	15	20	20
Memphis, TN	0	0	0	0	4	4	0	0	9	7	19	18
Seattle, WA	3	1	8	7	9	9	15	13	20	20	20	20
Salt Lake City, UT	0	0	1	1	9	8	0	0	15	14	20	20
San Francisco, CA	7	6	9	9	9	9	20	19	20	20	20	20
Charleston, S.C.	0	0	0	0	4	3	0	0	10	9	18	18
Santa Monica, CA	6	3	9	9	9	9	20	19	20	20	20	19
San Jose, CA,	9	9	9	9	9	10	20	20	20	20	20	20
Eureka, CA	6	6	8	8	8	8	18	20	19	20	20	20

Figure 6-25: A heat map representing the number of CPT soundings, out of 20 soundings, in which the pseudo-probabilistic method under predicted settlement compared to the PBEE procedure.

The heat map reinforces the trends observed above. The heat map illustrates that the Idriss and Boulanger (2014) triggering procedure is under predicting settlement at a higher percentage than the Robertson and Wride (2009) method. This trend can also demonstrate how the Idriss and Boulanger (2014) method produces larger PBEE settlement values than the Robertson and Wride (2009) method. The heat map reinforces the trend indicating that the under prediction of settlement increases with an increasing level of site seismicity and return period. The Robertson and Wride (2009) has on about 50% of the soundings under predicting settlement at the 2475 year return period. While the Idriss and Boulanger (2014) procedure under predicted settlements for almost 90% of the CPT soundings at the 2475 return period.

The heat map points out 3 outliers at Butte, MT for the modal magnitude pseudo-probabilistic values where all 20 profiles under predicted settlement for all three return periods.

This discrepancy is likely due to a large difference in the MSF due to a significant difference in the mean and modal magnitudes at Butte, MT (Table 6-2). This discrepancy does not manifest in the Idriss and Boulanger (2014) procedure because of the differing MSF calculation methods (Equations 3-12 and 3-23). The Boulanger and Idriss (2014) procedure does depend solely on the magnitude to calculate the MSF like the Robertson and Wride (2009) method.

The results for the 475 return period at lower seismic areas are not surprising. At the 475 year return period pseudo-probabilistic method generally over-predicted or the methods predicted similar settlement values. This trend is logical because the pseudo-probabilistic procedure uses a deterministic method of predicting settlements. Deterministic methods are considered to be a conservative approach because it generally designs for the controlling scenario earthquake.

However, this idea is concerning after reviewing the results from the higher return periods. The data suggests, as the return period increased, the pseudo-probabilistic analyses under-predicted the level of liquefaction-induced settlement hazard by up to 90%. This trend is likely caused by the fact that the pseudo-probabilistic and semi-probabilistic methods compute post-liquefaction volumetric strains deterministically. Deterministic strain calculations ignore the inherent uncertainty associated with calculating strain values. The PBEE procedure, however, accounts for this uncertainty, resulting in higher settlement estimations.

Results from the semi-probabilistic approach had less scatter but underestimated settlements at about the same percentage as the pseudo-probabilistic approach. The trends depicted in the semi-probabilistic results are very similar to the trends from the pseudo-probabilistic results. These similarities in the two method's results suggests the uncertainty in the liquefaction triggering is less significant than the uncertainty in the strain calculations. These

results also prove the semi-probabilistic method is not an improvement to the current pseudo-probabilistic methods. Significant calculations are required to perform the calculations necessary for the semi-probabilistic approach and, therefore, may not be worth it for engineers to use this approach as a replacement to the pseudo-probabilistic approach. Engineers should either stick with the easier and equally accurate pseudo-probabilistic approach, or go all the way to the PBEE approach for more accuracy.

By comparing the results a comparison can be made between the Robertson and Wride (2009) and Boulanger and Idriss (2014) triggering methods. The two methods consistently predicted similar PBEE settlements for the varying CPT soundings and cities. However, the Boulanger and Idriss procedure consistently produced larger settlement values. This trend indicates the Boulanger and Idriss method is a more conservative option than the Robertson and Wride method.

6.2.4 Discussion

Pseudo-probabilistic methods are widely accepted in industry because they are considered to be a simple way to incorporate probabilistic ground motions into the liquefaction analysis and are often considered as a conservative design practice. If, in fact, these methods are under-predicting liquefaction-induced settlements, then relying on pseudo-probabilistic methods for design presents a dangerous risk. Engineers could be severely under predicting post-liquefaction settlements while believing their designs are conservatively over predicting settlement. This data suggests that pseudo-probabilistic design methods are a good option for areas of lower seismicity and lower return periods. However, according to this data, fully-

probabilistic methods should be used for regions of higher seismicity and when designing for medium to large seismic events.

It is these larger seismic events that are the most concerning to the financial and physical well-being of a region, because these events are capable of causing the most damaging and hazardous events. If engineered structures, for these high return period events, are designed for pseudo-probabilistic settlements it is likely they will be under-designed. These structures will be especially under designed if located in high seismic regions. This level of under prediction of settlement will likely lead to a large economic toll, should a seismic event occur.

It is important to note the scope limitations for this study. This study only focused on settlement and only one settlement estimation method (Ishihara and Yoshimine, 1992). Only two triggering methods (Robertson and Wride, 2009; Boulanger and Idriss, 2014) were applied to this settlement method. To confirm the results of this study, research should be performed to examine other seismic effects (e.g., lateral spread, bearing capacity, slope stability, etc.).

6.2.5 Correction Factor Sensitivity Analysis

In addition to the comparative study, a sensitivity analysis is performed. Four separate PBEE settlement calculations are performed for each city and CPT sounding to test the sensitivity of the PBEE procedure to the CPT correction factors presented in sections 4.3.2 through 4.3.4. These four calculations included a series termed the baseline (i.e., no corrections applied), a series with the depth weighting factor (Section 4.3.2), a series with the combined transition zone and thin layer correction (Sections 4.3.3 & 4.3.4), and a series with the transition zone, thin layer, and depth weighting factor corrections applied. All 20 soil profiles are analyzed for all cities and all three return periods for each of these series.

The resulting data is combined and is presented in box and whisker plots below (Figures 6-26 through 6-28). To create these box and whisker plots, a ratio (R) is created, which is presented as:

$$R = \frac{Settlement_{Series}}{Settlement_{Baseline}} \quad (6\text{-}1)$$

where $Settlement_{Series}$ represents the calculated PBEE settlement from one of the correction factor series described above and $Settlement_{Baseline}$ represents the calculated PBEE settlement from the baseline series. This means that if R is equal to 1, the specific correction factor had no impact on the settlement calculation. Therefore, the further away R is from 1, the more sensitive the probabilistic procedure is to that particular option.

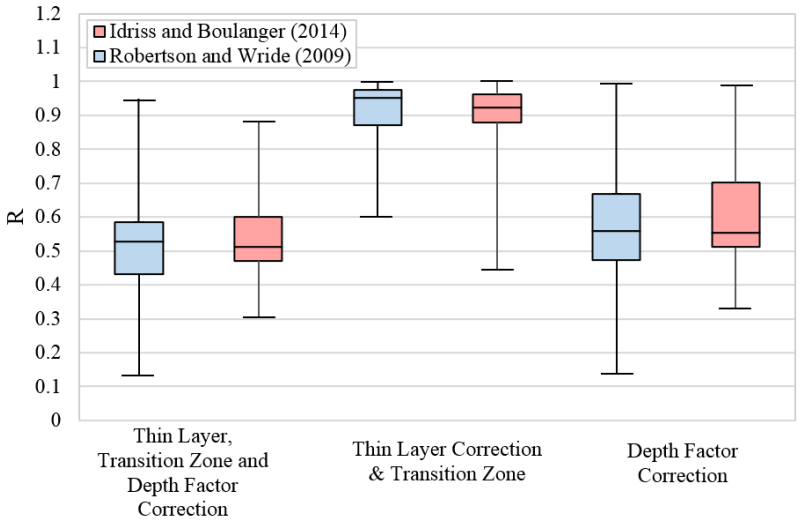

Figure 6-26: Box and whisker plots for R at a return period of 475 years.

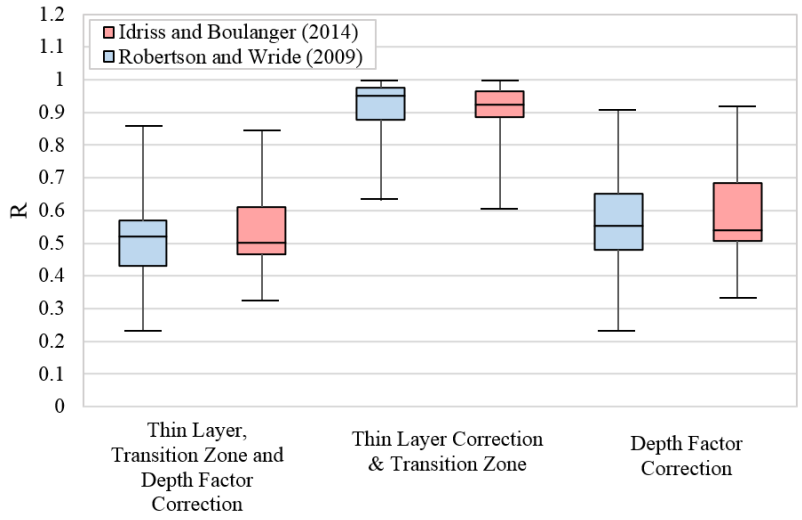

Figure 6-27: Box and whisker plots for *R* at a return period of 1039 years.

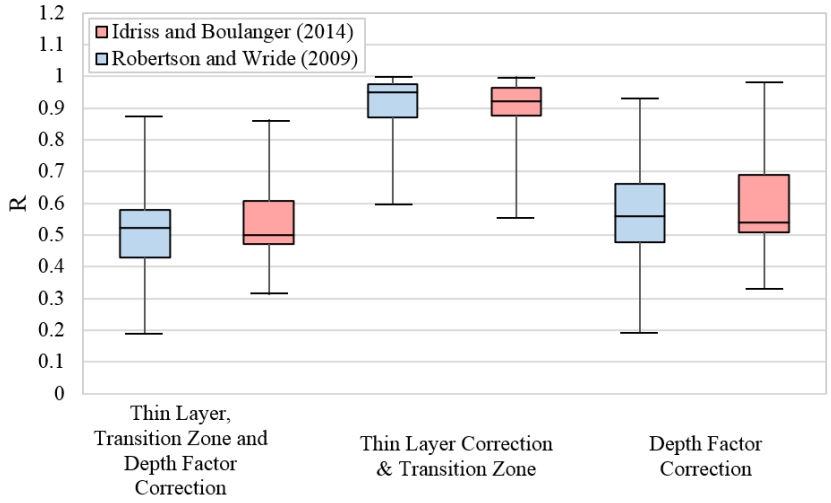

Figure 6-28: Box and Whisker plots for *R* at a return period of 2475 years.

The box and whisker plots show the impact each correction factor has on the full-probabilistic procedure. The box and whisker plots prove the importance and impact of correction factors. Based on the plots it's apparent the PBEE procedure is more sensitive to the depth weighting factor than the thin layer and transition zone correction factor. However, the

depth factor correction experienced a larger spread than the thin layer correction. It is logical that the thin layer and transition zone correction had a smaller impact on the calculated settlement values. For the thin layer correction to even be applied the soil profile needed to contain thin sand layers interbedded within soft clay layers. A few of the 20 profiles did not have this criteria and therefore did not experience any thin layer correction. However, because the depth weighting factor is independent of soil type, the depth weighting factor was always applied.

The data suggests that return period does not affect the sensitivity significantly. Across all three return periods, the median value and general trends are about the same. This is logical because the degree of sensitivity is dependent on soil type for thin layer correction and the depth factor correction will be constant because it is only dependent on depth. All of which are constant for each settlement calculation. It appears that *R* seemed to range between 0.45 and 0.6 for 68% of the data (+/- 1σ) regardless of the triggering model or the return period.

6.3 Chapter Summary

The PBEE (i.e., fully-probabilistic) liquefaction-induced settlement estimation procedure, presented in chapter 5, was tested using 20 different real CPT soundings, at 10 different seismic-level cities, and for three return periods (e.g., 475 year, 1039 year, and 2475 year). These results were compared to pseudo-probabilistic and semi-probabilistic values, calculated from the same CPT profiles and locations. For low return periods, the pseudo-probabilistic settlement values correlated fairly well with full-probabilistic settlement values. However, at higher return periods, this correlation deteriorated and showed pseudo-probabilistic methods under-predicting settlements significantly. The semi-probabilistic method followed similar trends to the pseudo-probabilistic method. Engineers should either stick with the easier and equally accurate pseudo-

probabilistic approach, or go all the way to the PBEE approach for more accuracy. The PBEE procedure was tested for its sensitivity to settlement correction factors. The PBEE procedure is more sensitive to the weighted depth factor correction than to the thin layer correction. This sensitivity remains pretty constant regardless of the triggering model or the return period.

7 SUMMARY AND CONCLUSIONS

Liquefaction is a phenomenon that occurs from cyclic loading from an earthquake. Liquefaction occurs when a saturated soil is loaded cyclically, which cause it to densify. Saturated soil densification causes the pore water to be squeezed out of the pore spaces, generating excess pore water pressure. This excess pore water pressure causes the soil particles to hydroplane on themselves resulting in zero effective stress, which is when liquefaction occurs.

Liquefaction can cause a many adverse effects, one of which is settlement. After a soil has liquefied, and the excess pore water starts to dissipate, soil particles tend to settle into a denser state, resulting in volumetric strains. These volumetric strains manifest themselves as ground surface settlements. Liquefaction-induced settlements are not directly life threatening, however they can cause extreme economic distress to an area because of the significant infrastructural damage they cause.

To design seismic resilient structures and infrastructure, engineers need to be able to predict seismic events, and their effects, accurately. Originally, engineers used a deterministic seismic hazard analysis (DHSA) to predict seismic hazards, by designing for the controlling earthquake. In the past 20 years engineers have relied on a pseudo-probabilistic seismic hazard analysis. This method uses a probabilistic seismic hazard analysis (PSHA) to choose a design earthquake, but

computes the likelihood of liquefaction triggering, and its effects, using deterministic calculation procedures.

Current research has found performance-based earthquake engineering (PBEE) procedures produce more accurate and consistent hazard estimates than the current pseudo-probabilistic methods (Kramer & Mayfield, 2007; Franke et al. 2014). The PBEE framework was proposed by the Pacific Earthquake Engineering Research (PEER) Center. PBEE applies a fully-probabilistic analysis into the prediction of seismic effects and presents these predictions in terms of levels of hazard. PBEE is extremely advantageous for not only predicting liquefaction and its effects, but also presenting these hazards in a way for all stakeholders to make more informed decisions. This study proposes a PBEE, fully-probabilistic, procedure to estimate post-liquefaction settlements for the CPT. This procedure incorporates the Ishihara and Yoshimine (1992) settlement method, by inputting the liquefaction triggering Robertson and Wride (1998, 2009) and Boulanger and Idriss (2014) methods, into the PEER framework.

A seismic hazard analysis tool, called *CPTLiquefY*, was developed to perform the full-probabilistic calculations. *CPTLiquefY* was developed within Microsoft Visual Studio, using Visual C++. The tool was developed by Mikayla Hatch, Tyler Coutu, and Alex Arndt, under the direction of Dr. Kevin Franke at Brigham Young University.

The calculated settlement values for the developed full-probabilistic procedure were compared to conventional analyses for 20 CPT profiles and 10 cities of varying levels of seismicity. It was observed that for a low return period, the pseudo-probabilistic settlement values correlated fairly well with full-probabilistic settlement values. At these low return periods and at cities of low seismicity the pseudo-probabilistic method over predicted settlements from about 5-50%. However, at higher return periods and cities with medium to high seismicity this

correlation deteriorated and showed pseudo-probabilistic methods under-predicting settlements significantly. In areas of high seismicity the pseudo-probabilistic procedure under predicted settlements up to 100%. The semi-probabilistic method followed similar trends to the pseudo-probabilistic method. These results suggest current design practices unintentionally ignore considerable amounts of risk when estimating liquefaction-induced settlements for earthquakes with higher return periods.

In addition to the comparative study, a sensitivity analysis was performed to test the effect of settlement correction factors on the PBEE estimation procedure. This analysis was performed for the thin layer correction and depth weighting factor correction. The results proved the fully-probabilistic procedure was more sensitive to the depth weighting factor than the thin layer correction. The study also proved the significance and importance of settlement calculation correction factors.

REFERENCES

Abrahamson, N., & Silva, W. (2008). Summary of the Abrahamson & Silva NGA Ground-Motion Relations. *Earthquake Spectra: February 2008, 24*(1), 67-97.

Ahmadi, M. M., & Robertson, P. K. (2005). Thin-layer effects on the CPT qc measurement. *Canadian Geotechnical Journal, 42*(5), 1302-1317.

Algermissen, S. T., Perkins, D. M., Thenhaus, P. C., Hanson, S. L., & Bender, B. L. (1982). Probabilistic estimates of maximum acceleration and velocity in rock in the contiguous United States. In U. S. G. Survey (Ed.), *Open-File Report 82-1033* (pp. 99). Washington, D.C.

Ambraseys, N. N. (1988). *Engineering Seismology* (Vol. 17).

Ancheta, T. D., Darragh, R. B., Stewart, J. P., Seyhan, E., Silva, W. J., Chiou, B. S.-J., . . . Donahue, J. L. (2014). NGA-West2 Database. *Earthquake Spectra:, 30*(3), 989-1005.

Arias, A. (1970). A measure of earthquake intensity. *Seismic Design for Nuclear Power Plants,* 438-483.

Ben-Menachem, A. (1961). Radiation Patterns of seismic surface waves from finite moving sources. *Bulletin of the Seismological Society of America, 51*, 401-435.

Benioff, H. (1955). *Mechanism and strain characteristics of the White Wolf fault as indicated by the aftershock sequence*: California Division of Mines, Bulletin 171.

Benjamin, J. R., & Associates. (1988). A criterion for determining exceedance of the Operating Basis Earthquake. In E. P. R. Institute (Ed.), *EPRI Report NP-5930*. Palo Alto, California.

Bolt, B. A. (1969). *Duration of strong motion.* Paper presented at the 4th World Conference on Earthquake Engineering, Santiago, Chile.

Boore, D. M., & Atkinson, G. M. (2008). Ground-Motion Prediction Equations for the Average Horizontal Component of PGA, PGV, and 5%-Damped PSA at Special Periods between 0.01 s and 10.0 s. *Earthquake Spectra: February 2008, 24*(1), 99-138.

Boore, D. M., Joyner, W. B., & Fumal, T. E. (1993). Estimation of response spectra and peak accelerations from western North America earthquakes: An interim report. In U. S. G. Survey (Ed.), *Open-File-Report 93-509*.

Boulanger, R., & Idriss, I. (2014). CPT and SPT based liquefaction triggering procedures. *Center for Geotechnical Modeling, Department of Civil and Environmental Engineering, University of California, Davis, CA. Report No. UCD/CGM-14/01*.

Boulanger, R. W., & Idriss, I. M. (2005). *New criteria for distinguishing between silts and clays that are susceptible to liquefaction versus cyclic failure.* Paper presented at the Technologies to Enhance Dam Safety and the Environment, 25th Annual United States Society on Dams, USSD, Denver.

Bray, J. D., & Dashti, S. (2014) Liquefaction -induced building movements. *Vol. 3. Bulletin of Earthquake Engineering* (pp. 1129-1156).

Cambell, K. W. (1981). Near source of peak horizontal acceleration. *Bulletin of the Seismological Society of America, 71*, 2039-2070.

Cambell, K. W., & Bozorgnia, Y. (1994). *Near-source attenuation of peak acceleration from worldwide accelerograms recorded from 1957 to 1993.* Paper presented at the 5th U.S. National Conference on Earthquake Engineering, Earthquake Engineering Research Institute, Berkeley, California.

Cambell, K. W., & Bozorgnia, Y. (2008). NGA Ground Motion Model for the Geometric Mean Horizontal Component of PGA, PGV, PGD, and 5% Damped Linear Elastic Response Spectra for Periods Ranging from 0.01 to 10 s. *Earthquake Spectra: February 2008, 24*(1), 139-171.

Casagrande, A. (1936). Characteristics of cohesionless soils affecting the stability of slopes and earth fills. *Journal of the Boston Society of Civil Engineers*.

Castro, G. (1969). Liquefaction of sands. *Harvard Soil Mechanics Series 87*.

Cetin, K., Bilge, H., Wu, J., Kammerer, A., & Seed, R. (2009). Probabilistic Model for the Assessment of Cyclically Induced Reconsolidation (Volumetric) Settlements. *Journal of Geotechnical and Geoenvironmental Engineering, 3*(135), 387-393.

Chiou, B. S.-J., & Youngs, R. R. (2008). A NGA Model for the Average Horizontal Component of Peak Ground Motion and Response Spectra. *Earthquake Spectra: February 2008, 24*(1), 173-215.

Cornell. (1968). Engineering seismic risk analysis. *Bulletin of the Seismological Society of America, 58*, 1583-1606.

Cornell, C. A., & Krawinkler, H. (2000). Progress and challenges in seismic performance assessment. *PEER Center News, 3*(2), 1-3.

Dashti, S., Bray, J. D., Pestana, J. M., Riemer, M., & Wilson, D. (2010). Mechanisms of Seismically Induced Settlement of Buildings with Shallow Foundations on Liquefiable Soil. *Journal of Geotechnical and Geoenvironmental Engineering, 135*(1).

Deierlein, G., Krawinkler, H., & Cornell, C. (2003). *A framework for performance-based earthquake engineering.* Paper presented at the Pacific conference on earthquake engineering.

Dobry, R., & Vucetic, M. (1987). *Dynamic properties and seismic response of soft clay deposits.* Paper presented at the International Symposium on Geotechnical Engineering of Soft Soils, Mexico City.

Elkstrom, L. T. (2015). A Simplified Performance-Based Procedure for the Prediction of Lateral Spread Displacements.

Franke, K. W., Wright, A. D., & Hatch, C. K. (2014). *PBLiquefY: A New Analysis tool for the performance-based evaluation of liquefaction triggering.* Paper presented at the 10th National Conference on Earthquake Engineering.

Friedman, D. (2007). How to Detect, Diagnose, & Evaluate Earthquake Damage. from inspect-ny.com

G. Castro, S. J. P. (1977). Factors affecting liquefaction and cyclic loading. *Journal of the Geotechnical Engineering Division, 106*(GT6), 501-506.

Golesorkhi, R. (1989). *Factors Influencing the Computational Determination of Earthquake-Induced Shear Stress in Sandy Soils.* (Ph.D.), University of California at Berkeley.

Hanks, T. C., & Kanamori, H. (1979). A moment magnitude scale. *Journal of Geophysical Research, 84*, 2348-2350.

Hanzawa, H., Itoh, Y., & Suzuki, K. (1979). Shear characteristics of a quick sand in the Arabian Gulf. *SOILS AND FOUNDATIONS, 19*(4), 1-15.

Housner, G. W. (1959). Behavior of structures during earthquakes. *Journal of the Engineering Mechanics Division, 85*(EM14), 109-129.

Huang, Y. M. (2008). *Performance-based design and evaluation for liquefaction-related seismic hazards.* (Ph.D. Dissertation), University of Washington, Seattle, WA.

Idriss, I. M. (2008). An NGA Empirical Model for Estimating the Horizontal Spectral Values Generated By Shallow Crustal Earthquakes. *Earthquake Spectra: February 2008, 24*(1), 217-242.

Idriss, I. M., & Boulanger, R. W. (2008). *Soil Liquefaction During Earthquakes*.

Ishihara, K. (1984). *Post-Earthquake Failure of Tailings Dam due to Liquefaction of the Pond Deposit.* Paper presented at the Int. Conference on Case Histories in Geotechnical Engineering, St. Louis, Missouri.

Ishihara, K. (1985). *Stability of natural deposits during earthquakes.* Paper presented at the 11th International Conference on Soil Mechanics and Foundation Engineering.

Ishihara, K., & Yoshimine, M. (1992). Evaluation of settlements in sand deposits following liquefaction during earthquakes. *SOILS AND FOUNDATIONS, 32*(1), 173-188. doi: 10.3208/sandf1972.32.173

Iwasaki, T., Tokida, K., Tatsuka, F., Wantabe, S., Yasuda, S., & Sato, H. (1982). *Miccrozonation for soil liquefaction potential using the simplified methods.* Paper presented at the 3rd International Conference on Microzonation, Seattle.

Jefferies, M. G., & Davies, M. P. (1993). Use of CPTU to estimate equivalent SPT N60. *Geotechnical Testing Journal, 16*(4).

Jennings, P. C. (1985). *Ground motion parameters that influence structural damage*. Berkeley, California: Earthquake Engineering Institute.

Jibson, R. (1987). Summary of research on the effects of topographic amplification of earthquake shaking on slope stability *Open-File Report 87-268*. Melano Park, California: U.S. Geologic Survey.

Joyner, W. B., & Boore, D. M. (1988). Measurement, characterization, and prediction of strong ground motion. *Earthquake Engineering and Soil Dynamics II - Recent Advances in Ground-Motion Evaluation,* 43-102.

Juang, C. H., Ching, J., Wang, L., Khoshnevisan, S., & Ku, C.-S. (2013). Simplified procedure for estimation of liquefaction-induced settlement and site-specific probabilistic settlement exceedance curve using cone penetration test (CPT). *Canadian Geotechnical Journal, 50*(10), 1055-1066.

K. Been, M. G. J. (1985). A state parameter for sands. *Geotechnique, 35*(2), 99-112.

Kanamori, H. (1977). The Energy Release in Great Earthquakes. *Journal of Geophysical Research, 82*, 2981-2987.

Kanamori, H. (1983). Magnitude scale and quantification of earthquakes. *Tectonophysics, 93*, 185-199.

Kramer, S. L. (1996). *Geotechnical Earthquake Engineering*. Upper Saddle River, NJ: Prentice Hall, Inc.

Kramer, S. L. (2008). Evaluation of liquefaction hazards in Washington State *WSDOT Report WA-RD* (Vol. 668.1, pp. 152).

Kramer, S. L., & Mayfield, R. T. (2007). Return period of soil liquefaction. *Journal of Geotechnical and Geoenvironmental Engineering, 133*(7), 802-813.

Lade, P. V. (1992). Static instability and liquefaction of loose fine sandy slopes. *Journal of Geotechnical Engineering, 118*(1), 51-71.

Lee, K., & Albaisa, A. (1974). Earthquake induced settlements in saturated sands. *Journal of ASCE, 103*(GT6), 565-588.

Liao, S. S. C., & Whitman, R. V. (1986). Overburden Correction Factors for SPT in Sand. *Journal of Geotechnical Engineering, ASCE, 112*(3).

Middlebrooks, T. A. (1942). For Peck Slide. *ASCE, 107*, 723-764.

Moehle, J., & Deierlein, G. G. (2004). *A framework methodology for performance-based earthquake engineering.* Paper presented at the 13th World Conference on Earthquake Engineering, Vancouver B.C., Canada.

Mogami, T., & Kubo, K. (1953). The behaviour of soil during vibration. *Proceedings, 3rd International Conference on Soil Mechanics and Foundation Engineering, Zurich, 1*.

Mohamad, R., & Dobry, R. (1986). Undrained monotonic and cyclic triaxial strength of sand. *Journal of Geotechnical Engineering, 112*(10), 941-958.

Nadgouda, K. (2007). Earthquake in Japan. *Geotechnical Engineering 101 and more.* 2017, from https://kshitija.wordpress.com/category/information/

Nagase, H., & Ishihara, K. (1988). Liquefaction-induced compaction and settlement of sand during earthquakes. *SOILS AND FOUNDATIONS, 28*(1), 66-76.

Peterson, B. D. (2016). *Development of a Performance-Based Procedure for Assessment of Liquefaction-Induced Free-Field Settlements.* (Master of Science), Brigham Young University, Provo, UT.

Peterson, M. D., Moschetti, M. P., Powers, P. M., Mueller, C. S., Haller, C. M., Frankel, A. D., & Field, N. (2015). The 2014 United States national seismic hazard model. *Earthquake Spectra, 31*(S1).

Porter, K. A. (2003). *An Overview of PEER's Performance-Based Earthquake Engineering Methodology.* Paper presented at the Ninth International Conference on Applications of Statistics and Probability in Civil Engineering.

Poulos, S. J. (1981). The steady state of deformation. *Journal of Geotechnical Engineering Division, 107*(GT5), 553-562.

Reiter, L. (1990). *Earthquake Hazard Analysis - Issues and Insights*. New York: Columbia University Press.

Richter, C. F. (1935). An instrumental earthquake scale. *Bulletin of the Seismological Society of America, 25*, 1-32.

Robertson, P. (2009). *Performance based earthquake design using the CPT.* Paper presented at the Proceedings of IS-Tokyo 2009: international conference on performance-based design in earthquake geotechnical engineering—from case history to practice, Tokyo, Japan.

Robertson, P. (2011). Computing in Geotechnical Engineering-Automatic Software Detection of CPT Transition Zones. *Geotechnical News, 29*(2), 33.

Robertson, P., & Wride, C. (1998). Evaluating cyclic liquefaction potential using the cone penetration test. *Canadian Geotechnical Journal, 35*(3), 442-459.

Robertson, P. K. (1990). Soil classification using the cone penetration test. *Canadian Geotechnical Journal, 27*.

Roscoe, K. H., & Pooroshab, H. B. (1963). *A fundamental principle of similarity in model tests for earth pressure problems.* Paper presented at the 2nd Asian Regional Conference on Soil Mechanics, Tokyo.

Seed, H. B., & Idriss, I. M. (1971). Simplified procedure for evaluating soil liquefaction potential. *Journal of Soil Mechanics & Foundations Div*.

Seed, H. B., & Idriss, I. M. (1982). Ground Motions and Soil Liquefaction During Earthquakes. *EERI,* 134.

Shamoto, Y., Zhang, J. M., & Tokimatsu, K. (1998). Methods for evaluating residual post-liquefaction ground settlement and horizontal displacement. *SOILS AND FOUNDATIONS, 2*(2), 69-83.

Singh, J. P. (1985). Earthquake ground motions: Implications for designing structures and reconciling structural damage. *Earthquake Spectra, 1*(2), 239-270.

Tatsuoka, F., Sasaki, T., & Yamada, S. (1984). *Settlement in Saturated sand induced by cyclic undrained simple shear*. Paper presented at the Eighth World Conference on Earthquake Engineering, San Francisco.

Tatsuoka, F., Zhou, S., Sato, T., & Shibuya, S. (1990). Evaluation method of liquefaction potential and its application. *Report on seismic hazards on the ground in urban areas. Ministry of Education of Japan, Tokyo*, 75-109.

Tentative provisions for the development of seismic regulations for buildings. (1978). Applied Technology Council.

Thun, J. L. V., Rochim, L. H., Scott, G. A., & Wilson, J. A. (1988). Earthquake ground motions for design and analysis of dams. *Earthquake Engineering and Soil Dynamics II - Recent Advance in Ground-Motion Evaluation,* 463-481.

Tokimatsu, K., & Seed, H. (1987). Evaluation of Settlements in Sands Due to Earthquake Shaking. *Journal of Geotechnical Engineering, 113*(8), 861-878.

Toro, G. R., Abrahamson, N. A., & Schneider, J. F. (1995). Engineering model of strong ground motions from earthquakes in the central and eastern United States. *Earthquake Spectra*.

Treadwell, D. D. (1976). *The influence of gravity, prestress, compressibility, and layering on soil resistance to static penetration.* (PhD), Cambridge University.

U.S.G.S. Earthquake Hazards Program. *Table of CPT Data, All Regions.* Retrieved March, 2017, from https://earthquake.usgs.gov/research/cpt/data/table/

Ulmer, K. J. (2015). Development of a Simplified Performance-Based Procedure for Assessment of Liquefaction Triggering Using Liquefaction Loading Maps.

Vaid, Y. P., & Chern, J. C. (1983). Effect of static shear on resistance of liquefaction. *SOILS AND FOUNDATIONS, 23*(1), 47-60.

Vidale, J. E., & Helmberger, D. V. (1988). Elastic finite difference of the 1971 San Fernando earthquake. *Bulletin of the Seismological Society of America, 78*(1), 122-141.

Williams, L., & Lopez, G. (2015). At Least 4,400 dead after devastating 7.8-Magnitude earthquake strikes Nepal. *Vox.* Retrieved 2017, from https://www.vox.com/2015/4/25/8495927/nepal-earthquake-magnitude-devastation

Wu, J., & Seed, R. B. (2004). *Estimation of liquefaction-induced ground settlement (case studies).* Paper presented at the 5th International Conference on Case Histories in Geotechnical Engineering, New York.

Youd, L. (2001). Liquefaction Resistance of Soils: Summary Report from the 1996 NCEER and 1998/NSF Workshops on Evaluation of Liquefaction Resistance of Soils. *Journal of Geotechnical and Geoenvironmental Engineering, 127*(4).

Youd, T. L. (1984). *Recurrence of liquefaction at the same site.* Paper presented at the 8th World Conference on Earthquake Engineering.

Youd, T. L. (1991). *Mapping of earthquake-induced liquefaction for seismic zonation.* Paper presented at the 4th International Conference on Seismic Zonation, Stanford University.

Youd, T. L., & Hoose, S. N. (1977). *Liquefaction susceptibility and geologic setting.* Paper presented at the 6th World Conference on Earthquake Engineering, Englewood Cliffs, N.J.

Youngs, R. R., Day, S. M., & Stevens, J. L. (1988). *Near field ground motions on rock for large subduction earthquakes.* Paper presented at the Earthquake Engineering and Soil Dynamics II: Recent Advances in Ground Motion Evaluation, New York.

APPENDIX A: CPTLIQUEFY TUTORIAL

CPTLiquefY is designed to be user friendly, but to ensure anyone can use the program a tutorial is provided. When the program is started a title page will appear. To start, the user can navigate to the "Soil Info" tab.

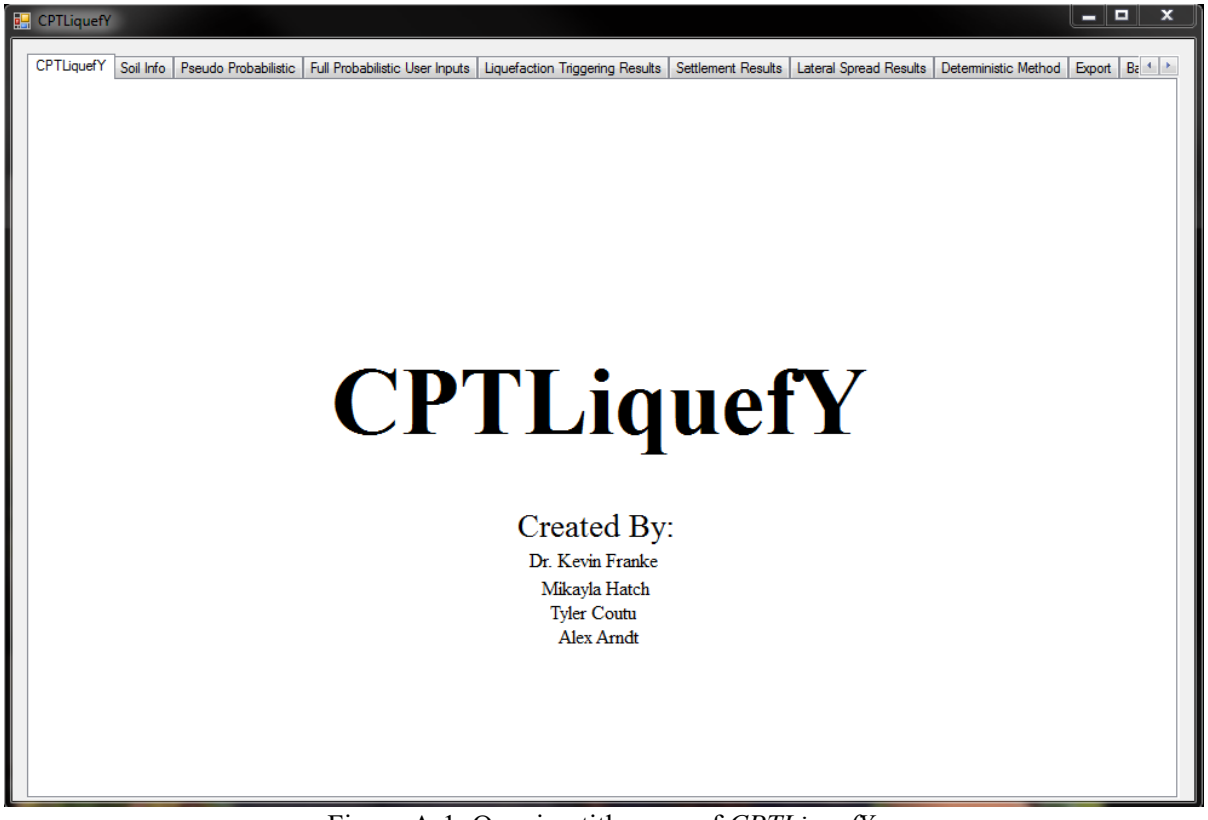

Figure A-1: Opening title page of *CPTLiquefY*.

Soil Info Tab:

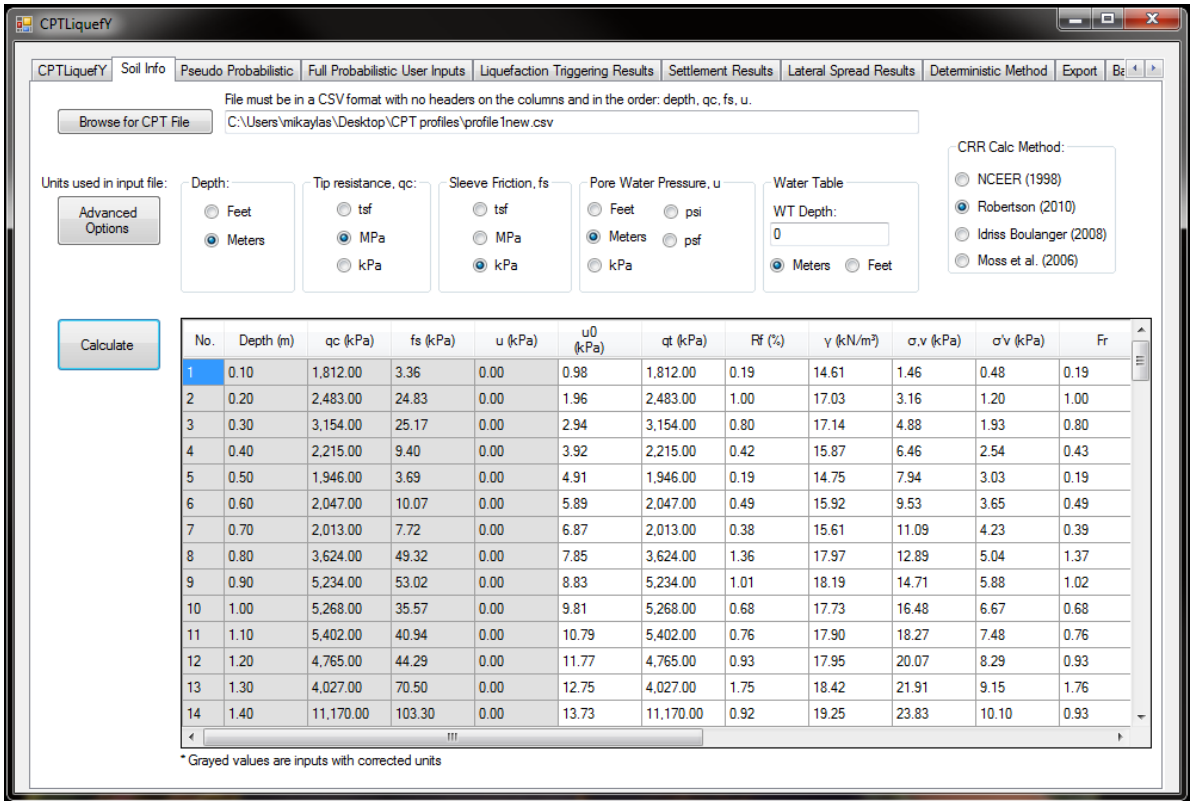

Figure A-2: Screen shot of "Soil Info" tab.

1. Click on "Soil Info" tab (Figure A-2).
2. To upload a CPT profile, click "Browse for CPT File", The CPT profile must be in an excel ".csv" format. The recorded CPT depth, tip resistance, sleeve friction, and pore water pressure need to be in the first, second, third, and fourth columns, respectively.
3. The user must next select what input units the data is currently in.
4. Next, fill out the water table information.
5. The user may adjust some advanced options by clicking the "Advanced Options" button. Adjustable options include, but are not limited to: Net Area Ratio, Reference Pressure, apply K_{α}, apply K_{σ}, apply depth correction factor, apply thin layer correction factor, etc.

6. To run preliminary calculations select the “Calculate” button. This button will run calculations all the way through the calculation of the CRR.

Pseudo-Probabilistic Tab:

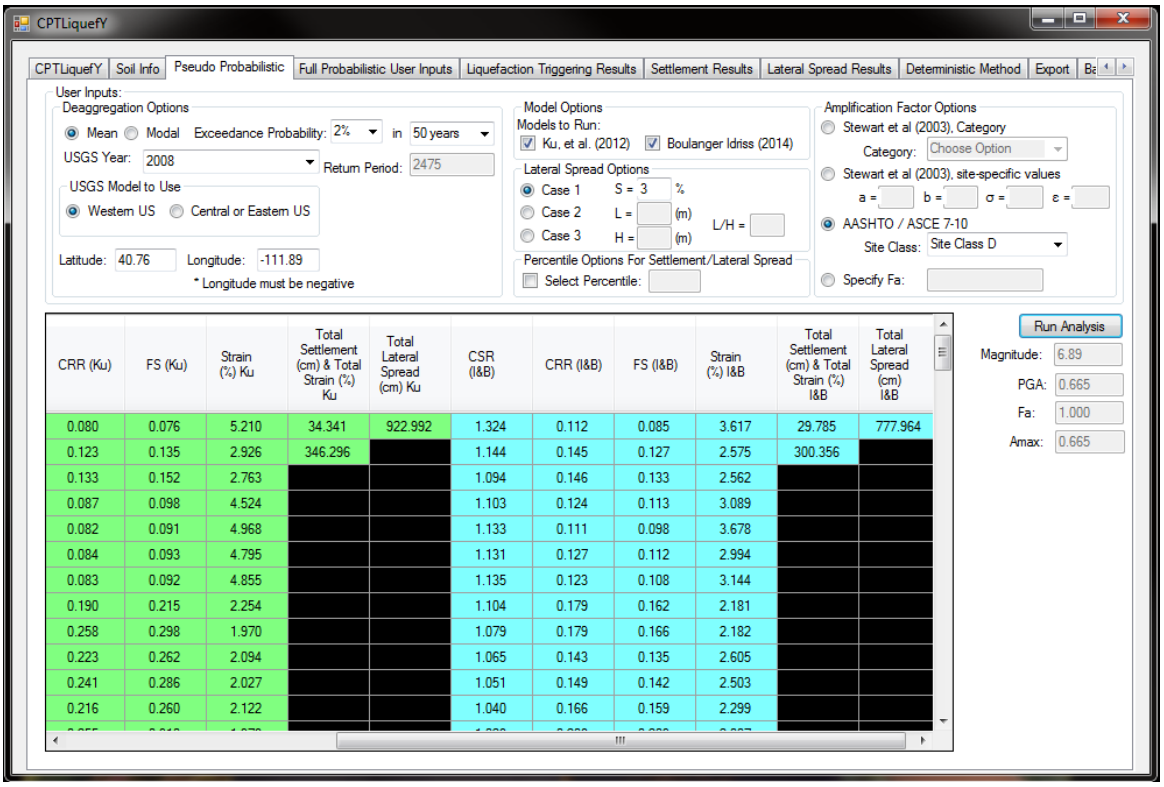

Figure A-3: Screenshot of “Pseudo-probabilistic” tab.

1. Navigate to the “Pseudo Probabilistic” tab (Figure A-3).
2. Select all desired deaggregation options: Mean or Modal magnitude, Return period, USGS tool year, Latitude and Longitude, and if the location is within the western or central/eastern United States.
3. Select which models to run.
4. Enter in Lateral Spread geometry.
5. Select which amplification factor to use.

6. To run a pseudo-probabilistic analysis, select “Run Analysis”. The results will be displayed in the data grid view on that tab.

Full-Probabilistic User Inputs Tab:

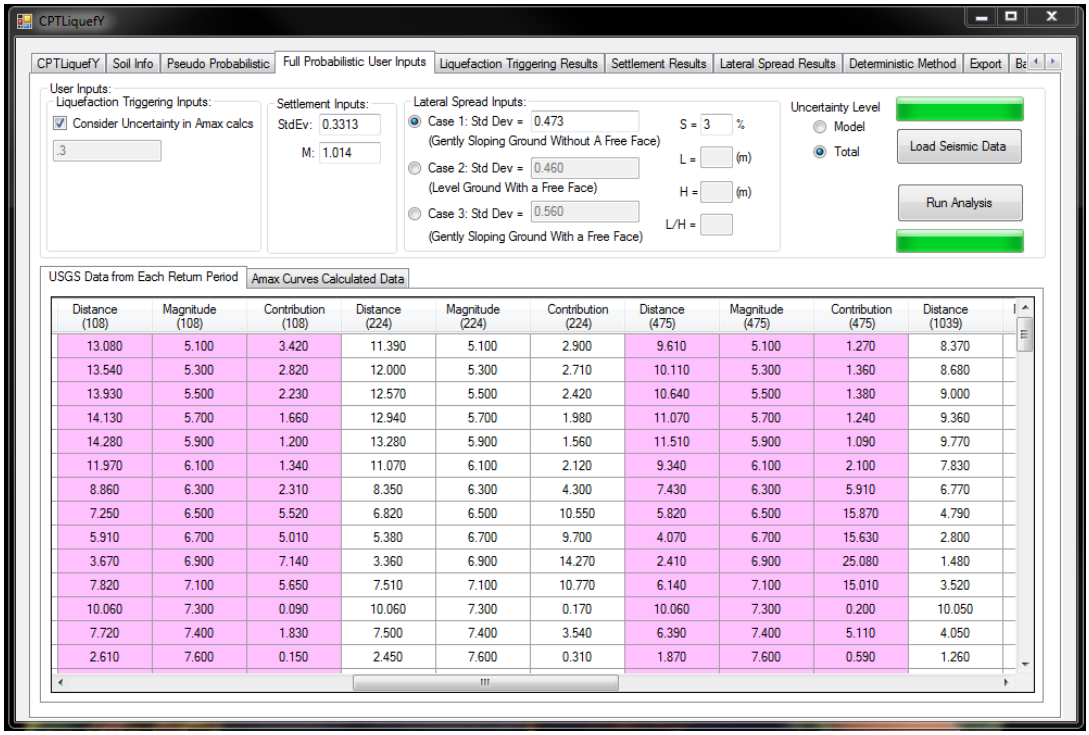

Figure A-4: Screenshot of “Full-Probabilistic User Inputs” tab.

1. Navigate to the “Full-Probabilistic User Inputs” tab (Figure A-4).
2. On this tab, options for the full-probabilistic liquefaction triggering and post-liquefaction settlements and lateral spreading are available to be adjusted.
3. To collect all seismic data for the full-probabilistic analysis and to generate a_{max} hazard curves to run the liquefaction triggering analysis click “Load Seismic Data”. This runs a deaggregations for return periods: 10, 22, 50, 108, 224, 475, 1039, 2475, 4975, 9950, and

19990. *CPTLiquefY* collects the distance, magnitude, and contribution from each return period. At this point everything is ready to run the full-probabilistic analysis.

4. To run the full probabilistic liquefaction triggering, post-liquefaction settlements, and lateral spreading analyses click “Run Analysis”.

5. After the analysis is complete, results can be viewed in their respective tabs. To view liquefaction triggering results navigate to the “Liquefaction Triggering Results” tab. To view post-liquefaction settlement results, navigate to the “Settlement Results” tab. To view post-liquefaction lateral spreading results, navigate to the “Lateral Spread Results” tab.

Settlement Results Tab:

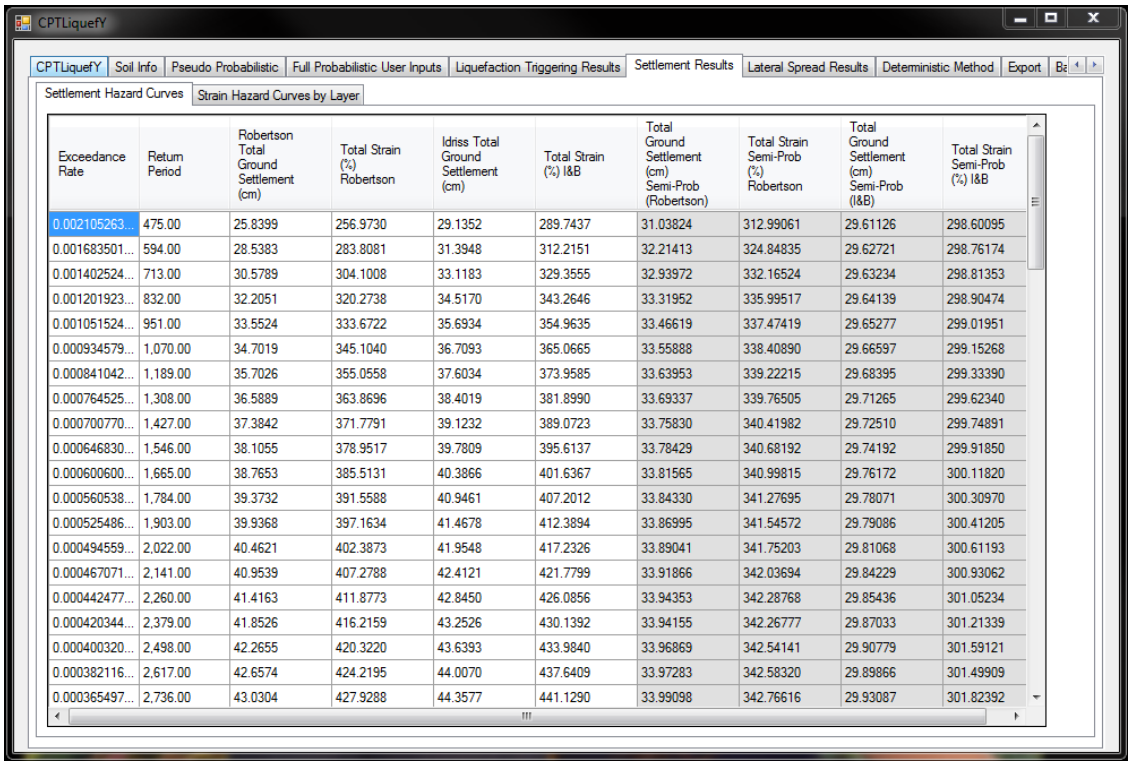

Exceedance Rate	Return Period	Robertson Total Ground Settlement (cm)	Total Strain (%) Robertson	Idriss Total Ground Settlement (cm)	Total Strain (%) I&B	Total Ground Settlement (cm) Semi-Prob (Robertson)	Total Strain Semi-Prob (%) Robertson	Total Ground Settlement (cm) Semi-Prob (I&B)	Total Strain Semi-Prob (%) I&B
0.002105263...	475.00	25.8399	256.9730	29.1352	289.7437	31.03824	312.99061	29.61126	298.60095
0.001683501...	594.00	28.5383	283.8081	31.3948	312.2151	32.21413	324.84835	29.62721	298.76174
0.001402524...	713.00	30.5789	304.1008	33.1183	329.3555	32.93972	332.16524	29.63234	298.81353
0.001201923...	832.00	32.2051	320.2738	34.5170	343.2646	33.31952	335.99517	29.64139	298.90474
0.001051524...	951.00	33.5524	333.6722	35.6934	354.9635	33.46619	337.47419	29.65277	299.01951
0.000934579...	1,070.00	34.7019	345.1040	36.7093	365.0665	33.55888	338.40890	29.66597	299.15268
0.000841042...	1,189.00	35.7026	355.0558	37.6034	373.9585	33.63953	339.22215	29.68395	299.33390
0.000764525...	1,308.00	36.5889	363.8696	38.4019	381.8990	33.69337	339.76505	29.71265	299.62340
0.000700770...	1,427.00	37.3842	371.7791	39.1232	389.0723	33.75830	340.41982	29.72510	299.74891
0.000646830...	1,546.00	38.1055	378.9517	39.7809	395.6137	33.78429	340.68192	29.74192	299.91850
0.000600600...	1,665.00	38.7653	385.5131	40.3866	401.6367	33.81565	340.99815	29.76172	300.11820
0.000560538...	1,784.00	39.3732	391.5588	40.9461	407.2012	33.84330	341.27695	29.78071	300.30970
0.000525486...	1,903.00	39.9368	397.1634	41.4678	412.3894	33.86995	341.54572	29.79086	300.41205
0.000494559...	2,022.00	40.4621	402.3873	41.9548	417.2326	33.89041	341.75203	29.81068	300.61193
0.000467071...	2,141.00	40.9539	407.2788	42.4121	421.7799	33.91866	342.03694	29.84229	300.93062
0.000442477...	2,260.00	41.4163	411.8773	42.8450	426.0856	33.94353	342.28768	29.85436	301.05234
0.000420344...	2,379.00	41.8526	416.2159	43.2526	430.1392	33.94155	342.26777	29.87033	301.21339
0.000400320...	2,498.00	42.2655	420.3220	43.6393	433.9840	33.96869	342.54141	29.90779	301.59121
0.000382116...	2,617.00	42.6574	424.2195	44.0070	437.6409	33.97283	342.58320	29.89866	301.49909
0.000365497...	2,736.00	43.0304	427.9288	44.3577	441.1290	33.99098	342.76616	29.93087	301.82392

Figure A-5: Screenshot of “Settlement Results” tab.

1. Navigate to the “Settlement Results” tab (Figure A-5).

2. The total ground settlement for the full-probabilistic and semi-probabilistic methods are displayed for return periods ranging from 475 to 10,000 years.

3. This data can be easily copy-pasted into excel for plotting.

4. To view the strain hazard curves for each soil layer click the sub tab “Strain Hazard Curves by Layer” and enter the soil layer of interest (Figure A-6).

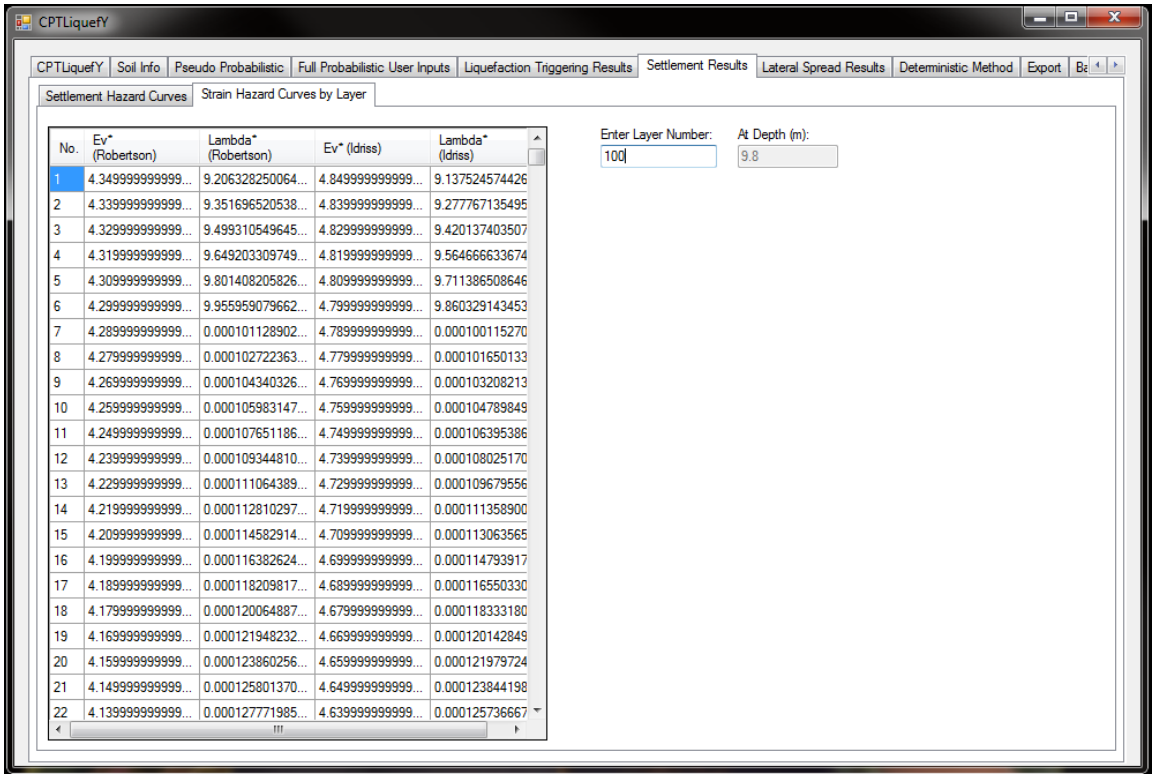

No.	Ev* (Robertson)	Lambda* (Robertson)	Ev* (Idriss)	Lambda* (Idriss)
1	4.349999999999...	9.206328250064...	4.849999999999...	9.137524574426
2	4.339999999999...	9.351696520538...	4.839999999999...	9.277767135495
3	4.329999999999...	9.499310549645...	4.829999999999...	9.420137403507
4	4.319999999999...	9.649203309749...	4.819999999999...	9.564666633674
5	4.309999999999...	9.801408205826...	4.809999999999...	9.711386508646
6	4.299999999999...	9.955959079662...	4.799999999999...	9.860329143453
7	4.289999999999...	0.000101128902...	4.789999999999...	0.000100115270
8	4.279999999999...	0.000102722363...	4.779999999999...	0.000101650133
9	4.269999999999...	0.000104340326...	4.769999999999...	0.000103208213
10	4.259999999999...	0.000105983147...	4.759999999999...	0.000104789849
11	4.249999999999...	0.000107651186...	4.749999999999...	0.000106395386
12	4.239999999999...	0.000109344810...	4.739999999999...	0.000108025170
13	4.229999999999...	0.000111064389...	4.729999999999...	0.000109679556
14	4.219999999999...	0.000112810297...	4.719999999999...	0.000111358900
15	4.209999999999...	0.000114582914...	4.709999999999...	0.000113063565
16	4.199999999999...	0.000116382624...	4.699999999999...	0.000114793917
17	4.189999999999...	0.000118209817...	4.689999999999...	0.000116550330
18	4.179999999999...	0.000120064887...	4.679999999999...	0.000118333180
19	4.169999999999...	0.000121948232...	4.669999999999...	0.000120142849
20	4.159999999999...	0.000123860256...	4.659999999999...	0.000121979724
21	4.149999999999...	0.000125801370...	4.649999999999...	0.000123844198
22	4.139999999999...	0.000127771985...	4.639999999999...	0.000125736667

Figure A-6: Screenshot of “Strain Hazard Curves by Layer” sub-tab.

Export Tab:

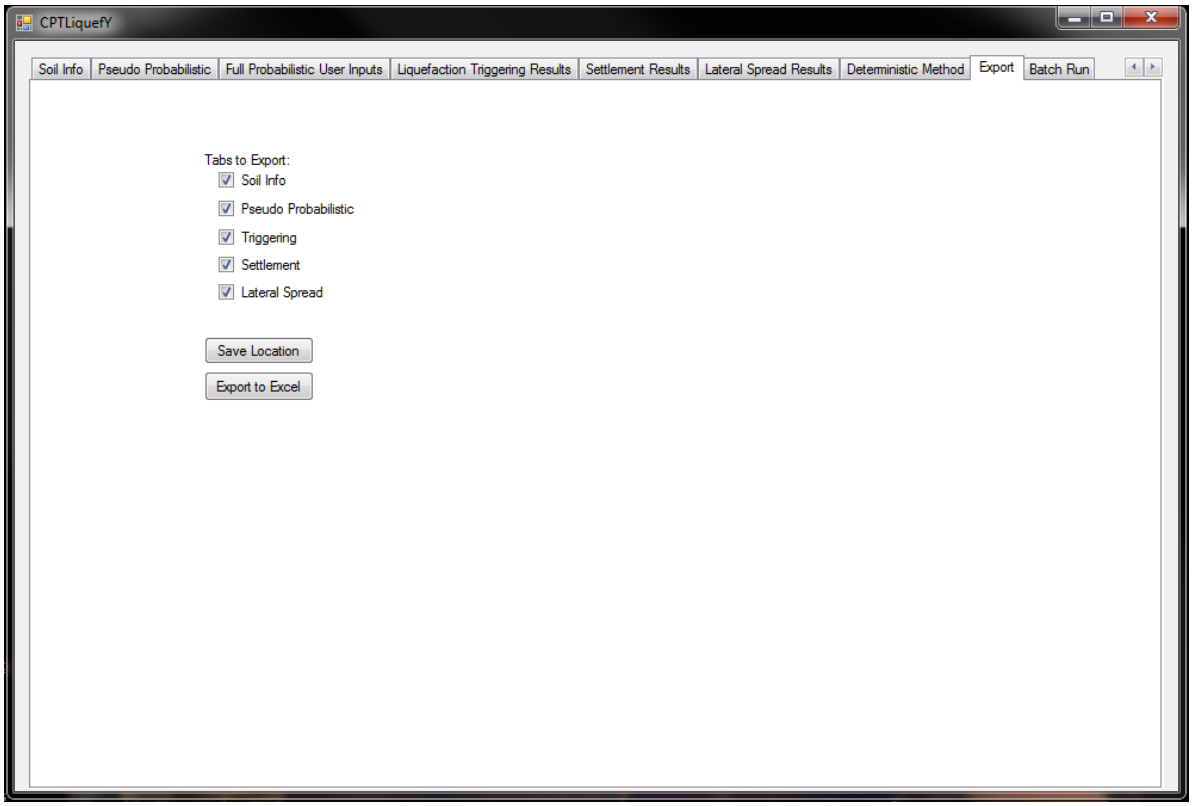

Figure A-7: Screenshot of "Export" tab.

1. All calculated data can be exported to an excel sheet by navigating to the "Export" tab (Figure A-7).
2. Select which data to export.
3. Select "Save Location" to choose the file name and where to save the file.
4. Click "Export to Excel" to export the file.

Batch Run Tab:

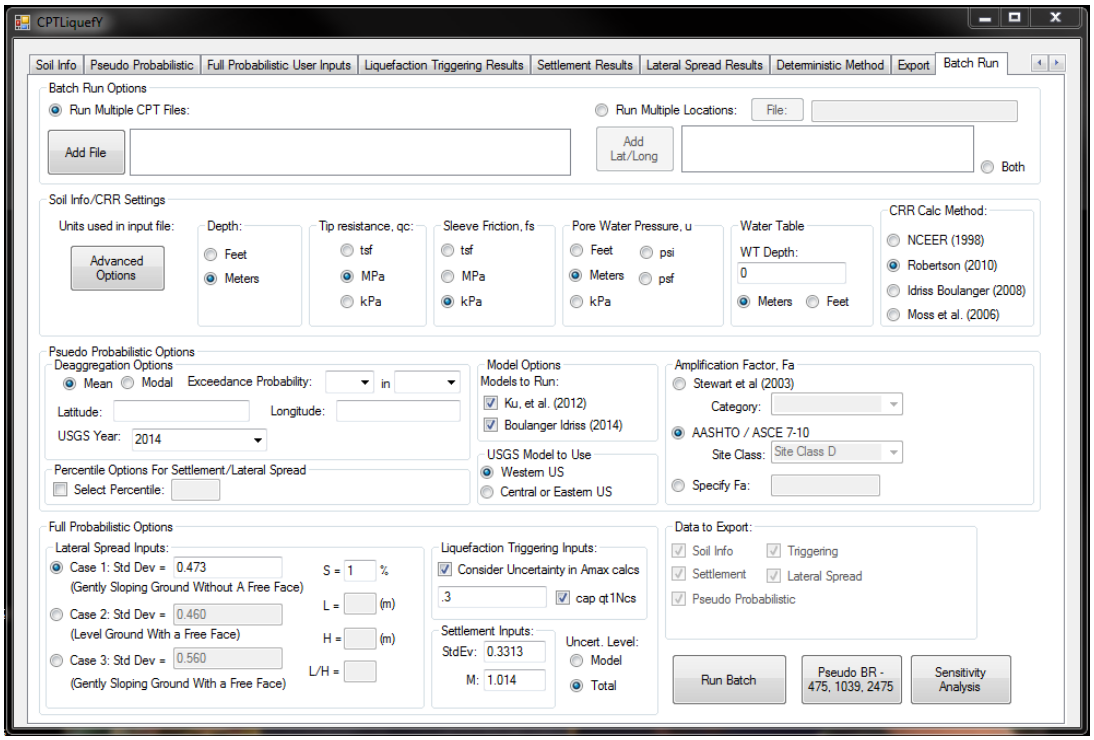

Figure A-8: Screenshot of "Batch Run" tab.

1. To run batch runs, navigate to the "Batch Run" tab (Figure A-8).
2. Here batches can be run for multiple soil profile files at one location, for multiple locations for one soil profile file, or for multiple files and locations.
3. After all options, for all the tabs, are selected on this page select "Run Batch". This button will run the Soil Info, Pseudo-Probabilistic, and Full-Probabilistic tabs automatically for all profiles and locations selected. The results are automatically exported into an excel sheet and saved in the same location as the soil profiles that are being ran.

APPENDIX B: RETURN PERIOD BOX PLOT DATA

Chapter 6 presented box and whisker plots depicting the actual return period compared to the assumed return according to the calculated settlement for the pseudo-probabilistic and semi-probabilistic approaches. The tables are presented in Figures B-1 through B-20, for each city and return period.

Table B-1: Actual Return Periods of Settlement Estimated for Butte, MT (1039)

		Actual T_R					
		Robertson and Wride (2009)			Idriss and Boulanger (2014)		
Profile	Assumed T_R	Mean	Modal	Semi	Mean	Modal	Semi
1	1039	2084.7	951.8	1795.0	1399.7	1278.9	1392.2
2	1039	1575.7	989.4	2016.2	1206.9	1067.9	1229.6
3	1039	1793.6	956.8	1960.6	1553.2	1278.3	1543.9
4	1039	2051.0	820.9	2121.8	1597.2	1267.6	1574.6
5	1039	1133.7	693.3	2820.4	1582.1	1188.9	1652.7
6	1039	2051.3	988.5	2103.5	1462.3	1281.1	1493.4
7	1039	1716.9	931.1	2136.8	1486.2	1267.2	1486.0
8	1039	1209.8	580.1	3188.6	1708.6	1308.8	1786.6
9	1039	1026.4	845.9	2306.8	953.9	781.0	1024.6
10	1039	1621.5	676.5	2887.3	1683.6	1223.2	1739.7
11	1039	1066.7	532.2	3141.2	1823.4	1421.1	1837.4
12	1039	1622.6	627.5	2433.5	1772.4	1398.4	1747.4
13	1039	2453.5	934.3	2005.4	1443.6	1355.8	1452.4
14	1039	988.8	476.7	2870.0	1605.2	1135.6	1663.0
15	1039	1765.6	1008.3	1746.7	1392.6	1263.8	1375.7
16	1039	918.9	525.6	3604.2	1549.6	1384.3	1604.0
17	1039	1149.6	702.8	2804.9	1723.8	1265.7	1692.2
18	1039	611.1	470.0	6422.0	1710.1	1298.8	1721.3
19	1039	1749.4	886.3	2062.0	1590.7	1312.1	1625.7
20	1039	1367.1	591.1	2495.4	1692.9	1301.0	1757.8

Table B-2: Actual Return Periods of Settlement Estimated for Butte, MT (2475)

		Actual T_R					
		Robertson and Wride (2009)			Idriss and Boulanger (2014)		
Profile	Assumed T_R	Mean	Modal	Semi	Mean	Modal	Semi
1	2475	3559.6	2113.0	3195.2	1460.0	1451.0	1464.1
2	2475	2694.7	1586.3	4354.5	1714.0	1468.7	1924.9
3	2475	2988.9	1817.5	3615.2	2114.0	1866.2	2278.6
4	2475	5354.0	2094.3	5024.2	1973.5	1859.5	2067.4
5	2475	2276.6	1147.4	9894.0	2846.0	2112.7	3753.0
6	2475	3317.8	2080.6	3695.8	2001.4	1680.4	2266.3
7	2475	4056.9	1738.7	4497.5	1897.3	1666.4	2066.0
8	2475	3576.3	1237.5	9882.0	3219.7	2282.1	4245.5
9	2475	1496.7	1034.3	7501.8	1501.7	1143.2	2140.9
10	2475	3792.6	1645.0	9976.0	2934.9	2274.2	3801.5
11	2475	4779.4	1085.0	9943.0	2994.4	2334.7	3559.7
12	2475	4758.3	1658.3	9841.8	2286.3	2151.4	2406.9
13	2475	3692.1	2491.0	3814.9	1662.0	1566.4	1726.7
14	2475	5266.9	1008.2	9949.0	3756.0	2503.6	4982.8
15	2475	2637.9	1781.5	2904.6	1423.0	1404.6	1454.6
16	2475	3241.6	934.9	9971.0	2731.5	2054.9	3089.8
17	2475	3686.7	1169.9	9998.0	2420.1	2177.8	2602.8
18	2475	1614.9	619.8	9924.0	2909.5	2506.4	3207.0
19	2475	3750.5	1773.6	4450.2	2274.5	1914.9	2546.2
20	2475	5192.0	1394.9	9921.0	3103.2	2355.4	3917.2

Table B-3: Actual Return Periods of Settlement Estimated for Eureka, CA (1039)

		Actual T_R					
		Robertson and Wride (2009)			Idriss and Boulanger (2014)		
Profile	Assumed T_R	Mean	Modal	Semi	Mean	Modal	Semi
1	1039	463.0	435.0	411.0	1328.4	1341.7	1328.6
2	1039	3404.4	1342.2	845.6	931.8	1008.6	967.2
3	1039	500.3	462.0	422.0	1133.1	1149.2	1133.3
4	1039	433.0	417.0	437.0	1201.5	1210.3	1202.0
5	1039	9910.0	9926.0	2428.4	872.4	561.3	854.6
6	1039	427.0	430.0	452.0	1218.8	1218.9	1218.9
7	1039	599.0	586.0	412.0	1157.7	1157.7	1157.7
8	1039	9951.0	9929.0	1589.5	559.5	604.6	561.4
9	1039	9995.0	9508.4	3968.6	1341.8	886.9	1346.4
10	1039	9989.0	7712.0	1156.5	694.7	748.7	693.0
11	1039	9921.0	6532.1	1735.4	595.6	652.9	595.4
12	1039	5228.2	2618.2	1010.4	884.6	959.6	887.3
13	1039	459.0	465.0	462.0	1316.4	1316.4	1316.4
14	1039	3437.5	3274.8	1146.5	744.3	744.3	744.3
15	1039	402.0	467.0	415.0	1348.4	1355.1	1349.9
16	1039	9988.0	9936.0	1831.1	1109.5	1109.5	1109.5
17	1039	4361.2	3338.9	1070.5	1050.6	1075.3	1050.6
18	1039	9964.0	9893.0	5764.6	880.5	884.4	881.5
19	1039	810.3	679.6	401.0	947.0	976.2	948.0
20	1039	2831.0	2430.7	901.6	819.7	837.8	820.1

Table B-4: Actual Return Periods of Settlement Estimated for Eureka, CA (2475)

		Actual T_R					
		Robertson and Wride (2009)			Idriss and Boulanger (2014)		
Profile	Assumed T_R	Mean	Modal	Semi	Mean	Modal	Semi
1	2475	465.0	425.0	400.0	1324.6	1326.9	1326.5
2	2475	9877.0	4216.4	1039.7	735.2	870.0	845.8
3	2475	532.7	505.5	419.0	1112.7	1128.0	1120.1
4	2475	490.2	472.0	469.0	1182.3	1199.6	1187.1
5	2475	9999.0	9909.0	3385.7	1376.4	855.9	1372.5
6	2475	416.0	452.0	463.0	1216.0	1218.7	1217.8
7	2475	616.0	601.0	456.0	937.9	1012.6	1157.7
8	2475	9958.0	9876.0	2101.7	504.8	550.3	515.0
9	2475	9877.0	9985.0	6733.6	1942.5	1395.9	1905.3
10	2475	9999.0	9877.0	1425.2	619.1	693.7	612.0
11	2475	9936.0	9958.0	2260.5	508.5	584.5	513.7
12	2475	9959.0	5927.8	1179.9	797.8	883.5	802.5
13	2475	418.0	467.0	443.0	1270.2	1287.3	1316.4
14	2475	3513.4	3458.4	1346.7	729.2	731.4	744.3
15	2475	420.0	473.0	434.0	1150.5	1216.4	1329.8
16	2475	9984.0	9946.0	2553.8	598.5	648.7	1109.5
17	2475	5632.7	4602.9	1315.1	935.2	969.9	1049.6
18	2475	9890.0	9945.0	8692.4	683.8	750.8	873.1
19	2475	955.7	832.9	439.0	894.4	930.5	912.6
20	2475	3156.6	2888.8	1050.4	808.1	819.3	810.0

Table B-5: Actual Return Periods of Settlement Estimated for Santa Monica, CA (1039)

		Actual T_R					
		Robertson and Wride (2009)			Idriss and Boulanger (2014)		
Profile	Assumed T_R	Mean	Modal	Semi	Mean	Modal	Semi
1	1039	417.0	453.0	415.0	1314.9	1307.6	1305.3
2	1039	581.3	828.3	885.3	941.9	930.1	943.8
3	1039	554.1	591.4	465.0	1052.1	1043.4	1043.1
4	1039	538.1	561.6	486.7	1125.0	1121.2	1120.7
5	1039	3422.0	8415.7	3334.5	525.1	632.5	667.5
6	1039	520.4	549.5	435.0	1103.1	1103.1	1103.1
7	1039	780.7	801.9	451.0	1072.2	1056.4	1055.6
8	1039	9967.0	9912.0	2296.5	529.4	480.4	476.2
9	1039	3562.0	8624.1	4148.2	674.0	951.6	1002.4
10	1039	4784.6	7868.2	1620.9	634.0	611.9	604.1
11	1039	5390.3	8346.2	2658.4	598.4	531.8	524.4
12	1039	1721.4	2506.9	1501.1	920.2	886.7	879.9
13	1039	403.0	412.0	442.0	1223.7	1223.7	1223.7
14	1039	5170.6	6198.5	1870.8	536.4	521.2	519.5
15	1039	419.0	465.0	457.0	1340.9	1332.8	1331.8
16	1039	9915.0	9974.0	2656.2	996.8	996.8	996.8
17	1039	5534.3	7178.3	1513.3	1004.2	992.0	988.8
18	1039	9960.0	9999.0	9956.0	774.3	751.6	745.9
19	1039	692.2	786.0	505.3	887.5	869.8	867.2
20	1039	3459.3	4239.5	1342.7	705.3	680.0	675.9

Table B-6: Actual Return Periods of Settlement Estimated for Santa Monica, CA (2475)

		Actual T_R					
		Robertson and Wride (2009)			Idriss and Boulanger (2014)		
Profile	Assumed T_R	Mean	Modal	Semi	Mean	Modal	Semi
1	2475	472.0	475.0	408.0	1301.1	1294.7	1287.3
2	2475	1207.2	1683.5	1127.3	895.9	879.1	891.8
3	2475	621.5	643.6	436.0	1038.5	1032.0	1028.2
4	2475	578.5	587.7	516.1	1117.9	1114.4	1110.8
5	2475	9935.0	9946.0	5535.1	766.0	961.3	1098.7
6	2475	556.1	557.3	403.0	1103.1	1103.1	1103.1
7	2475	838.2	867.6	515.4	1054.7	1054.7	1054.7
8	2475	9966.0	9980.0	3416.9	512.2	552.8	571.0
9	2475	9909.0	9931.0	8230.7	1445.0	2608.4	3348.4
10	2475	9907.0	9992.0	2160.0	583.6	562.6	541.8
11	2475	9961.0	9899.0	3823.6	493.5	493.0	521.4
12	2475	3696.1	5154.0	1874.4	865.3	840.8	818.3
13	2475	407.0	438.0	411.0	1223.7	1223.7	1223.7
14	2475	7592.5	8841.3	2403.1	513.2	512.6	512.6
15	2475	461.0	412.0	429.0	1318.6	1307.9	1306.2
16	2475	9913.0	9906.0	4146.8	996.8	996.8	996.8
17	2475	8449.5	9309.0	2079.4	978.7	963.8	951.2
18	2475	9967.0	9925.0	9958.0	732.0	722.0	714.4
19	2475	873.2	948.6	568.8	855.9	840.7	830.0
20	2475	5112.1	5714.9	1671.5	664.4	652.7	645.5

Table B-7: Actual Return Periods of Settlement Estimated for Salt Lake City, UT (1039)

		Actual T_R					
		Robertson and Wride (2009)			Idriss and Boulanger (2014)		
Profile	Assumed T_R	Mean	Modal	Semi	Mean	Modal	Semi
1	1039	960.4	962.9	915.6	524.0	524.5	524.8
2	1039	1139.3	1212.9	1938.8	751.8	757.7	743.2
3	1039	1398.8	1434.6	1114.1	699.2	702.2	698.2
4	1039	1451.9	1467.5	1310.8	648.4	649.9	648.8
5	1039	2174.3	2522.1	3752.0	1166.1	1200.2	1173.6
6	1039	1564.5	1580.9	1051.6	677.4	677.4	676.9
7	1039	1936.2	2012.0	1215.3	644.1	647.0	644.8
8	1039	7998.2	9083.0	2889.7	1201.5	1218.0	1204.3
9	1039	2137.8	2423.2	4155.8	1324.6	1381.5	1373.1
10	1039	3572.1	4072.4	2508.9	1031.5	1044.1	1029.7
11	1039	5022.4	5409.8	3293.4	1048.8	1064.1	1054.1
12	1039	2435.8	2557.8	2408.8	734.3	743.0	739.5
13	1039	1095.1	1103.5	936.3	576.2	577.0	576.0
14	1039	6234.1	6640.5	2588.7	1163.1	1183.3	1160.6
15	1039	1159.4	1170.5	952.1	499.0	499.5	499.5
16	1039	9973.0	9897.0	3159.4	741.2	741.2	741.2
17	1039	5576.6	6035.4	2243.2	713.3	716.3	714.5
18	1039	7816.3	9440.9	6935.0	876.0	886.4	877.8
19	1039	1702.2	1740.6	1325.4	820.8	826.6	824.4
20	1039	4311.5	4631.4	2218.9	980.2	988.5	980.7

Table B-8: Actual Return Periods of Settlement Estimated for Salt Lake City, UT (2475)

		Actual T_R					
		Robertson and Wride (2009)			Idriss and Boulanger (2014)		
Profile	Assumed T_R	Mean	Modal	Semi	Mean	Modal	Semi
1	2475	994.9	997.8	948.8	534.3	535.2	537.9
2	2475	2415.1	2524.0	2824.7	828.8	831.2	821.6
3	2475	1858.4	1872.2	1287.3	716.9	718.6	722.6
4	2475	1632.4	1640.4	1465.4	661.1	661.8	664.0
5	2475	9995.0	9910.0	7374.9	1701.6	1742.1	1902.7
6	2475	1825.2	1829.6	1178.9	677.4	677.4	677.4
7	2475	2298.8	2309.4	1426.7	703.4	703.4	703.4
8	2475	9915.0	9975.0	4939.1	1450.8	1464.0	1520.7
9	2475	9910.0	9969.0	9975.0	2289.1	2386.9	2941.3
10	2475	9897.0	9947.0	3862.3	1161.0	1168.1	1200.8
11	2475	9892.0	9964.0	5550.0	1339.3	1354.6	1412.8
12	2475	5137.4	5407.2	3570.1	853.0	857.2	876.0
13	2475	1194.6	1198.8	995.5	579.8	579.8	579.8
14	2475	9956.0	9979.0	4018.1	1332.9	1335.9	1345.7
15	2475	1288.5	1299.2	1052.6	510.6	511.6	517.0
16	2475	9979.0	9878.0	5446.2	741.2	741.2	741.2
17	2475	9977.0	9982.0	3499.6	756.0	757.8	767.5
18	2475	9890.0	9901.0	9910.0	991.8	995.1	1008.3
19	2475	2312.3	2346.9	1604.5	904.6	908.2	920.1
20	2475	8239.9	8457.4	3177.8	1077.9	1083.4	1098.6

Table B-9: Actual Return Periods of Settlement Estimated for San Jose, CA (1039)

		Actual T_R					
		Robertson and Wride (2009)			Idriss and Boulanger (2014)		
Profile	Assumed T_R	Mean	Modal	Semi	Mean	Modal	Semi
1	1039	426.0	407.0	460.0	2175.7	2177.8	2167.0
2	1039	416.0	403.0	549.5	1278.7	1283.7	1261.3
3	1039	445.0	420.0	475.0	1439.0	1442.7	1428.9
4	1039	470.0	431.0	449.0	1509.7	1511.3	1504.3
5	1039	5794.3	3994.7	3010.5	692.7	729.4	499.9
6	1039	445.0	452.0	424.0	1426.3	1426.3	1426.3
7	1039	406.0	459.0	423.0	1422.9	1428.0	1422.4
8	1039	9949.0	9981.0	1981.4	855.6	871.4	782.0
9	1039	5437.5	3862.2	3882.2	475.2	546.0	1176.5
10	1039	5261.2	4334.9	1207.4	1005.3	1015.5	957.5
11	1039	5990.1	5069.0	2250.8	904.1	925.2	836.1
12	1039	1631.2	1406.5	1107.6	1271.3	1281.5	1227.1
13	1039	407.0	465.0	435.0	1609.8	1609.8	1609.8
14	1039	4478.8	4171.6	1492.0	906.1	910.3	896.4
15	1039	472.0	431.0	422.0	1706.8	1710.2	1686.7
16	1039	9975.0	9956.0	2349.6	1397.2	1397.2	1397.2
17	1039	4978.3	4556.3	1182.9	1387.5	1391.4	1363.7
18	1039	9992.0	9977.0	9961.0	1138.6	1145.4	1109.8
19	1039	472.0	406.0	441.0	1252.9	1259.1	1227.1
20	1039	2868.7	2667.0	983.2	1075.3	1086.1	1047.8

Table B-10: Actual Return Periods of Settlement Estimated for San Jose, CA (2475)

		Actual T_R					
		Robertson and Wride (2009)			Idriss and Boulanger (2014)		
Profile	Assumed T_R	Mean	Modal	Semi	Mean	Modal	Semi
1	2475	434.0	437.0	461.0	2168.8	2171.3	2153.8
2	2475	773.6	628.2	669.2	1234.0	1247.2	1210.5
3	2475	468.0	400.0	406.0	1429.7	1433.4	1412.0
4	2475	467.0	419.0	457.0	1504.4	1506.4	1494.1
5	2475	9889.0	9921.0	4555.5	518.4	591.5	776.9
6	2475	433.0	465.0	426.0	1426.3	1426.3	1426.3
7	2475	459.0	469.0	475.0	1422.4	1422.4	1422.4
8	2475	9899.0	9962.0	2713.2	784.7	813.1	709.1
9	2475	9909.0	9938.0	6713.8	969.6	700.7	2270.2
10	2475	9934.0	8739.6	1516.9	961.2	976.2	900.7
11	2475	9990.0	9834.2	2997.2	842.6	864.3	753.4
12	2475	2924.8	2354.2	1298.8	1235.6	1249.4	1157.1
13	2475	437.0	403.0	473.0	1609.8	1609.8	1609.8
14	2475	6000.7	5443.0	1786.4	896.3	897.4	896.3
15	2475	475.0	456.0	406.0	1685.0	1693.9	1676.8
16	2475	9893.0	9933.0	3478.3	1397.2	1397.2	1397.2
17	2475	6217.3	5869.7	1509.4	1366.0	1374.7	1327.0
18	2475	9907.0	9889.0	9973.0	1111.5	1119.8	1096.6
19	2475	486.4	461.0	468.0	1229.2	1238.8	1193.0
20	2475	3745.3	3432.0	1161.9	1050.2	1058.7	1021.7

Table B-11: Actual Return Periods of Settlement Estimated for San Fran, CA (1039)

		Actual T_R					
		Robertson and Wride (2009)			Idriss and Boulanger (2014)		
Profile	Assumed T_R	Mean	Modal	Semi	Mean	Modal	Semi
1	1039	400.0	427.0	433.0	1343.6	1336.8	1335.2
2	1039	642.8	828.2	785.6	999.8	980.8	985.9
3	1039	486.4	505.3	408.0	1114.3	1107.3	1105.2
4	1039	444.0	416.0	405.0	1177.7	1174.2	1173.0
5	1039	4763.0	9889.0	2747.6	488.4	585.9	636.6
6	1039	473.0	431.0	426.0	1169.0	1169.0	1169.0
7	1039	639.6	658.3	437.0	1101.6	1097.4	1097.4
8	1039	9904.0	9883.0	1822.9	588.4	548.0	532.3
9	1039	5114.1	8056.6	3712.9	689.3	997.5	1204.6
10	1039	4924.1	7119.7	1301.2	713.4	687.2	676.1
11	1039	4998.5	7131.9	2055.8	628.7	589.0	576.1
12	1039	1682.3	2213.8	1181.9	947.5	923.5	915.1
13	1039	416.0	420.0	457.0	1274.1	1274.1	1274.1
14	1039	3951.5	4572.3	1416.7	633.7	626.2	624.0
15	1039	441.0	446.0	449.0	1375.8	1366.2	1357.4
16	1039	9878.0	9953.0	2109.3	1059.9	1059.9	1059.9
17	1039	4562.0	5235.0	1206.5	1061.7	1051.0	1044.4
18	1039	9945.0	9954.0	8246.5	832.0	817.6	808.6
19	1039	627.5	678.4	427.0	940.4	926.2	920.0
20	1039	2848.8	3279.9	1058.1	777.1	759.9	756.0

Table B-12: Actual Return Periods of Settlement Estimated for San Jose, CA (2475)

		Actual T_R					
		Robertson and Wride (2009)			Idriss and Boulanger (2014)		
Profile	Assumed T_R	Mean	Modal	Semi	Mean	Modal	Semi
1	2475	430.0	454.0	431.0	1331.0	1321.6	1312.8
2	2475	1211.8	1744.8	955.9	953.2	931.2	933.3
3	2475	527.9	542.6	400.0	1102.6	1093.7	1089.5
4	2475	434.0	479.6	421.0	1171.0	1166.0	1162.7
5	2475	9988.0	9876.0	4074.1	707.7	907.3	1101.7
6	2475	449.0	452.0	430.0	1169.0	1169.0	1169.0
7	2475	688.6	703.1	458.0	1097.4	1097.4	1097.4
8	2475	9973.0	9966.0	2528.7	508.9	477.8	494.0
9	2475	9895.0	9932.0	6732.9	1565.1	2093.2	2661.1
10	2475	9998.0	9906.0	1638.4	664.3	637.8	618.6
11	2475	9965.0	9987.0	2742.8	557.3	517.9	496.7
12	2475	3235.9	4407.1	1414.5	904.1	869.7	846.6
13	2475	472.0	409.0	475.0	1274.1	1274.1	1274.1
14	2475	5462.5	6210.6	1745.1	623.8	623.8	623.8
15	2475	410.0	422.0	426.0	1350.1	1347.8	1345.3
16	2475	9904.0	9972.0	2976.8	1059.9	1059.9	1059.9
17	2475	5849.1	6503.0	1558.2	1036.2	1018.7	1003.4
18	2475	9877.0	9896.0	9980.0	803.2	793.3	793.2
19	2475	748.8	811.2	478.7	912.3	895.7	885.2
20	2475	3804.2	4135.8	1263.1	749.0	735.5	729.7

Table B-13: Actual Return Periods of Settlement Estimated for Seattle, WA (1039)

		Actual T_R					
		Robertson and Wride (2009)			Idriss and Boulanger (2014)		
Profile	Assumed T_R	Mean	Modal	Semi	Mean	Modal	Semi
1	1039	445.0	424.0	410.0	964.4	961.9	959.1
2	1039	593.3	752.9	1258.4	651.9	632.4	621.2
3	1039	751.2	833.5	625.1	710.1	699.9	697.2
4	1039	854.7	892.3	802.7	775.5	770.0	766.5
5	1039	1497.4	2837.5	3963.5	674.3	777.3	874.2
6	1039	811.2	845.8	555.7	732.8	732.5	732.5
7	1039	1123.1	1280.4	728.3	774.8	763.2	746.8
8	1039	7173.8	9891.0	2945.5	671.8	707.1	744.7
9	1039	1409.5	2494.1	4417.3	768.3	922.2	1104.5
10	1039	2585.0	4577.8	2212.9	579.0	609.4	635.6
11	1039	4475.2	6276.2	3451.4	568.8	606.4	642.4
12	1039	1789.3	2237.2	2075.6	660.5	632.6	604.1
13	1039	559.6	574.2	485.3	865.8	861.7	860.1
14	1039	5591.8	7285.6	2525.0	660.5	708.6	739.7
15	1039	577.2	600.5	486.8	985.3	982.6	978.4
16	1039	9966.0	9917.0	3370.3	625.4	625.4	625.4
17	1039	4672.9	6739.8	2041.2	682.1	672.2	661.0
18	1039	8432.8	9907.0	9885.0	507.1	481.9	488.5
19	1039	964.5	1059.9	792.1	597.1	578.9	563.6
20	1039	3386.7	4560.2	1903.3	532.1	550.5	565.4

Table B-14: Actual Return Periods of Settlement Estimated for San Fran, CA (2475)

		Actual T_R					
		Robertson and Wride (2009)			Idriss and Boulanger (2014)		
Profile	Assumed T_R	Mean	Modal	Semi	Mean	Modal	Semi
1	2475	477.8	482.7	452.0	956.8	953.1	944.5
2	2475	1062.5	1311.3	1657.6	597.5	591.8	585.4
3	2475	984.4	1025.1	695.0	695.5	691.3	683.2
4	2475	942.1	968.0	867.0	764.5	762.6	758.1
5	2475	6809.3	9890.0	6863.6	952.9	1059.7	1350.8
6	2475	920.9	955.6	600.4	732.5	732.5	732.5
7	2475	1373.9	1394.9	826.2	725.9	717.7	712.3
8	2475	9961.0	9878.0	4532.9	783.1	824.2	916.6
9	2475	7336.9	9981.0	9190.9	1240.7	1497.4	2565.9
10	2475	9087.9	9967.0	3102.2	649.4	662.6	702.2
11	2475	9958.0	9932.0	5217.3	695.6	747.2	826.4
12	2475	3178.4	3978.4	2828.9	584.8	565.9	538.5
13	2475	598.6	613.0	507.4	860.1	860.1	860.1
14	2475	9479.8	9893.0	3559.5	766.0	779.4	794.4
15	2475	625.3	643.2	523.1	976.3	972.2	957.8
16	2475	9918.0	9969.0	5227.0	625.4	625.4	625.4
17	2475	9927.0	9962.0	2920.7	654.2	647.9	633.1
18	2475	9972.0	9979.0	9916.0	507.9	521.6	539.7
19	2475	1236.5	1335.1	914.4	547.0	538.3	520.1
20	2475	6319.7	7135.3	2512.2	574.0	586.5	608.1

Table B-15: Actual Return Periods of Settlement Estimated for Charleston, S.C. (1039)

		Actual T_R					
		Robertson and Wride (2009)			Idriss and Boulanger (2014)		
Profile	Assumed T_R	Mean	Modal	Semi	Mean	Modal	Semi
1	1039	1552.2	1575.9	1432.9	745.8	750.0	744.3
2	1039	1583.7	2148.6	2218.1	1054.5	1105.4	949.1
3	1039	2080.8	2404.9	1527.2	970.7	992.5	944.5
4	1039	2124.5	2249.2	1708.3	906.3	916.9	895.6
5	1039	2435.3	5149.0	3024.3	1522.7	1798.0	1341.4
6	1039	2417.6	2572.3	1556.3	953.2	953.8	946.0
7	1039	2664.3	3199.8	1633.8	898.4	922.4	879.3
8	1039	8126.7	9981.0	2634.5	1622.2	1747.0	1423.1
9	1039	2529.0	5131.4	2958.0	1717.8	2137.2	1293.1
10	1039	3924.1	8104.8	2524.1	1400.4	1498.6	1281.0
11	1039	5682.8	8772.7	2880.2	1412.3	1537.8	1244.2
12	1039	3068.6	4117.5	2378.0	1008.7	1073.6	958.8
13	1039	1693.4	1762.6	1399.6	811.6	818.3	803.7
14	1039	7125.1	9915.0	2354.4	1561.2	1705.8	1423.4
15	1039	1834.0	1941.4	1410.5	704.6	708.2	702.0
16	1039	9913.0	9956.0	2931.1	1032.5	1032.5	1029.6
17	1039	6208.0	9744.7	2219.9	997.3	1021.4	967.2
18	1039	6693.3	9960.0	4773.4	1195.0	1267.6	1107.1
19	1039	2452.0	2804.0	1748.3	1140.1	1188.6	1079.6
20	1039	5135.0	7534.9	2257.1	1338.0	1402.2	1263.6

Table B-16: Actual Return Periods of Settlement Estimated for Charleston, S.C. (2475)

		Actual T_R					
		Robertson and Wride (2009)			Idriss and Boulanger (2014)		
Profile	Assumed T_R	Mean	Modal	Semi	Mean	Modal	Semi
1	2475	1630.1	1652.4	1528.8	766.9	775.8	761.2
2	2475	4528.4	6857.4	3864.5	1206.0	1253.9	1136.0
3	2475	2944.3	3080.6	1922.1	1013.9	1025.5	1005.2
4	2475	2473.1	2539.0	2127.1	929.3	934.6	925.1
5	2475	9952.0	9899.0	8112.2	2567.9	3277.0	2314.6
6	2475	2889.7	2906.0	1810.7	953.8	953.8	953.8
7	2475	3477.4	3645.1	2037.2	990.4	990.4	987.1
8	2475	9992.0	9927.0	5557.8	2085.4	2294.7	1984.1
9	2475	9921.0	9998.0	9997.0	3718.4	6143.0	3048.3
10	2475	9878.0	9991.0	4683.4	1652.9	1732.5	1597.5
11	2475	9989.0	9977.0	6295.8	1932.2	2076.1	1807.1
12	2475	8688.6	9916.0	4419.6	1215.1	1277.5	1180.1
13	2475	1899.2	1910.2	1541.9	818.4	818.4	818.4
14	2475	9952.0	9966.0	4760.4	1853.9	1861.7	1830.0
15	2475	2126.7	2191.4	1657.8	729.2	746.5	721.3
16	2475	9932.0	9963.0	6124.2	1032.5	1032.5	1032.5
17	2475	9980.0	9934.0	4146.6	1069.1	1100.5	1057.7
18	2475	9906.0	9944.0	9960.0	1398.8	1435.5	1370.6
19	2475	3701.2	4119.6	2304.0	1286.2	1325.5	1262.8
20	2475	9931.0	9897.0	3959.2	1518.8	1560.1	1484.6

Table B-17: Actual Return Periods of Settlement Estimated for Portland, OR (1039)

		Actual T_R					
		Robertson and Wride (2009)			Idriss and Boulanger (2014)		
Profile	Assumed T_R	Mean	Modal	Semi	Mean	Modal	Semi
1	1039	1067.3	1072.4	1022.0	558.0	558.2	559.0
2	1039	821.6	872.7	1932.6	704.8	724.4	793.2
3	1039	1109.1	1234.2	1225.6	739.4	753.2	784.5
4	1039	1499.2	1588.0	1480.8	703.7	709.5	724.8
5	1039	825.2	1016.4	3758.1	1021.0	1094.9	1273.7
6	1039	1090.9	1246.7	1168.7	752.6	762.4	773.1
7	1039	1251.1	1409.0	1392.7	691.6	701.0	710.7
8	1039	1472.2	2179.8	3265.4	1073.9	1159.4	1352.5
9	1039	659.7	799.9	3436.3	787.2	867.9	1318.4
10	1039	1269.7	1531.8	2860.0	1011.2	1065.2	1203.3
11	1039	1805.7	2484.2	3696.2	956.5	1005.9	1174.9
12	1039	1653.4	1916.3	2662.6	764.6	778.2	822.1
13	1039	1020.0	1069.1	1047.6	621.7	627.0	638.0
14	1039	2407.6	3372.1	2870.0	1151.4	1210.4	1334.4
15	1039	1027.7	1123.2	1025.0	539.8	539.8	542.2
16	1039	1014.1	1406.9	3788.2	874.3	896.2	911.9
17	1039	1654.8	2387.1	2529.5	778.2	790.9	802.9
18	1039	979.4	1404.4	8262.3	880.6	915.8	996.7
19	1039	1221.1	1411.3	1469.1	820.5	848.1	904.4
20	1039	1859.8	2384.1	2511.8	1023.6	1074.5	1157.1

Table B-18: Actual Return Periods of Settlement Estimated for Portland, OR (2475)

		Actual T_R					
		Robertson and Wride (2009)			Idriss and Boulanger (2014)		
Profile	Assumed T_R	Mean	Modal	Semi	Mean	Modal	Semi
1	2475	1092.3	1098.1	1069.5	559.2	559.6	568.9
2	2475	1102.5	1201.1	3006.9	837.0	859.4	942.5
3	2475	1539.7	1616.4	1452.2	787.1	793.3	822.3
4	2475	1761.1	1794.0	1760.8	729.1	731.4	749.0
5	2475	1863.4	2311.0	8732.7	1317.1	1386.7	2169.6
6	2475	1729.5	1808.3	1312.1	775.5	776.9	778.3
7	2475	1966.7	2195.4	1640.0	717.5	722.6	793.5
8	2475	7517.5	9980.0	6149.5	1402.7	1457.0	1806.7
9	2475	1759.4	2280.4	9939.0	1406.5	1529.5	2861.8
10	2475	3022.9	3885.6	4719.7	1254.3	1285.2	1484.3
11	2475	5640.2	6725.9	7095.0	1226.4	1268.3	1654.2
12	2475	2760.6	3108.8	4402.8	835.7	849.6	1010.5
13	2475	1214.2	1256.5	1133.4	641.8	643.2	650.6
14	2475	7237.9	8656.4	5182.1	1383.1	1420.6	1703.1
15	2475	1266.1	1311.4	1169.8	542.5	543.3	553.2
16	2475	7005.3	9914.0	6976.1	911.9	911.9	911.9
17	2475	5858.0	7216.6	4280.0	815.5	821.5	873.3
18	2475	5433.2	9366.6	9919.0	1034.6	1051.1	1226.0
19	2475	1884.1	1996.0	1814.9	923.4	937.4	1044.8
20	2475	4687.7	5514.9	3988.8	1186.0	1203.7	1341.7

Table B-19: Actual Return Periods of Settlement Estimated for Memphis, TN (1039)

		Actual T_R					
		Robertson and Wride (2009)			Idriss and Boulanger (2014)		
Profile	Assumed T_R	Mean	Modal	Semi	Mean	Modal	Semi
1	1039	1453.4	1478.8	1339.6	734.7	739.9	733.6
2	1039	1449.8	2114.1	2153.5	1042.1	1116.8	934.6
3	1039	1973.5	2349.7	1460.0	986.3	1017.2	953.9
4	1039	2083.4	2232.2	1661.2	918.7	932.1	904.8
5	1039	2274.0	5858.1	3227.2	1566.3	1972.6	1390.4
6	1039	2274.3	2484.6	1478.7	967.2	970.4	955.6
7	1039	2491.3	3230.6	1589.7	905.0	932.3	890.0
8	1039	8272.6	9884.0	2802.7	1678.2	1878.1	1474.1
9	1039	2331.2	5779.0	3073.1	1752.4	2401.5	1212.5
10	1039	3649.7	9189.5	2632.5	1454.8	1597.9	1307.8
11	1039	5893.9	9939.0	3111.5	1453.1	1646.3	1264.1
12	1039	3077.0	4491.4	2403.4	1025.8	1114.0	975.3
13	1039	1588.9	1681.1	1321.6	814.3	822.0	805.7
14	1039	7531.0	9972.0	2434.4	1631.5	1832.2	1488.2
15	1039	1710.9	1853.5	1324.1	702.6	707.2	700.8
16	1039	9325.6	9906.0	3214.5	1072.9	1072.9	1068.5
17	1039	6430.8	9944.0	2280.8	1015.6	1045.7	988.9
18	1039	6547.2	9984.0	5679.2	1231.1	1327.9	1144.3
19	1039	2343.2	2787.8	1683.5	1154.8	1224.2	1090.2
20	1039	5171.0	8525.9	2314.8	1398.4	1490.5	1309.9

Table B-20: Actual Return Periods of Settlement Estimated for Memphis, TN (2475)

		Actual T_R					
		Robertson and Wride (2009)			Idriss and Boulanger (2014)		
Profile	Assumed T_R	Mean	Modal	Semi	Mean	Modal	Semi
1	2475	1494.8	1527.0	1422.4	745.0	756.9	746.0
2	2475	2823.1	4409.8	3630.8	1174.4	1212.7	1152.8
3	2475	2686.0	2889.5	1812.4	1022.5	1039.7	1023.2
4	2475	2335.1	2454.8	2065.7	937.9	944.8	938.7
5	2475	9898.0	9939.0	8370.8	2296.6	2930.6	2302.4
6	2475	2670.7	2801.2	1692.7	970.4	970.4	970.4
7	2475	3367.3	3506.2	1955.6	987.0	1008.7	982.5
8	2475	9986.0	9902.0	5814.7	2031.6	2268.5	2035.5
9	2475	9894.0	9969.0	9989.0	2940.3	4634.3	2998.0
10	2475	9989.0	9953.0	4759.3	1677.6	1778.1	1683.8
11	2475	9878.0	9963.0	6566.3	1838.1	2106.3	1862.1
12	2475	5915.2	9467.4	4499.9	1189.1	1271.9	1193.6
13	2475	1747.1	1811.8	1450.6	823.9	823.9	823.9
14	2475	9980.0	9944.0	4971.7	1947.7	2003.5	1942.4
15	2475	1909.2	2029.2	1546.3	712.2	725.7	712.7
16	2475	9930.0	9892.0	6392.5	1072.9	1072.9	1072.9
17	2475	9882.0	9888.0	4265.1	1072.3	1099.8	1073.8
18	2475	9955.0	9975.0	9989.0	1411.2	1475.7	1413.0
19	2475	3167.5	3675.1	2192.6	1281.5	1328.4	1282.6
20	2475	9990.0	9974.0	4052.0	1541.3	1623.8	1541.7